UNIVERSITY of CALIFORNIA
Santa Barbara

Quantum control of surface acoustic wave phonons

A dissertation submitted in partial satisfaction of the
requirements for the degree of

Doctor of Philosophy

in

Physics

by

Kevin Joseph Satzinger

Committee in charge:

Professor Andrew N. Cleland, Chair

Professor Leon M. Balents

Professor David M. Weld

June 2018

The dissertation of Kevin Joseph Satzinger is approved:

Professor Leon M. Balents

Professor David M. Weld

Professor Andrew N. Cleland, Chair

June 2018

Acknowledgements

This has been a long journey, and I am overflowing with gratitude for the numerous people who have contributed to this work, directly and indirectly.

The person I must thank the most is Andrew Cleland, who has been my graduate advisor since I started at UCSB in 2012. His immense technical knowledge, street smarts, and leadership have (almost) always steered me in the right direction. I admit the move to Chicago in 2015 was challenging, both personally and professionally, but it was also a great opportunity to build a new group and lab from the foundation. In the end, we came out of it stronger. I am so thankful I had the opportunity to work on this project. I remember reading about Aaron O'Connell's work [70, 71] in college, which really attracted me to UCSB. Pushing quantum *mechanics* forward like this is a dream come true, and it was all possible thanks to Andrew.

I also want to thank everyone involved in this *special* journey to Chicago. Leon Balents and David Weld have graciously served on my committee from afar, and I appreciate that they have been there to support me. Many people went out of their way to accommodate us, especially Jennifer Farrar, Novia Pagone, and Mary Pat McCullough. The other people who moved to Chicago have a special place in my heart: Greg Peairs, my comrade-in-arms from the beginning; Peter Duda, whose heroic efforts to run the new cleanroom enabled all the fabrication in this thesis; and everyone from the Awschalom group who blazed the trail before us.

Andrew, Greg, and I faced some daunting challenges when we arrived in Chicago to empty rooms and numerous cardboard boxes. We were fortunate to be joined by such bright, hard-working new colleagues: Hung-Shen Chang, an inspirational figure always willing to learn and teach; Ming-Han Chou, who took up the mantle of aluminum nitride sputtering; Joel Grebel, who never gives up; Rhys Povey, natural leader and Mathematica wizard; and Youpeng Zhong, who made an even larger move from Zhejiang and set up our electronics for qubit experiments. Glory awaits all of you.

Over the years, we were joined by two outstanding postdocs. Étienne Dumur was instrumental in setting up our dilution refrigerator, and we worked out the coupling mechanism for the D line together. Audrey Bienfait's creative perspective was always welcome, and she taught me about amplifiers and noise. I wish them luck in their journeys in quantum acoustics.

I also had the opportunity to work closely with some younger students. Ivan Gutierrez and Ben November, Chicago undergraduates, really rose to the occasion and meaningfully contributed to a wide range of projects. Chris Conner, who started as a graduate student in 2017, quickly mastered many important experimental techniques; we worked together on the contents of chapter 4. I am sure you all have bright futures.

An important benefit of moving to Chicago was the presence of the Awschalom and Schuster groups. David Awschalom had my back, and Dave Schuster's enthusiasm and creativity really helped push this project forward. It was great to work with Sam Whiteley and Agnetta Cleland on acoustics and flip-chip integration. Nate Earnest and Ravi Naik

helped me feel welcome at Chicago way back in 2013 when I first visited (I'm glad we're all finally graduating).

I wouldn't have succeeded at Chicago without the foundation of my education at UCSB. Amit Vainsencher and Joerg Bochmann welcomed Greg and me into the fold and worked with us on piezoelectric optomechanics. They taught me many important lessons, scientific and otherwise. I benefited from the outstanding fabrication facilities and engineers at UCSB, chiefly the guidance of Brian Thibeault and the persistence of Brian Lingg. The Martinis group always provided support for our efforts, and I especially thank Erik Lucero for the photography tips, Dan Sank for the detailed microwave/filter discussions, and Andrew Dunsworth for qubit fabrication and design advice. I also want to thank my classmates and friends from UCSB. I wish I could have stayed with you, and it means a lot that our relationships persisted despite the distance.

Finally, I want to thank everyone who helped prepare me for graduate school in the first place. This was a worthy challenge, and I couldn't have done it without you. Thank you to my professors and friends from college and to the mentors of my undergraduate research experiences. Thank you to all my teachers, friends, and family. You took the time to shape me into the person I am.

Curriculum Vitæ

Kevin Joseph Satzinger

Education

2018	Ph.D., Physics, University of California, Santa Barbara National Science Foundation Graduate Research Fellowship, 2012-2015
2012	B.S., Physics & Mathematics, Truman State University, Kirksville, MO Valedictorian, Outstanding Student in Physics, Honors Scholar Barry M. Goldwater Scholarship, 2011

Professional Experience

2015-2018	Visiting graduate student researcher, Institute for Molecular Engineering, University of Chicago
2012-2015	Graduate student researcher, Department of Physics, University of California Santa Barbara
2011	Intern, Advanced Silicon Technology Group, Massachusetts Institute of Technology Lincoln Laboratory
2010	Intern, National Nanotechnology Infrastructure Network REU, School of Engineering and Applied Sciences, Harvard University
2009	Intern, National Science Foundation REU, Department of Physics, Southern Illinois University Carbondale

Publications

"Quantum control of surface acoustic wave phonons," K. J. Satzinger et al., *Submitted* (2018)

"Simple and reusable non-galvanic flip-chip integration for hybrid quantum systems," K. J. Satzinger et al., *In Preparation* (2018)

"Coherent control of spins with Gaussian acoustics," S. J. Whiteley, G. Wolfowicz, C. P. Anderson, A. Bourassa, H. Ma, M. Ye, G. Koolstra, K. J. Satzinger, F. J. Heremans, A. N. Cleland, D. I. Schuster, G. Galli, D. D. Awschalom, *Submitted* (2018)

"Bi-directional conversion between microwave and optical frequencies in a piezoelectric optomechanical device," A. Vainsencher, K. J. Satzinger, G. A. Peairs, A. N. Cleland, *Applied Physics Letters* 109, 033107 (2016)

"The importance of cantilever dynamics in the interpretation of Kelvin probe force microscopy," K. J. Satzinger, K. A. Brown, R. M. Westervelt, *Journal of Applied Physics* 112, 064510 (2012)

"High spatial resolution Kelvin probe force microscopy with coaxial probes," K. A. Brown, K. J. Satzinger, R. M. Westervelt, *Nanotechnology* 23, 115703 (2012)

Abstract

Quantum control of surface acoustic wave phonons

by

Kevin Joseph Satzinger

Quantum behavior in a macroscopic mechanical resonator is of great scientific and technological interest, but it is a substantial experimental challenge to realize. In particular, surface acoustic waves have emerged in recent years as a likely platform for coupling disparate quantum systems together. In this thesis, we present a surface acoustic wave resonator strongly coupled to a superconducting qubit. We begin by describing simple experiments with surface acoustic waves. Next, we discuss the design of a qubit and tunable coupler circuit to maintain good qubit performance in the presence of a surface acoustic wave resonator on an incompatible substrate. We then explain how to bring together devices on separate chips in a simple, accessible flip-chip assembly. Finally, we put these elements together to establish quantum control of surface acoustic wave phonons. We demonstrate good qubit performance and strong, tunable coupling to the acoustic mode. We show ground state cooling of the surface acoustic wave resonator with probability at least 99.5%. Finally, we illustrate quantum superposition in the surface acoustic wave resonator, conducting Wigner tomography of a superposition $|0\rangle + |1\rangle$, which we find has fidelity 0.945 ± 0.006.

Contents

Chapter 1

Introduction

To begin, we review the basic ideas of this thesis and some previous work.

1.1 Overview

The superposition of quantum states is one of the hallmarks of quantum physics, and clear demonstrations of superposition have been achieved in a number of quantum systems. However, macroscopic mechanical systems have remained a challenge, with only indirect demonstrations of mechanical state superpositions, in spite of the intellectual appeal and technical utility such a capability would bring [86, 90, 56]. This is due in part to the highly linear response of most mechanical systems, making quantum operation difficult, as well as their characteristically low frequencies, making it difficult to reach the quantum ground state. Linear resonant systems are traditionally challenging to control at the level of single quanta, as they are always in the correspondence limit [13].

The recent advent of engineered quantum devices in the form of qubits has enabled full quantum control over some linear systems, in particular electromagnetic resonators [43, 96]. A number of experiments have demonstrated that qubits may provide similar control over mechanical degrees of freedom, including qubits coupled to bulk acoustic modes [70, 20], surface acoustic waves [38, 62], and flexural modes in suspended beams [1, 55, 103, 59]. Of particular note are experiments in which a superconducting qubit is coupled via a piezoelectric material to a microwave-frequency bulk acoustic mode [22], where the ground state can be achieved at moderate cryogenic temperatures, and demonstrations include controlled vacuum Rabi swaps between the qubit and the mechanical mode [70, 20]. However, the level of quantum control and measurement has been limited by the difficulty of engineering a single mechanical mode with sufficient coupling and quantum state lifetime. More advanced operations, such as synthesizing arbitrary acoustic quantum states and measuring those states using Wigner tomography, remain a challenge.

Here we report a significant advance in the level of quantum control of a mechanical device, where we couple a superconducting qubit to a microwave-frequency surface acoustic wave resonance, demonstrating ground-state operation, vacuum Rabi swaps between the qubit and the acoustic mode, and the synthesis of mechanical Fock states as well as a Fock state superposition. We map out the Wigner function for these mechanical states using qubit-based Wigner tomography. We note that a similar achievement has recently been reported with an experiment coupling a superconducting qubit to a bulk acoustic

mode [21].

In the rest of this chapter, we review some fundamental concepts and related work mentioned above. In the next two chapters, we discuss the two key elements to our experiment: surface acoustic waves and superconducting qubits. In chapter 4, we explain how to bring them together with a simple flip-chip technique. In chapter 5, we present our experimental results coupling a surface acoustic wave resonator to a superconducting qubit. We conclude with chapter 6, a summary of the key lessons from this work and a discussion of possible future directions.

1.2 Harmonic oscillator

The harmonic oscillator is a classic element of physics, permeating all levels. A simple example is a mass m on a spring with stiffness k, which exhibits harmonic motion at its resonant angular frequency $\omega = \sqrt{k/m}$. The mass has position x relative to its equilibrium position and momentum $p = m\dfrac{dx}{dt}$. This brings about the classical Hamiltonian [36]

$$H = \frac{1}{2m}p^2 + \frac{k}{2}x^2. \tag{1.1}$$

1.2.1 Quantum mechanics

We can also consider the harmonic oscillator subject to quantum mechanics [83]. It may seem odd to consider quantum behavior in something macroscopic like a mass on a spring,

but in this thesis, we will demonstrate characteristically quantum behavior in a closely related mechanical system. The Hamiltonian H and the variables x and p are promoted to quantum operators with the commutation relation $[x, p] = i\hbar$. This can be recast into the familiar "ladder" form, using

$$a = \sqrt{\frac{m\omega}{2\hbar}} \left(x + \frac{i}{m\omega} p \right), \tag{1.2}$$

which satisfies $[a, a^\dagger] = 1$, to arrive at

$$H = \hbar\omega \left(a^\dagger a + \frac{1}{2} \right). \tag{1.3}$$

In this form, we naturally see the structure of the quantum system. The energy eigenstates $|n\rangle$ are eigenstates of $a^\dagger a$ with eigenvalue n; these are also called Fock states. A final concept to mention is the coherent state $|\alpha\rangle$, which is an eigenstate of a with eigenvalue α [83]:

$$|\alpha\rangle = e^{-|\alpha|^2/2} \sum_{n=0}^{\infty} \frac{\alpha^n}{\sqrt{n!}} |n\rangle. \tag{1.4}$$

We can generate a coherent state using a classical drive, which we explore experimentally in chapter 5.

Besides the wavevector $|\psi\rangle$, wavefunction $\psi(x) = \langle x|\psi\rangle$, or density matrix ρ, an alternative representation of a resonator state is the Wigner function $W(x, p)$, a real-valued quasiprobability distribution [100, 40]. It can take on negative values, which are a signature of non-classical behavior. We define it in terms of a density matrix ρ; for a pure state $|\psi\rangle$, $\rho = |\psi\rangle\langle\psi|$. By definition,

$$W(x, p) = \frac{1}{\pi\hbar} \int_{-\infty}^{\infty} \langle x + y|\rho|x - y\rangle e^{2ipy/\hbar}\, dy. \tag{1.5}$$

We can recover the actual probability distributions P along x and p by integrating away the opposite variable:

$$P(x) = \int_{-\infty}^{\infty} W(x,p)\,dp \tag{1.6}$$

$$P(p) = \int_{-\infty}^{\infty} W(x,p)\,dx \tag{1.7}$$

$$\tag{1.8}$$

We revisit Wigner functions when we characterize quantum states in a macroscopic mechanical resonator in chapter 5.

1.2.2 Normal modes in solids

When we bring a collection of atoms together to make a solid, the motion of every atom becomes coupled together. These interactions give rise to many characteristic frequencies and normal modes of vibration [36].[1] For small amplitudes, each of these normal modes acts as an independent harmonic oscillator with its own frequency and displacement profile. The subject of this thesis is to take one particular normal mode, a 4 GHz vibration on the surface of a crystal, and cause it to exhibit quantum behavior.

The notion of quantum behavior in mechanical normal modes dates back over a century, when Einstein [31] and later Debye [25] used models composed of independent harmonic oscillators to explain the low-temperature behavior of the specific heat of solids

[1] In quantum experiments with trapped ions, normal modes of motion in arrays of several trapped ions are used to generate entanglement between ions [93].

[72]. The relevant phenomenon was what happens when the thermal energy $k_B T$ becomes small compared to the single-phonon energy $\hbar\omega$. In the Einstein model, all the modes have the same frequency, while the Debye model uses a reasonable distribution of frequencies. The familiar Debye temperature T_D corresponds to the energy of the highest-frequency mode in the solid.

From low temperature heat capacity measurements, it was apparent that these normal modes behave quantum mechanically and can approach their ground states of motion. One wonders to what extent such a mechanical mode can exhibit quantum behavior such as quantum superposition. In this thesis, we explore this question in great detail.

1.3 Ground state cooling

About a decade ago, there was a flurry of interest in attempting to cool a macroscopic mechanical resonator to the quantum ground state. The first demonstration, mentioned above, involved a 6 GHz resonator coupled to a superconducting qubit at cryogenic temperatures [70]. We discuss this further below, but first we mention a different set of experiments that use active cooling to supplement cryogenic refrigeration.

1.3.1 Experiments with active cooling

Since 2010, there have been many examples of ground state cooling, which is usually taken to mean measuring an average phonon number $\langle n \rangle < 1$.[2] Many of these use an

[2]One could have a stricter criterion, such as $\langle n \rangle < 0.5$ or $\ll 1$. The achievement in Ref. [70] had $\langle n \rangle \leq 0.07$, rather persuasive. In chapter 5, we demonstrate $\langle n \rangle \leq 0.005$.

active cooling scheme based on cavity optomechanics, where the mechanical mode of interest (angular frequency ω_m) is parametrically coupled to an electromagnetic mode (angular frequency $\omega_e \gg \omega_m$), such as a microwave or optical resonance [4]. The origin of this coupling is that the motion x of the mechanical mode shifts the electromagnetic angular resonance frequency ω_e: $\partial\omega_e/\partial x \neq 0$.

Instead of exclusively relying on direct refrigeration ($k_B T \ll \hbar\omega_m$), these experiments use the optomechanical interaction to bring about cooling, primarily sideband cooling. The basic idea is to illuminate the electromagnetic mode with red-detuned radiation at angular frequency $\omega_e - \omega_m$. Under the right circumstances, a mechanical phonon and a red-detuned photon can combine their energy, generating a photon with energy $\hbar\omega_e$ in the electromagnetic mode. This process removes one phonon, slightly cooling the mechanical mode.

We briefly summarize several pioneering examples. In Ref. [91], Teufel et al. strongly couple a 10 MHz vibration of a suspended metal drum to a 7.5 GHz superconducting LC resonator at a temperature of 15 mK. Sideband cooling brings the phonon occupation to $\langle n \rangle = 0.34 \pm 0.05$. Chan et al. [16] use a silicon optomechanical crystal coupling co-localized mechanical (3.7 GHz) and optical (195 THz, 1540 nm) modes. Starting at 20 K, they use sideband cooling to achieve $\langle n \rangle = 0.85 \pm 0.08$. As a last example, in Ref. [73], Peterson et al. suspend a silicon nitride membrane with a 1.5 MHz mechanical mode in an optical Fabry-Pérot resonator at 70 mK. They use sideband cooling and measure $\langle n \rangle = 0.20 \pm 0.02$, reaching the quantum backaction limit for their experiment. There

are many more example of ground state cooling that have been achieved, many building directly on these works.

1.3.2 Coupling to qubits

We now address an alternative approach, the one we will take in this thesis, first demonstrated in Ref. [70]. There are two key ingredients. The first is to use a GHz frequency mode at mK temperatures, realizing $k_B T \ll \hbar\omega_m$. If the mechanical mode thermalizes to the cryostat temperature, it will automatically be very close to the quantum ground state, without the need for active cooling. The second ingredient is to couple to a highly nonlinear system, in this case a superconducting qubit. The qubit can be used to assess the state of the mechanical resonator, in particular how close it is to the quantum ground state. This also allows the experiment to rapidly transcend ground state cooling: nonclassical states can be generated by a qubit and then imprinted on the mechanical resonator.

In Ref. [70], O'Connell et al. use a 6.2 GHz vibration of a suspended parallel plate capacitor made with piezoelectric aluminum nitride. It is capacitively coupled to a superconducting phase qubit. O'Connell et al. demonstrate ground state cooling, $\langle n \rangle \leq 0.07$, and furthermore the swapping of a photon from the qubit into the resonator, generating a single phonon state. This experiment is limited by the short lifetime of the resonance (6 ns), and the qubit lifetime is short as well (17 ns), but they still achieve strong coupling; the time to swap a single photon/phonon is 4 ns.

Recently, a complementary effort with much longer mechanical lifetimes has emerged. Chu et al. [20] use acoustic overtones in a 420 µm thick sapphire plate. The primary modes are separated by a free spectral range of 13.2 MHz, and they also couple to spurious Bessel modes close to each primary mode. They use a disk of aluminum nitride on the sapphire surface to couple these modes to the electric field of a 3D transmon. They measure $\langle n \rangle \leq 0.02$ and demonstrate similar phonon control to Ref. [70], although the lifetimes involved are much longer ($\sim$10 µs), with much slower interactions. Very recently, this group has substantially improved their devices by using a curved surface to extricate their primary mode from the spurious modes [21]. Their work is complementary to what we present in this thesis, with many similar achievements, but in bulk acoustic waves.

1.4 Surface acoustic waves

Surface acoustic waves are vibrations localized near the surfaces of elastic solids. We discuss them at length in chapter 2, and we demonstrate coupling between a superconducting qubit and a surface acoustic wave resonator in chapter 5. Here, we just discuss some related work in the realm of coupling qubits and surface acoustic waves.

Surface acoustic waves are a mature technology for many classical applications, and there are hopes that they could be very useful in emerging quantum technologies. The idea is that surface acoustic waves are easily controlled, and they should also be able to couple to a wide variety of disparate quantum systems [87, 3, 99].

Over the past few years, there have been several experiments coupling superconduct-

ing qubits to surface acoustic waves in various ways. This comes about rather naturally: the main technology to interact with surface acoustic waves is a transducer made of an interdigital capacitor, and that capacitor can be integrated with a qubit circuit. In these experiments, the capacitance of the transducer constitutes part of the capacitance of a transmon superconducting qubit. This brings about a strong interaction between the qubit and surface acoustic waves.

Gustafsson et al. [38] made the first demonstration of such a transmon/transducer hybrid. By tuning the qubit to the transducer frequency (4.8 GHz), they efficiently emit single phonons. They also interrogate the qubit with a separate transducer coupled to a transmission line. In Ref. [62], Manenti et al. use a similar device, but with a lower frequency transducer (520 MHz). In this case, they place the transducer between two acoustic mirrors, making an acoustic resonator. The acoustic waves are at a much lower frequency than the qubit, but they still observe some non-resonant interactions, including time-domain measurements showing the qubit interacting with an acoustic pulse bouncing back and forth between the mirrors. Finally, in Ref. [65], Moores et al. bring these two ideas together, placing the qubit/transducer in an acoustic resonator at 4.3 GHz. They observe spectroscopic evidence of strong coupling between the qubit and several acoustic modes.

Chapter 2

Surface acoustic waves

The main subject of this thesis is a surface acoustic wave (SAW) resonator that we couple to a superconducting qubit. In this chapter, we describe some fundamental concepts of surface acoustic wave devices. We go over classical experiments with a variety of resonators. Finally, we consider how to couple such a resonator to a qubit.

2.1 Introduction

Surface acoustic waves are vibrations confined near the surface of an elastic solid [79, 42, 66]. Since the 1960s, many technological applications of electromechanical surface acoustic wave devices at radio frequencies have emerged. SAW devices are now ubiquitous, with billions of devices manufactured each year.[1]

Two main characteristics make SAW devices technologically viable: their relatively

[1]Applications include radar, ultrasonics, sensors, mobile phones, GPS receivers, RFID tags, and garage door openers.

slow propagation speed (a few km/s, 10^{-5} times the speed of light), and the ease of manipulating them with simple lithographically-defined metal patterns. The operation frequency is set lithographically by the wavelength of the metal patterns. Taken together, these features allow the construction of physically compact devices many wavelengths in extent, enabling structures like delay lines (4 mm at 4 km/s is 1 µs), pulse compressors, and various other filters.

2.1.1 Rayleigh waves

There are various types of surface acoustic waves, but here we concern ourselves with the simplest and most common, Rayleigh waves [79].[2] Here, we sketch a discussion from Ref. [66]. Consider an acoustic plane wave in an infinite isotropic elastic medium with angular frequency ω and wavevector $\vec{k}$. The displacement $\vec{u}$ takes the form

$$\vec{u}(\vec{r}, t) = \vec{u}_0 \exp[i(\omega t - \vec{k} \cdot \vec{r})]. \tag{2.1}$$

The direction of $\vec{u}_0$ compared to $\vec{k}$ determines the polarization of the wave; it is natural to consider separately transverse (shear) waves ($\vec{u}_0$ and $\vec{k}$ orthogonal, with speed v_t) and longitudinal waves ($\vec{u_0}$ and $\vec{k}$ parallel, with speed v_ℓ). Longitudinal waves are faster than transverse waves in the same medium ($v_\ell > v_t$).

We construct a Rayleigh wave out of two plane waves. Consider a semi-infinite isotropic elastic medium with its surface in the xy plane, as depicted in Fig. 2.1a. The boundary condition is that the surface $z = 0$ is stress-free. We add a transverse plane

[2] Rayleigh waves are also important in seismology; they come from earthquakes.

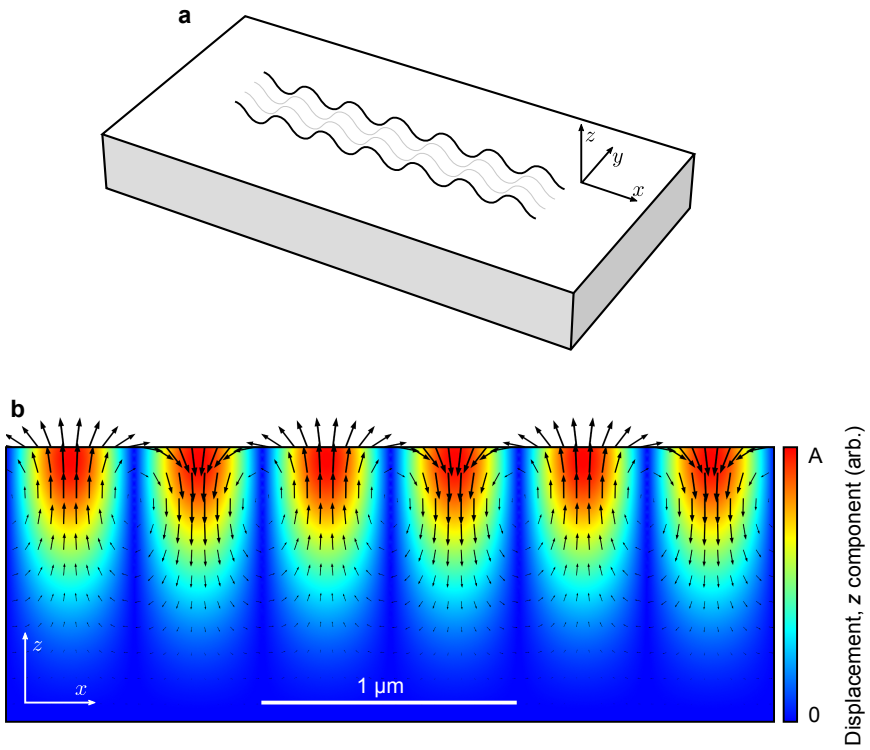

Figure 2.1: **Rayleigh waves. a,** Schematic showing a Rayleigh wave propagating along the $z = 0$ surface in the x direction. **b,** Illustration of the displacement of a Rayleigh wave. The color shows the amplitude of the displacement z component, and the arrows show the displacement vector field. This is actually calculated using the finite element simulation we will revisit in Fig. 2.4.

wave with wavevector $|\vec{k}_t| = \omega/v_t$ to a longitudinal wave with wavevector $|\vec{k}_\ell| = \omega/v_\ell$. We seek to generate a wave propagating along the x direction, with no y dependence; the displacements should vary as $\exp(-ik_R x)$. This imposes a constraint on the components of $\vec{k}_t$ and $\vec{k}_\ell$: x component equal to k_R, zero y component, and z component constrained by the magnitudes listed above. Demanding that the amplitude decays as we descend beneath the surface forces the z components to be nonzero and *imaginary*. This means $k_R > |\vec{k}_t| > |\vec{k}_\ell|$, so the speed $v_R = \omega/k_R$ is less than the bulk wave speeds ($v_R < v_t < v_\ell$).[3] Finally, the stress-free boundary condition determines the relative amplitude and phase of the transverse and longitudinal components. We arrive at the following displacement, a Rayleigh wave:

$$\vec{u}(\vec{r}, t) = A(u_x \hat{x} + u_z \hat{z}) \exp[i(\omega t - k_R x)] \tag{2.2}$$

$$u_x = \gamma \exp(a k_R z) - \exp(b k_R z) \tag{2.3}$$

$$u_z = i \left[\gamma a \exp(a k_R z) - b^{-1} \exp(b k_R z)\right], \tag{2.4}$$

where a, b, and γ are positive, dimensionless, real numbers dictated by ω and material properties, and A is proportional to the displacement amplitude. This wave propagates along the surface in the x direction with maximum displacement at the surface. The amplitude exponentially decays as we descend into the bulk; the characteristic decay length approximately equals to the wavelength $\lambda_R = 2\pi v_R/\omega = 2\pi/k_R$. We plot an

[3]Here, for example, $\vec{k}_t = k_R \hat{x} + \sqrt{|\vec{k}_t|^2 - k_R^2}\hat{z}$, and $k_R > |\vec{k}_t|$. The positive imaginary z component makes $\exp[-ik_{t,z} z]$ give exponential decay into the bulk ($z < 0$).

example in Fig. 2.1b. Note that the x and z displacements are 90° out of phase, so each element follows an elliptical path.

2.1.2 Piezoelectricity

Certain anisotropic materials with particular symmetry properties and charge distributions exhibit a very important property, piezoelectricity, where strain $\boldsymbol{S}$ is accompanied by polarization $\vec{P}$ [24, 23].[4] The familiar electric displacement field $\vec{D} = \epsilon_0 \vec{E} + \vec{P}$, where $\vec{E}$ is the electric field. Ordinarily, this can be computed as $\boldsymbol{\epsilon} \cdot \vec{E}$ with a suitable dielectric tensor $\boldsymbol{\epsilon}$. Similarly, the stress $\boldsymbol{T}$ is ordinarily related to the strain $\boldsymbol{S}$ by $\boldsymbol{T} = \boldsymbol{c} \cdot \boldsymbol{S}$, where $\boldsymbol{c}$ is the stiffness tensor.

However, in a piezoelectric material, these are coupled together. There are various ways of expressing the relationship; here we use "stress-charge form" with a piezoelectric coupling tensor $\boldsymbol{e}$. In this form, we calculate the stiffness tensor at constant electric field and the dielectric tensor at constant stress, as those are the independent variables. The relationship is given by [23]

$$\vec{D} = \boldsymbol{\epsilon} \cdot \vec{E} + \boldsymbol{e} \cdot \boldsymbol{S} \tag{2.5}$$

$$\boldsymbol{T} = -\boldsymbol{e}^t \cdot \vec{E} + \boldsymbol{c} \cdot \boldsymbol{S}, \tag{2.6}$$

where $\boldsymbol{e}^t$ denotes the transpose of $\boldsymbol{e}$. These equations say that a strain brings about an electric displacement field, and an electric field brings about a stress.

[4] We denote tensor quantities like $\boldsymbol{S}$ with bold-face letters.

This applies to our discussion of Rayleigh waves: on a piezoelectric substrate, the traveling acoustic wave is principally a wave of strain, but it takes a wave of polarization along for the ride. This allows us to control surface acoustic waves using voltages applied to patterned metal transducers, which we discuss below.

2.1.3 Piezoelectric Rayleigh waves

Note that we only discussed Rayleigh waves on an isotropic solid, but similar waves exist in anisotropic media, including piezoelectric substrates; these are called piezoelectric Rayleigh waves. It is important to consider the *electrical* boundary condition on the surface of the piezoelectric substrate. For a non-metallized surface, there are no free charges on the surface, and there will be a voltage wave in the vacuum above the surface. For a metallized surface, the conductor shorts out surface potentials. On a piezoelectric substrate, this slows down the wave speed by a fraction $\Delta v/v$.

This is closely related to the piezoelectric coupling strength of the material, though it is specific to surface acoustic waves. We use the standard piezoelectric coupling coefficient $K^2 = 2\Delta v/v$ to summarize the piezoelectric coupling strength of a material. This is a simplification compared to examining the details of the piezoelectric coupling tensor $\boldsymbol{e}$ or its strain-charge form sibling $\boldsymbol{d}$.

2.1.4 Piezoelectric materials

There are many different piezoelectric materials of technological interest. Several experiments mentioned in chapter 1 use aluminum nitride [70, 12, 94, 20]. This is a reasonably robust material that can be deposited in thin films with controlled stress [32] and even grown epitaxially in some circumstances [95]. Although these were not experiments with surface acoustic waves, we can get an idea of the piezoelectric coupling strength by examining the coefficient K^2 for aluminum nitride; it is about 0.5% [14].

Quartz, crystalline silicon dioxide, is a common material for SAW devices [66]. The usual crystal orientation, called ST-X, has favorable temperature stability properties near room temperature. It has been observed to be very low-loss at cryogenic temperatures [37, 61, 80]. It is a relatively weak piezoelectric material, $K^2 = 0.12\%$, though this increases the plausibility of making good superconducting qubits on quartz [62]. Gallium arsenide is another weak piezoelectric material, with $K^2 = 0.07\%$ [38]. It is not widely used in industrial SAW devices, but it has been used in some experiments with surface acoustic waves coupled to qubits [39, 38, 65].

Lithium niobate is the other common material for SAW devices [66]. There are various crystal orientations for different applications. Here we concern ourselves with a very popular orientation, the 128°Y-X crystal cut, a rotated Y cut where the waves propagate along the crystal X direction. This has several favorable properties: very strong $K^2 = 5.4\%$ (roughly 50 times that of quartz or gallium arsenide), a relatively high wave speed $v = 4.0\,\mathrm{km/s}$, transducers with small internal reflections, and minimal

coupling to bulk waves [42]. Another popular orientation worth mentioning is Y-Z, which has minimal diffraction [66]. Lithium niobate has some very interesting properties besides strong piezoelectricity: ferroelectricity, pyroelectricity, and many useful optical properties [101, 102]. In this thesis, all of our surface acoustic devices use lithium niobate, 128°Y-X. See appendix E for fabrication information.

2.2 Surface acoustic wave resonators

The subject of this thesis is surface acoustic wave *resonators*, where waves are trapped between two mirrors, and we will just have one transducer inside each resonator. We show an example of such a resonator in Fig. 2.2. There are many other sorts of SAW devices, typically involving more than one transducer communicating through resonant or traveling modes [66], but we will not discuss them further. Here we describe the essential operation and properties of the components that constitute surface acoustic wave resonators; for more details, see Refs. [42, 41, 66]. Also see appendix A for information about numerically modeling these devices.

2.2.1 Mirrors

A good surface acoustic wave mirror will reflect almost all of the incoming acoustic waves. This is a bit challenging to do without inadvertently scattering some of the incoming waves into other modes, such as bulk acoustic waves. A very successful approach is to use a Bragg-style mirror made of a periodic structure where each period reflects a small

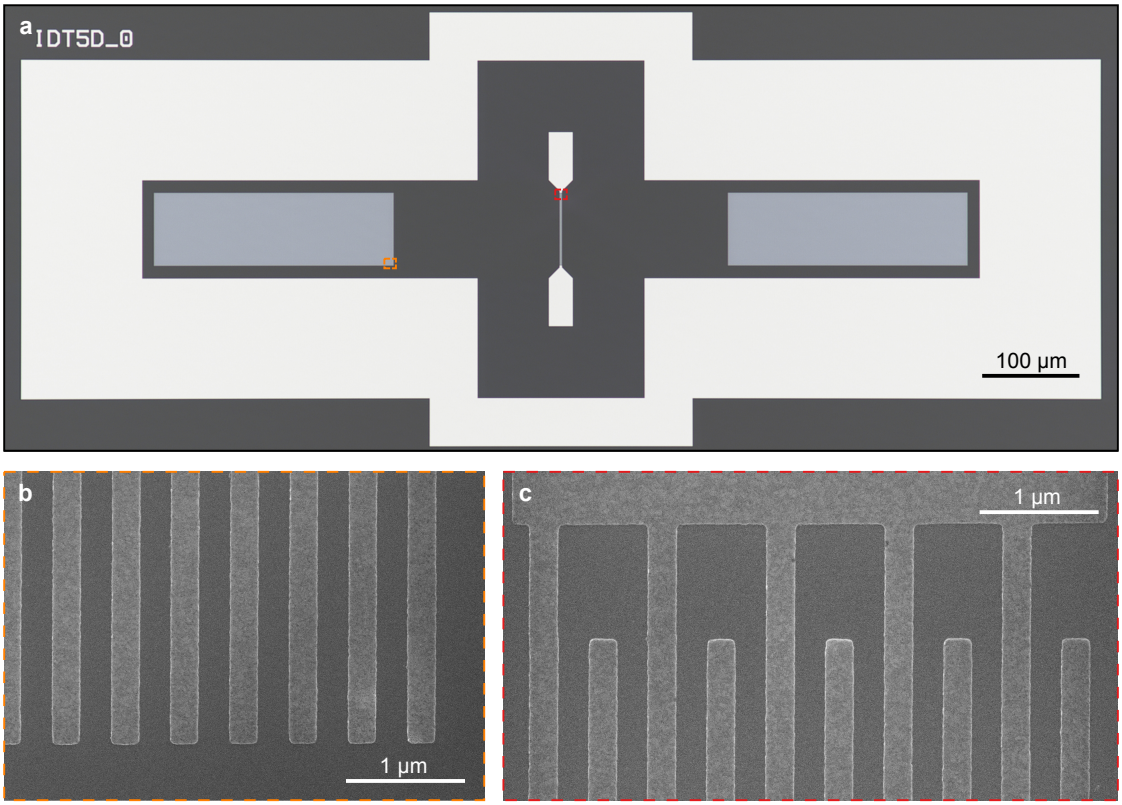

Figure 2.2: **Surface acoustic wave resonator. a,** Optical micrograph of a typical Fabry-Pérot style resonator. The transducer (center) has two electrodes for measurements (above and below). There are two large mirrors (left and right). **b-c** Scanning electron micrographs of the corner of a mirror (**b**) and the top of a transducer (**c**).

amount ($|r| \sim 1\%$) of the incoming wave amplitude.[5] If the period lines up correctly with the acoustic wavelength, there is constructive interference, yielding nearly 100% reflection over a fractional bandwidth $\Delta f/f \approx 2|r|/\pi$. This frequency band is called the "stop band." Intuitively, larger reflection per line $|r|$ gives a larger stop band because most of the wave is reflected in $\approx 1/|r|$ periods, and if that number of periods is smaller, a wider range of wavelengths can "line up" with the mirror long enough to be reflected.

Ordinarily, a mirror is made of several hundred thin metal lines or shallow grooves etched into the substrate. Having thicker metal or deeper grooves tends to increase the reflection per line $|r|$, but taking this too far leads to loss from scattering into bulk acoustic waves. A typical thickness or depth is about 1% of the acoustic wavelength λ, although that is often unreasonably thin for GHz frequency devices where $\lambda \sim 1\,\mu\text{m}$.

On weak piezoelectric materials, such as quartz, the reflections are dominated by mechanical scattering from the mass loading of the metal lines or etched grooves. For metal lines on strong piezoelectric substrates, such as lithium niobate, in addition to mechanical reflections, there are reflections caused by the metal lines shorting out the surface potential under them, slowing down the effective wave speed. If the metal is sufficiently thin, this is the dominant effect. In the devices we discuss below, there is a comparable contribution from mechanical and piezoelectric reflections.

Another important consideration for these piezoelectric reflections is the electrical connectivity of the metal lines, whether they are connected together (short-circuit) or individually floating (open-circuit). This determines the *phase* of the piezoelectric re-

[5]The reflection per period r is conventionally an imaginary number.

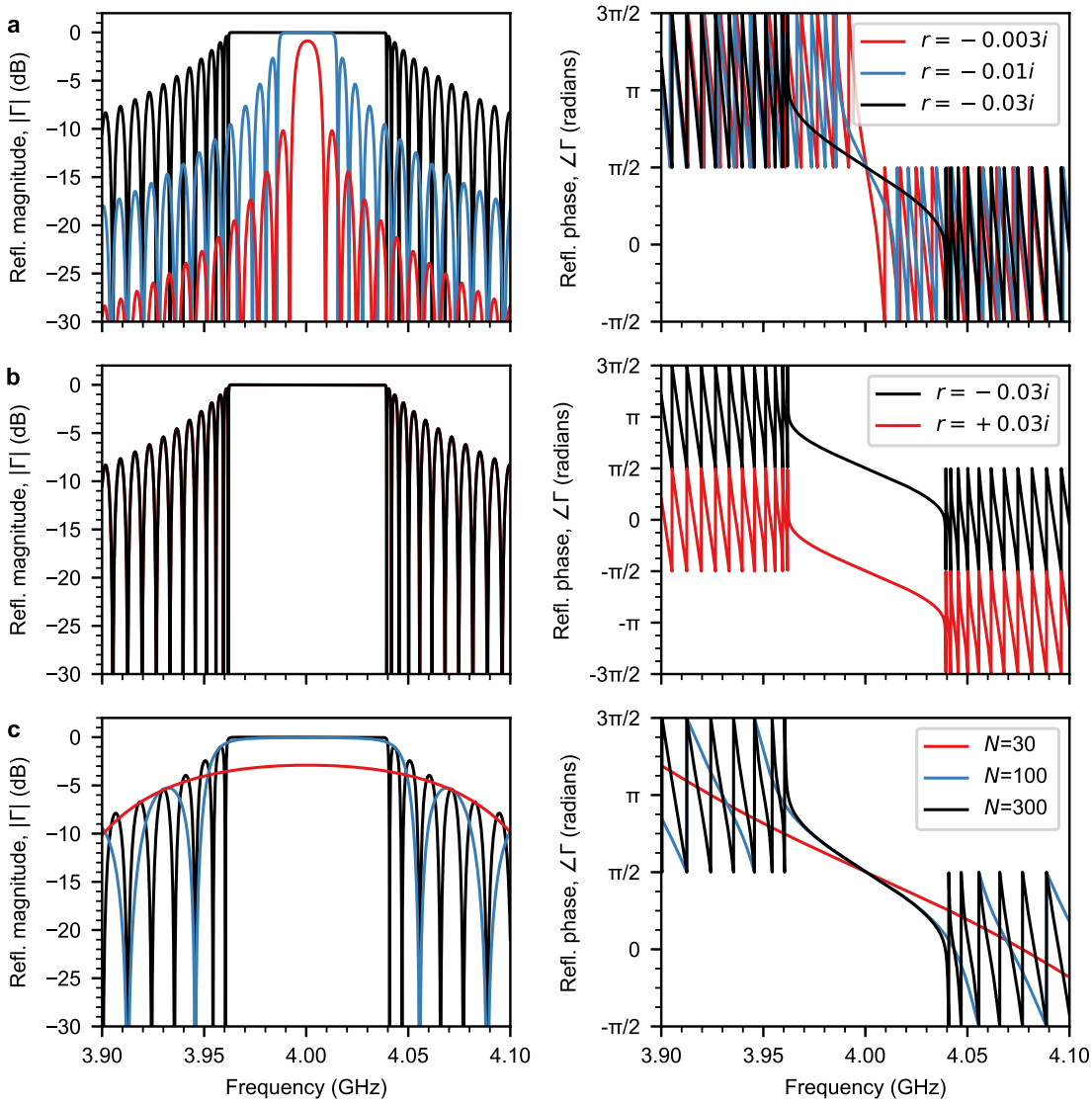

Figure 2.3: **Calculated reflection Γ from a lossless acoustic mirror.** Left: Reflection magnitude $|\Gamma| = |P_{11}|$. Right: Reflection phase $\angle\Gamma = \angle P_{11}$. **a,** Vary $|r|$ with $N = 500$. The mirrors in our devices, below, have $r \approx -0.03i$. **b,** Vary the sign of r with $N = 500$. **c,** Vary N with $r = -0.03i$.

flections. How this compares to the phase of the mechanical reflections depends on the substrate and crystal orientation. In our case, with 128Y-X lithium niobate, we use open-circuit lines in our mirrors to maximize reflection $|r|$, while the lines in the transducer are approximately short-circuit, giving smaller $|r|$.

Four important parameters in a mirror are its reflection per line r, number of lines N, period p, and effective wave speed v.[6] Maximal reflections occur when the period is half a wavelength ($p = \lambda/2 = \pi v/\omega$), giving a center angular frequency $\omega_m = \pi v/p$. In Fig. 2.3, we show calculated mirror reflections $\Gamma = P_{11}$, magnitude and phase, for a variety of r and N values, assuming a center frequency of 4 GHz. These are calculated with the coupling-of-modes method; see appendix A. Note in particular the dependence of the stop bandwidth on $|r|$, the reflection phase on the sign of r, and the dependence of the maximum reflection magnitude and out-of-band ripples on N.

2.2.2 Transducers

Surface acoustic wave transducers allow us to launch and detect surface acoustic waves electronically, interfacing with currents and voltages. SAW devices use transducers made of periodic interdigital capacitors. The periodic geometry allows a transducer to interact with waves which appropriately align with the fingers of the transducer, similar to the Bragg mirror discussed above.

In this interdigital transducer, the fingers alternate between positive and negative polarity; the positive fingers are electrically connected to one electrode, and the negative

[6] The loss in the mirror is also important in real devices, but not for this discussion.

fingers are electrical connected to the other. When a voltage is applied across the transducer, a periodic electric field develops between the two sets of fingers. This is spatially well-matched to a surface acoustic wave with the same wavelength as the transducer. As discussed above, this electric field brings about a mechanical stress in the substrate. If we apply an AC voltage with frequency corresponding to the transducer wavelength, the transducer efficiently launches surface acoustic waves. We illustrate this in Fig. 2.4a-c. The reverse process also works, so the transducer can also detect surface acoustic waves.

We can understand a lot about a transducer by studying its admittance

$$Y_t(\omega) = i\omega C + Y_a(\omega), \tag{2.7}$$

where C is the interdigital capacitance and $Y_a(\omega)$ is a complex, frequency-dependent "acoustic" admittance characterizing the transduction. To gain some intuition, we study a very simple model of a lossless, non-reflective transducer [66]. It has wavelength λ_t, effective wave speed v_t, center angular frequency $\omega_t = 2\pi v_t/\lambda_t$, aperture W (the finger overlap length), and N_t pairs of fingers. We just look at the real part $\mathrm{Re}[Y_a(\omega)]$; the imaginary part is its Hilbert transform. $\mathrm{Re}[Y_a(\omega)]$ has a characteristic "sinc squared" shape:

$$\mathrm{Re}[Y_a(\omega)] = Y_0 \left[\frac{\sin[\pi N_t(\omega - \omega_t)/\omega_t]}{\pi N_t(\omega - \omega_t)/\omega_t} \right]^2. \tag{2.8}$$

The prefactor Y_0 is somewhat involved; it is proportional to $\epsilon_{\text{eff}}\omega_t W N_t^2 K^2$, where ϵ_{eff} is the effective dielectric constant of the substrate (also called ϵ_∞ in the SAW literature). We illustrate the particularly-important dependence on the number of finger pairs N_t in Fig. 2.4d. Having more finger pairs increases the resonant response at the expense of

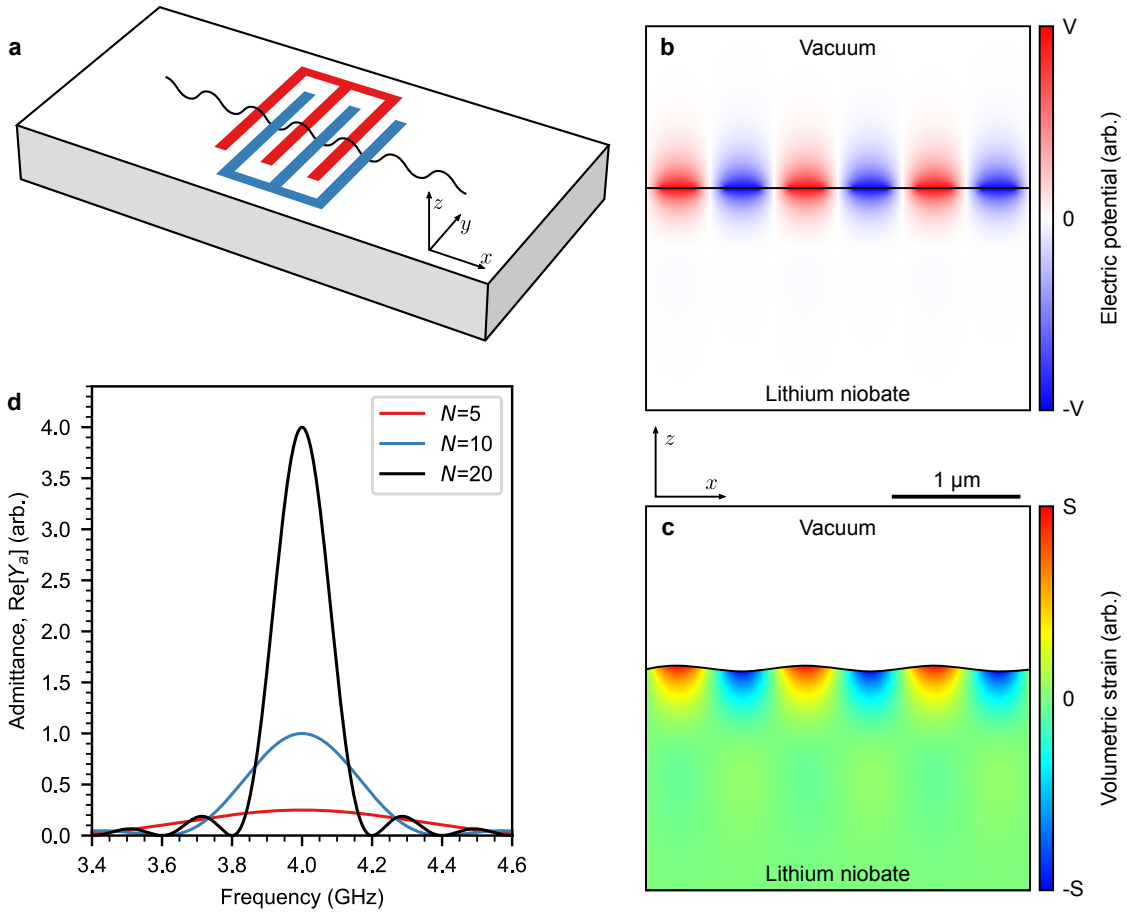

Figure 2.4: **Interdigital transducers.** **a,** Schematic of an interdigital transducer (perspective view). One side of the interdigital capacitor is blue, and the other is red. The black sine wave represents a surface acoustic wave. **b-c,** Side view of a finite element simulation of a simple interdigital transducer (COMSOL). As in **a**, there are three finger pairs. The simulation has periodic boundary conditions. **b,** Electric potential in the presence of a DC voltage applied across the transducer. The associated electric field $\vec{E}$ brings about a stress $\boldsymbol{T}$ which can drive acoustic waves. **c,** Volumetric strain showing the acoustic wave excited by resonant drive (AC voltage near 4 GHz). The geometry is also distorted according to the simulated displacement profile (the amplitude is greatly exaggerated). **d,** Calculated admittance $\mathrm{Re}[Y_a(\omega)]$ for a simple transducer with different numbers of finger pairs N_t. The transducer has wavelenth $\lambda_t = 1\,\mu\mathrm{m}$ and speed $v_t = 4\,\mathrm{km/s}$. The admittances are normalized to the $N_t = 10$ maximum.

bandwidth. The fractional bandwidth is roughly $\Delta f/f \approx 1/N_t$. This is a similar story to the mirror bandwidth: a transducer with fewer finger pairs can align well with a wider range of acoustic wavelengths.

Note also the proportionality with $\epsilon_{\text{eff}} K^2$. We mention above that lithium niobate has a piezoelectric coupling strength K^2 about 50 times that of quartz and gallium arsenide. It also has a much higher dielectric constant ϵ_{eff}, about 10 times higher. This makes its admittance response overwhelmingly larger for the same geometry. For this reason, lithium niobate devices can work well with relatively few finger pairs ($N_t \sim 10$), allowing devices with a wide bandwidth. On the other hand, quartz typically devices require many more finger pairs ($N_t \sim 100$), resulting in narrow bandwidth.

2.2.3 Fabry-Pérot resonators

The easiest way to construct a surface acoustic wave resonator is to place two mirrors relatively far apart (distance $L_r \sim 100\lambda$) and place a wide-bandwidth transducer (several finger pairs) in the middle. This acts analogously to an optical Fabry-Pérot resonator. The first relevant frequency range is the mirror stop band. In that band, acoustic waves are efficiently reflected by the mirrors, creating an "echo chamber" where the waves can bounce back an forth. At certain frequencies, these reflections interfere constructively, bringing about electromechanical resonances. Since the mirrors are relatively far apart in space, these resonances will be relatively close together in frequency, with frequency

spacing roughly v/L.[7] We previously showed such a resonator in Fig. 2.2. We will discuss these in more detail below in the context of some experiments.

2.2.4 Single-mode resonators

For the quantum experiment in chapter 5, we just want to couple to *one* electromechanical resonance. To keep things simple, we can construct a resonator designed to have a single mode in the ≈100 MHz mirror bandwidth. This overall makes the experiment easier and also increases the coupling somewhat. The main price is lower quality factor, as the mirrors are more lossy than the open surfaces featured in the multimode Fabry-Pérot designs.

They are also somewhat more difficult to design. The fundamental idea is simple: bring the mirrors closer together so that the frequency spacing between the modes exceeds the mirror stop bandwidth. The difficulty is mainly because the phase of the mirror reflection is somewhat complicated (see Fig. 2.3). It is not simply 0° or 180° as one might expect, and it is frequency-dependent. We also must take into account the internal reflections inside the transducer. Without careful consideration, it is possible to end up with zero or two modes instead of one.

In our design, we adopt a continuous grating structure where the transducer and mirrors are right next to each other [30]. In addition to considering the reflections in the transducer and the phase of the mirror reflection, we also need to compensate for

[7]This is for the case that the transducer only couples to one mode symmetry (even or odd with respect to the center of the resonator); the actual free spectral range for *all* modes is $v/(2L)$.

the differing effective speeds in the transducer and mirrors. We use parameters from cryogenic measurements of the easier Fabry-Pérot resonators and a reliable numerical model to design our single-mode resonator (see appendix A). See Ref. [41] for a parallel discussion of designing this type of resonator.

2.3 Classical experiments

We have discussed surface acoustic wave resonators from a theoretical point of view, but before we can tackle the quantum experiment in chapter 5, we perform some simple classical measurements to establish a good understanding.

2.3.1 Room temperature measurements

Fortunately, most of these devices work at room temperature, although there is substantial ohmic loss in the very thin (25 nm to 30 nm) aluminum films, especially in the long, narrow transducer lines. We use a probe station outfitted with microwave probes (GGB Picoprobe 40A) to conduct fast, calibrated measurements of many devices. This is shown in Fig. 2.5a. In the next few sections, we explore measurements of those devices.

We conduct a short/open/load/through calibration of the two probes using a vector network analyzer and a dedicated calibration substrate (GGB CS-5) with precise calibration standards. This allows us to remove the effects of the SMA interfaces, cables, and probes from our vector network analyzer measurements. We show an example calibration standard being measured in Fig. 2.5b. In Fig. 2.5c, we show an example of a

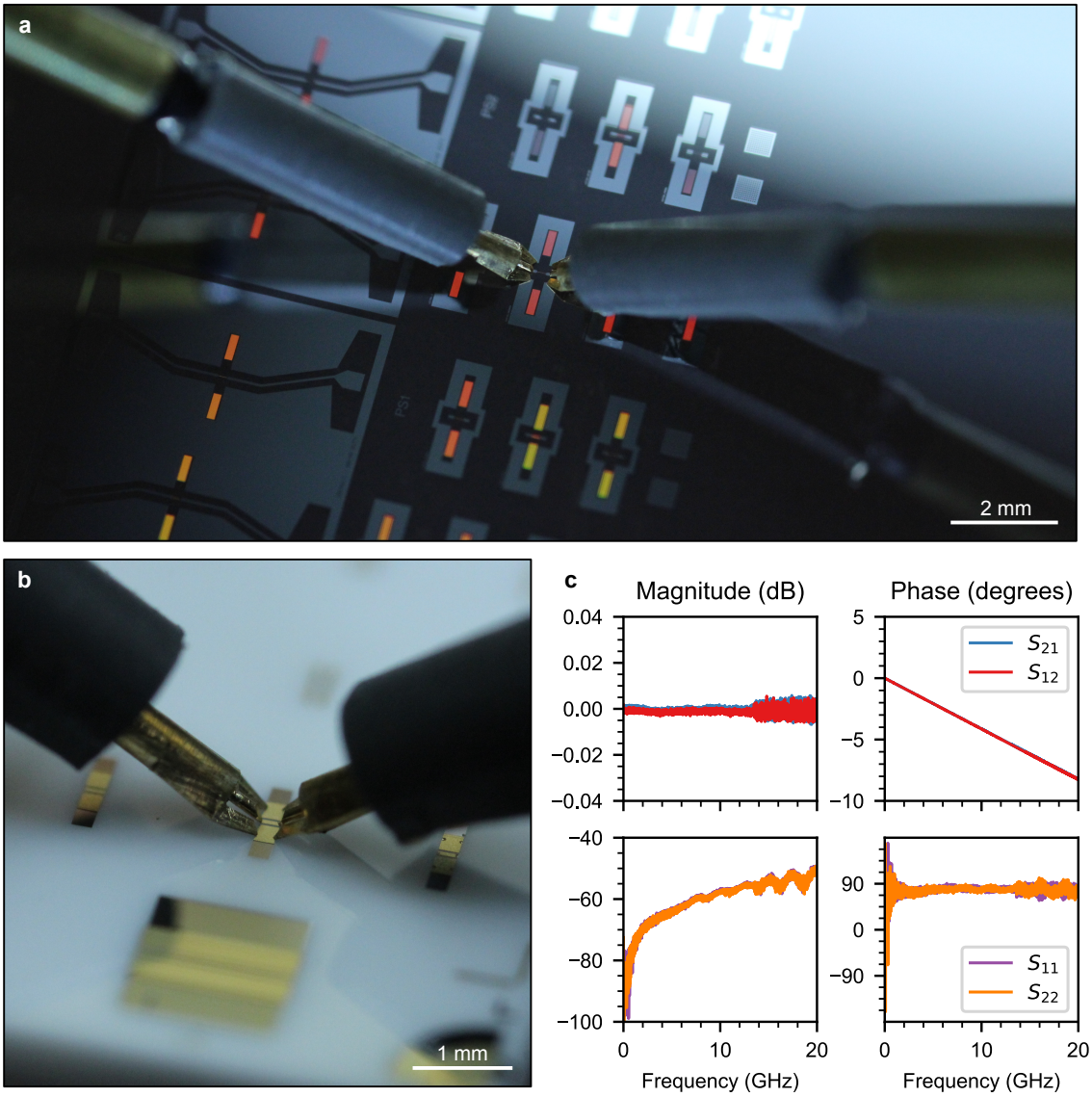

Figure 2.5: **Room temperature measurements with microwave probes. a,** Photograph of two microwave probes measuring transmission through the transducer of a Fabry-Pérot resonator. The red/orange colors are from optical diffraction. **b,** Probes measuring a calibration standard, in this case a "through" 50 Ω transmission line. **c,** Example validation measurement. Following the calibration measurements, we reposition the probes on a "through" 50 Ω transmission line and measure it. The results are very close to the ideal values. We plot all four S_{ij} parameters: magnitude on the left, phase on the right, transmission (S_{21}, S_{12}) on the top, and reflection (S_{11}, S_{22}) on the bottom. This is raw data directly from the network analyzer following calibration. The manufacturer states the electrical delay through this transmission line is 1.13 ps, which gives a phase shift of $-8°$ at 20 GHz.

validation measurement where, after calibration, we re-measure the "through" standard. We find that this calibration gives excellent results for measurements of all four scattering parameters S_{ij}. These-high quality measurements were instrumental to developing a quantitative understanding of these devices (and many other electromechanical and microwave devices).

2.3.2 Modeling experimental results

It is very useful to construct a simple but comprehensive model of these devices. This allows us to understand the experiments and also is essential to designing more complicated devices, such as single-mode resonators. We use a standard approach for modeling SAW devices, the P-matrix [66]. For detailed information about P-matrices, see appendix A. The core idea is to construct 1-dimensional electromechanical models of individual components (like mirrors, transducers, and open space) and then cascade them together to make a more complicated device like a resonator. We use robust, established electromechanical models, together with design parameters and material properties. In practice, we fine-tune the material property values to fit models to experimental data.

We walk through the modeling process in Fig. 2.6. We present the calibrated transmission S_{21} measured through a transducer in a resonator, as depicted in Fig. 2.5a. Fig. 2.6a shows the transmission over a wide frequency range. We fit this to a series RLC embedding circuit. Most of this impedance is actually inside the transducer. The capacitance is dominated by the interdigital capacitance of the transducer, and the re-

sistance and inductance is dominated by the thin, narrow fingers. However, we keep the model simple by putting the resistance and inductance in lumped elements in series with the SAW device model. We observe that the fitted capacitance is somewhat lower than the design value (about 30% lower), which we attribute to the distributed resistance in the fingers.

We then move to a more sophisticated model by including the admittance of the transducer alone (as if the mirrors weren't there), as shown in Fig. 2.6b-c. This is put in the circuit as an acoustic admittance $Y_a(\omega)$ in parallel with the capacitor. We refine the RLC embedding circuit and adjust the effective speed v_t of the transducer.

Finally, we add the mirrors, using a much more complicated $Y_a(\omega)$ constructed from our P-matrix model. We adjust the effective speed in the open space (v_s) and mirrors (v_m), the reflection per line in the mirror r, and the loss in the open space (η_s) and mirrors (η_m) (see appendix A). In these devices, the transducer is very small ($N_t = 5$ finger pairs), so we use a very simple non-reflective model. This is shown in Fig. 2.6d, where we zoom on the resonant region. We observe good agreement between the experiment and model.

We can learn more about the device by peeling apart the components of our model from Fig. 2.6c and looking at them individually. This allows us to escape the details of the embedding circuit and the scattering matrix and instead focus on the SAW behavior. We do so in Fig. 2.7. In Fig. 2.7a, we replot the experimental transmission magnitude $|S_{21}|$. In Fig. 2.7b, we show the real part of the acoustic admittance of the models. Each peak from the full model corresponds to a resonance.[8] We also look at the transducer

[8]The peaks in the admittance are actually local maxima in $|S_{21}|$, but there are corresponding

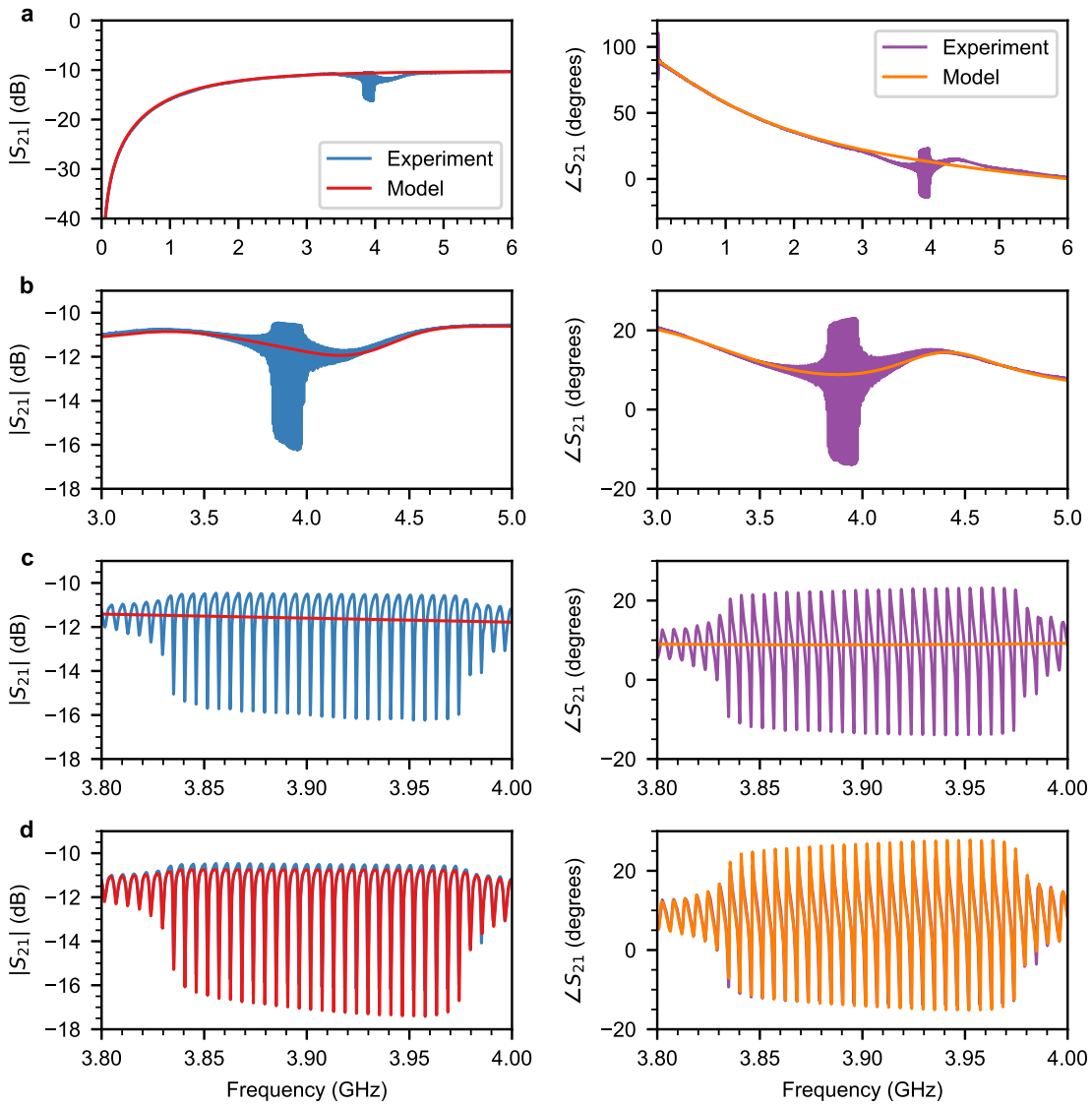

Figure 2.6: **Fitting transmission through a surface acoustic wave resonator.** Apply models to calibrated vector network analyzer measurement of a device pictured in Fig. 2.5a. Left: Transmission magnitude $|S_{21}|$. Right: Transmission phase $\angle S_{21}$. **a,** Wide-frequency plot with the simple RLC model (transmission through a series RLC). **b-c,** With the RLC model incorporating the transducer admittance (but not the mirrors). **c,** With the complete model.

alone. Since it only has $N_t = 5$ finger pairs, it has a very broad bandwidth, around 1 GHz. By design, its response is basically uniform over the frequency range of interest. The resonances in Fig. 2.7a-b come about from the mirrors. Interference among reflected waves frustrates the transducer response except at the resonance frequencies, where it is enhanced. This is quite clear looking at Fig. 2.7c, where we plot the magnitude of the mirror reflection. The stop band coincides with the frequency range where the resonances occur.

This modeling technique will resurface in chapter 5, where we use a superconducting qubit to measure the frequency dependence of a SAW resonator and then model its response.

2.3.3 Varying parameters

Here, we discuss several different device designs. We focus on the devices shown in Fig. 2.5a.[9] We can fit each of these with similar fidelity to the model described at length in the previous section, just updating the design parameters, adjusting the embedding RLC (accommodating variation in probe contact resistances and transducers), and slightly adjusting the various material properties (less than 1%). For clarity and simplicity, we just plot the transmission magnitude $|S_{21}|$ of the experimental data. This emphasizes the main lesson from each experiment. However, in analyzing these experiments quantitatively, it is critical to include the transmission phase.

impedance peaks that go with the dips in $|S_{21}|$.

[9] We also performed rather comprehensive experiments with 700 MHz devices. Later efforts were more focused on cryogenic measurements, although we still measured many devices at room temperature.

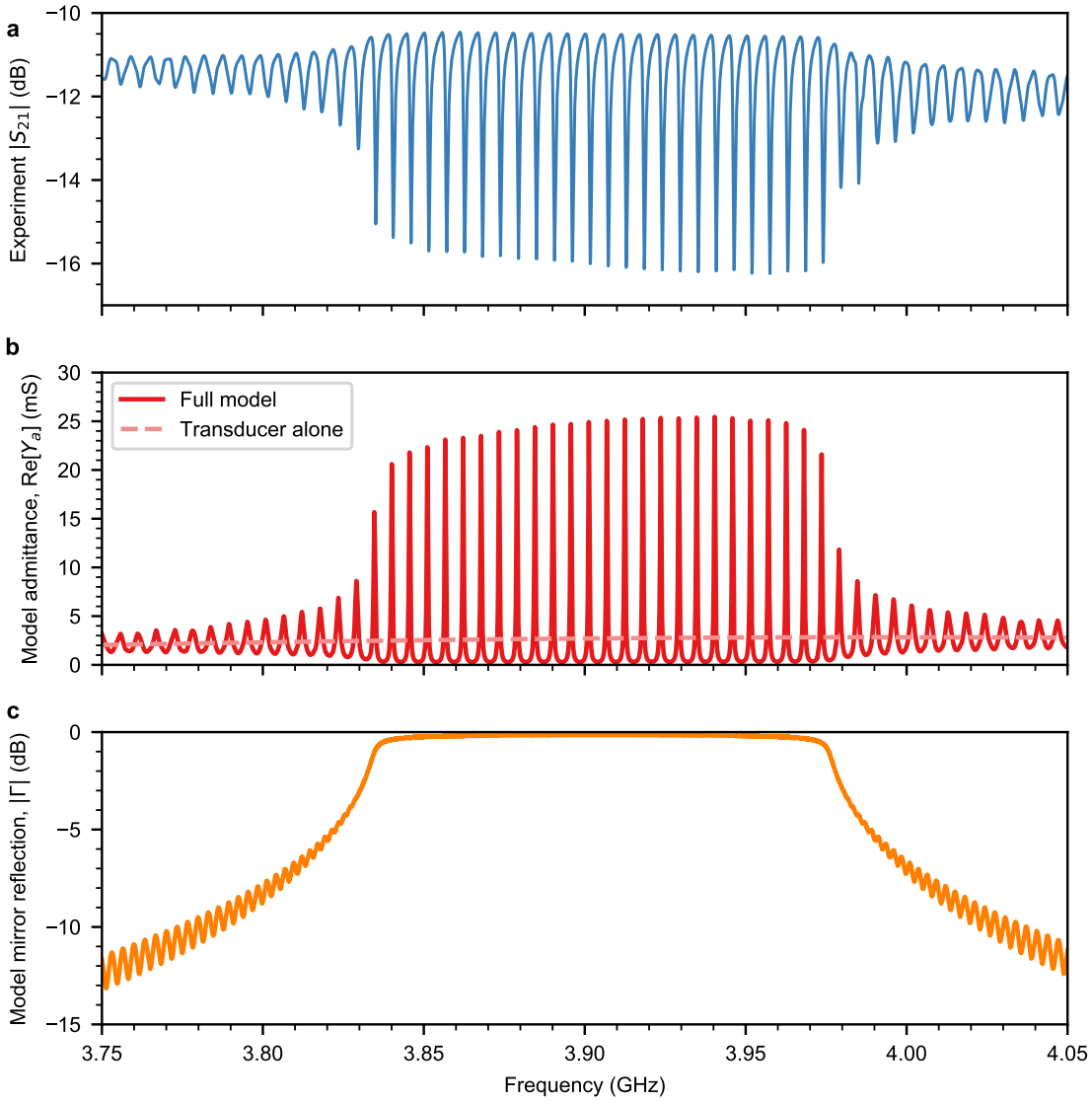

Figure 2.7: **Model of a surface acoustic wave resonator.** Examination of the model developed in Fig. 2.6. **a,** Experimental transmission magnitude $|S_{21}|$ associated with the model. **b,** Real part of the acoustic admittance Y_a for the full model (with many peaks) and the transducer alone (approximately constant) **c,** Magnitude of the mirror reflection Γ.

Distance between mirrors

As we discuss above, the distance between the mirrors determines the frequency spacing between the resonances. It also affects the electromechanical coupling: if we keep the same transducer and bring the mirrors closer together, a larger fraction of the device is covered by the transducer, so the electromechanical coupling is stronger. We show a simple experiment in Fig. 2.8. Decreasing the distance between the mirrors makes the resonances deeper (due to stronger coupling) and further apart in frequency, as expected.

Mirror pitch

In these devices, the transducer has a very large bandwidth; the frequency range where the resonances occur is determined by the mirror stop band. In Fig. 2.9, we show two devices with slightly different mirror periods, shifting the mirror stop band as expected.

Mirror duty cycle

The mirror duty cycle should have a substantial effect on the piezoelectric reflections [66]. We test this here, shown in Fig 2.10. As expected (with open-circuit mirrors), we see the strongest reflections with the 60/40 duty cycle (wider metal lines). This manifests itself in the larger stop bandwidth.

These large $\approx$100 MHz bandwidths are very convenient, and they are possible thanks to the strong piezoelectric coupling in lithium niobate. We also note that larger $|r|$ (and hence stop bandwidth) is not universally beneficial; if $|r|$ is pushed too far, it can bring about excessive scattering into bulk modes. We also suspect that the metal film and

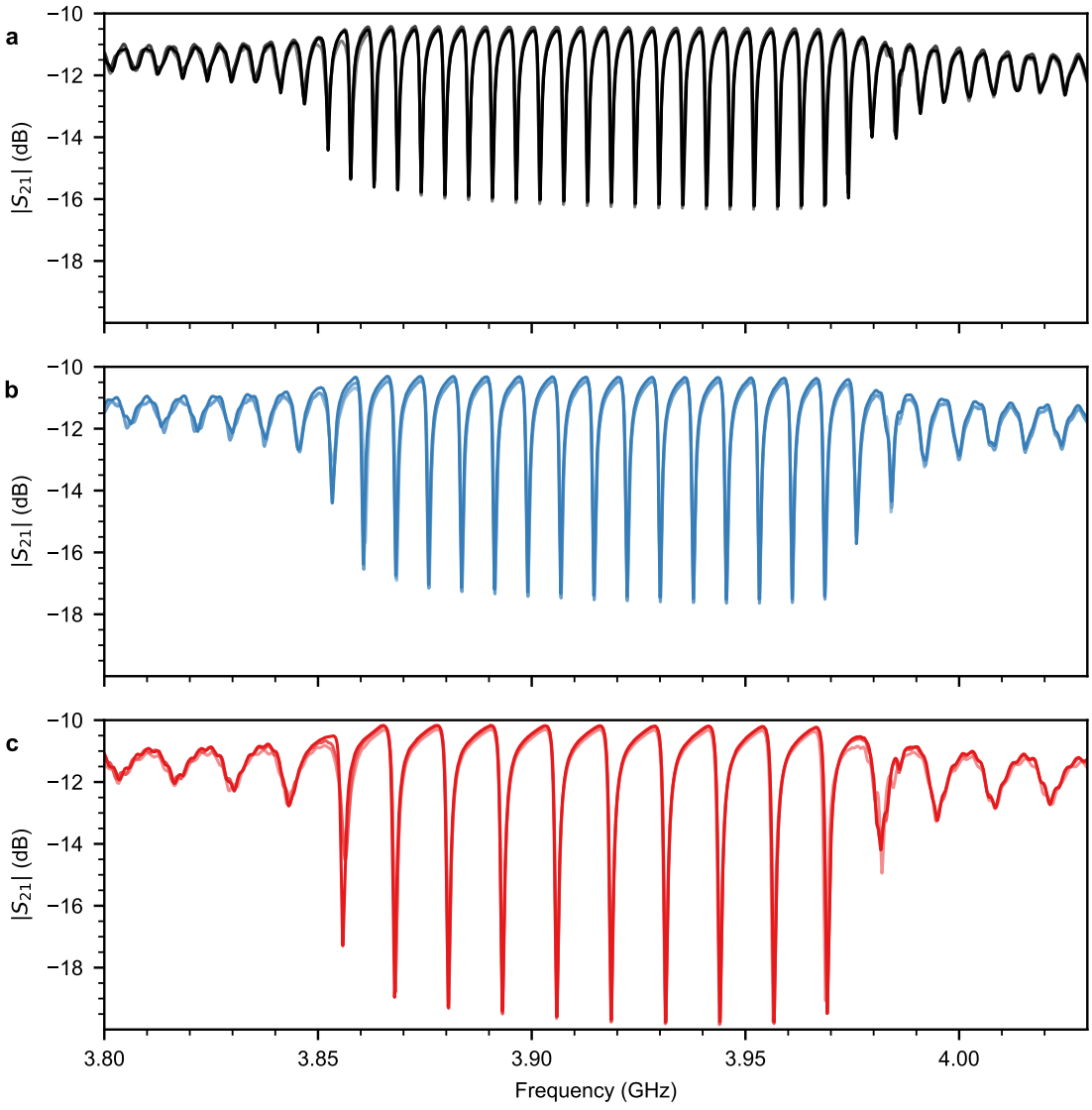

Figure 2.8: **Resonators with different distances between the mirrors.** Calibrated vector network analyzer measurements of devices pictured in Fig. 2.5a. Three devices of each type are plotted together in different shades. **a,** 700 µm. **b,** 500 µm. **c,** 300 µm.

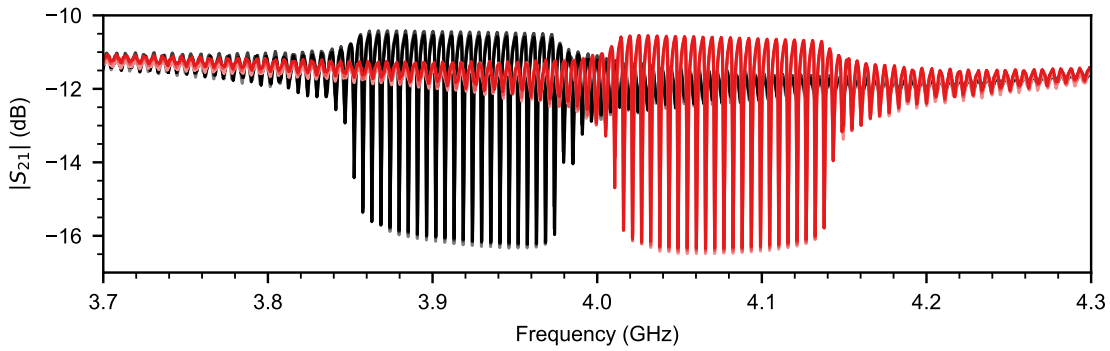

Figure 2.9: **Resonators with different mirror periods.** Calibrated vector network analyzer measurements of devices pictured in Fig. 2.5a. Three devices of each type are plotted together in different shades. Black: 0.50 µm. Red: 0.48 µm.

associated interfaces are lossier than the empty surface.

2.3.4 Cryogenic measurements

Cryogenic measurements are much more involved; we wirebond a chip into a sample mount and cool it down in a dilution refrigerator (see appendix D). As the devices cool down, we observe much lower loss thanks to superconductivity and diminished material loss. We show measurements of an example device in Fig. 2.11, one of the square dies on the left side of Fig. 2.5a. This device has the same design as the device in Fig. 2.10a. Note the much deeper dips: the typical quality factor increases from about 4×10^3 at room temperature to 4×10^4 at 7 mK. We also observe that at low power, such that the mean phonon number is around 1, the quality factor diminishes to about 2×10^4. This is consistent with related experiments on quartz [61]. Another interesting feature is that the lower-frequency resonances exhibit unexpected splitting, as though we couple

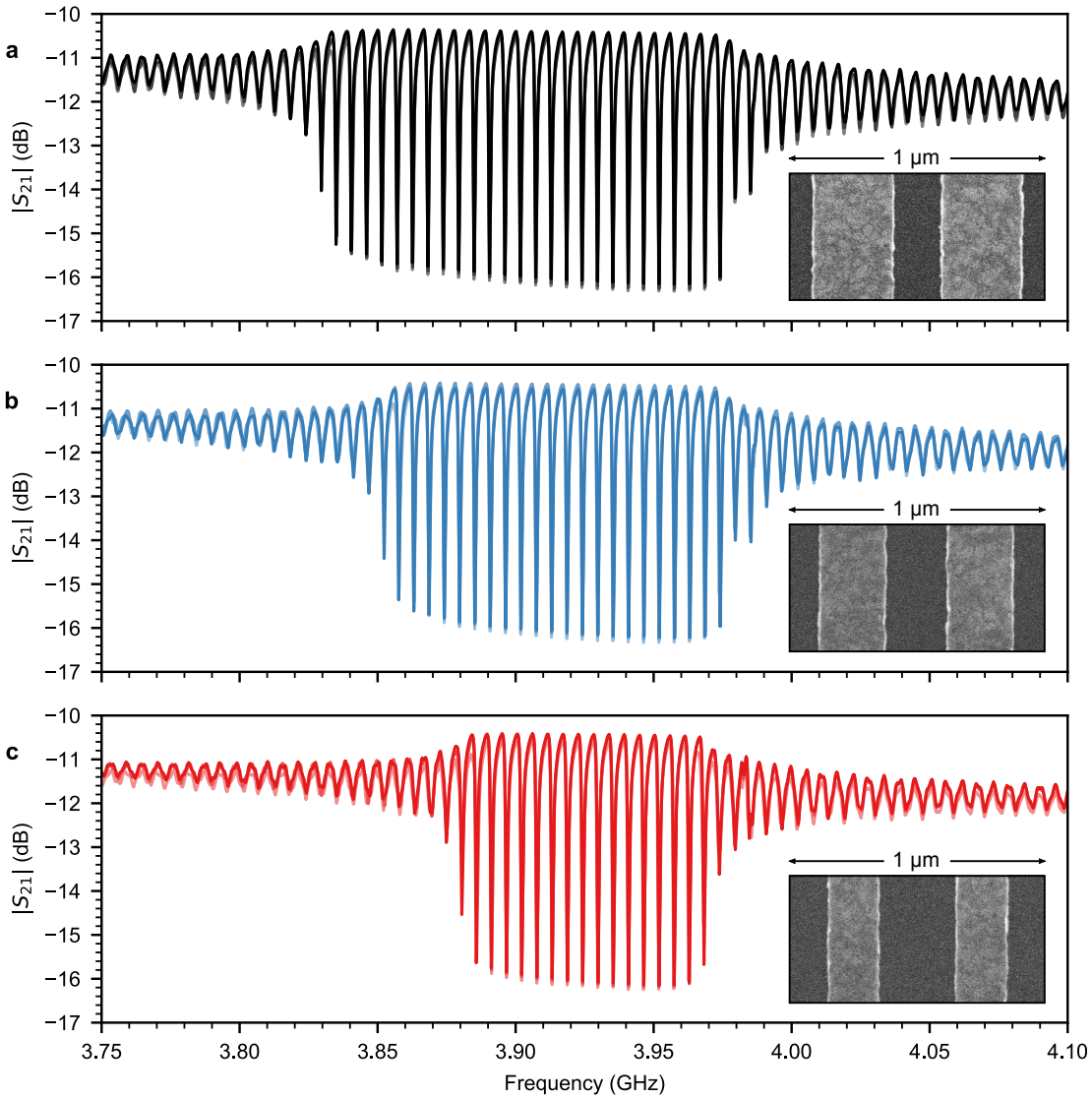

Figure 2.10: **Resonators with different mirror duty cycles.** Calibrated vector network analyzer measurements of devices pictured in Fig. 2.5a. Three devices of each type are plotted together in different shades. Insets: Scanning electron micrographs showing one wavelength (two periods) of each grating of aluminum lines. **a,** 60/40 (metal/space). **b,** 50/50. **c,** 40/60.

to a family of spurious modes. This could be investigated further using a 2-dimensional generalization of the P-matrix model techniques [92].

2.3.5 Other measurement configurations

All of these experiments measure transmission *through* the transducer, from one electrode to the other. Alternatively, we can have an uninterrupted transmission line with one end of the transducer connected to the transmission line and the other end grounded. This is called a "tee" network, and it is pictured in Fig. 2.12.

The "tee" configuration has several benefits. First, we ordinarily have high transmission through the transmission line, just slightly loaded by the transducer capacitance to ground. In principle, this could allow frequency multiplexing, with several devices on one transmission line (like the coplanar waveguide resonator experiment in chapter 4). In the "through" configuration, dips in $|S_{21}|$ correspond to *impedance* maxima, while in the "tee" configuration, dips correspond to *admittance* maxima. As we discuss below, we are ultimately interested in the admittance maxima, and those are emphasized in the "tee" configuration. This works very well for cryogenic measurements, where the aluminum is superconducting. However, we observe that for room temperature measurements, ohmic loss substantially damps the admittance maxima, so the "through" configuration is typically better for room temperature measurements.

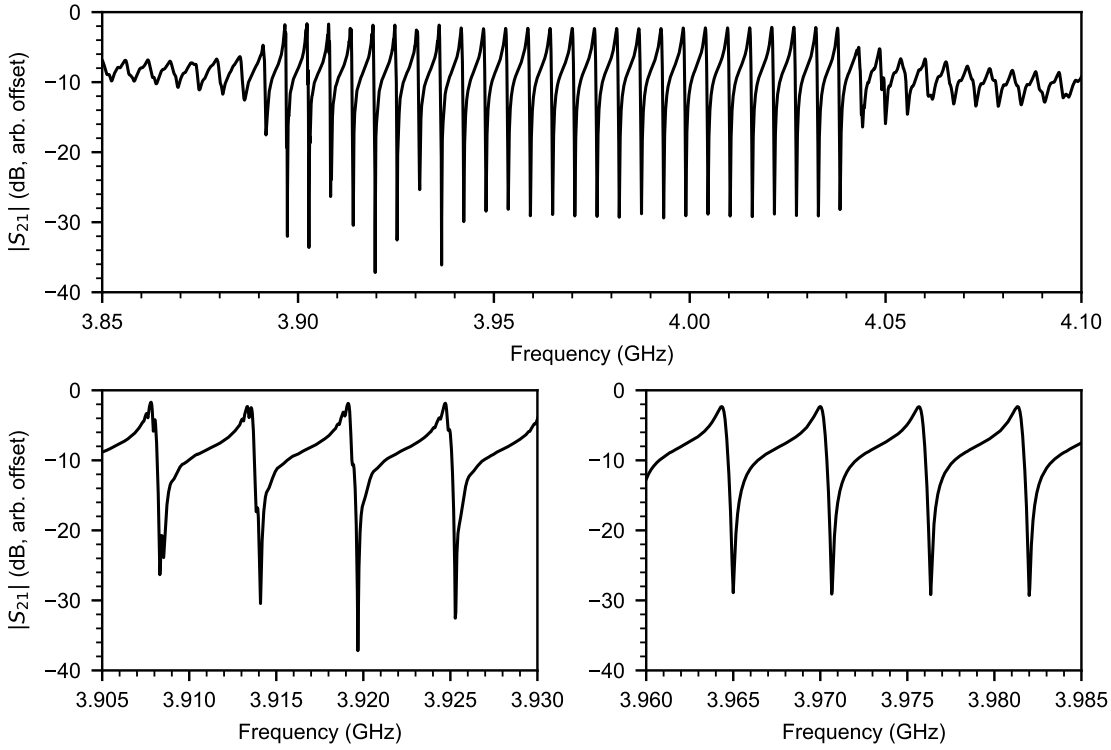

Figure 2.11: **Cryogenic measurements of SAW resonances.** Microwave transmission magnitude $|S_{21}|$ through the sample with arbitrary offset from attenuation and amplification. Note that the transmission phase, not pictured, is also very important to analyze. Top: Broad scan showing the full stop band. Lower left: Zoomed-in scan of several lower-frequency resonances showing the unexpected splittings. Lower right: Zoomed-in scan of central resonances.

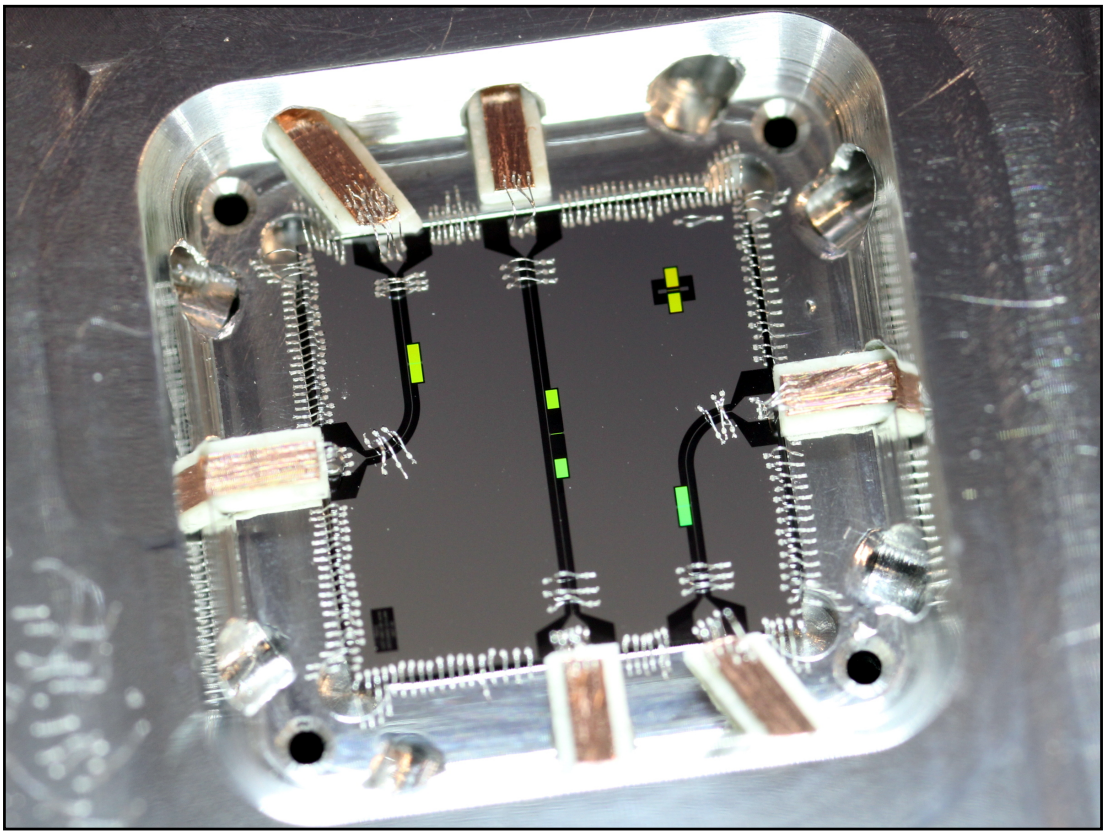

Figure 2.12: **Tee measurement configuration.** Photograph of a wirebonded sample with four resonators. Upper right: For room temperature measurement. Center: Fabry-Pérot style resonator. Upper left and lower right: Single-mode resonator prototypes. The chip is a 6 mm square.

2.4 Considerations for coupling to a qubit

Our goal is to couple one of these surface acoustic wave resonances to a superconducting qubit. As we mention earlier, several previous experiments have attempted this [38, 62, 65]. The approach was to use a weak piezoelectric substrate (quartz or gallium arsenide) as a compromise so the qubit and SAW device could inhabit the same substrate. To get strong coupling despite the weak piezoelectricity, the interdigital transducer is made an integral part of the qubit, constituting much of its capacitance. This is a reasonable approach, and it is also similar to the experiments coupling superconducting qubits to bulk waves, where the aluminum nitride in the transducer participates in the qubit capacitance [70, 20]. However, it imposes some difficulties for the qubit. The fine interdigital geometry is empirically quite lossy for qubits, and the piezoelectric substrate presents loss as well. Moreover, the qubit is always exposed to the transducer, which can bring about loss over a wide frequency range.

We pursue an alternative, establishing a separation between the qubit and transducer so that the transducer does not participate in the qubit capacitance. Further, we use tunable coupling so that the qubit and transducer can be isolated from each other on demand. These ideas will be explored in more detail in the coming chapters.

2.4.1 Series and parallel resonances

Superconducting qubits are circuits, so it would be useful to pursue a simple circuit model for our resonator. As we mention earlier, these electromechanical resonances have

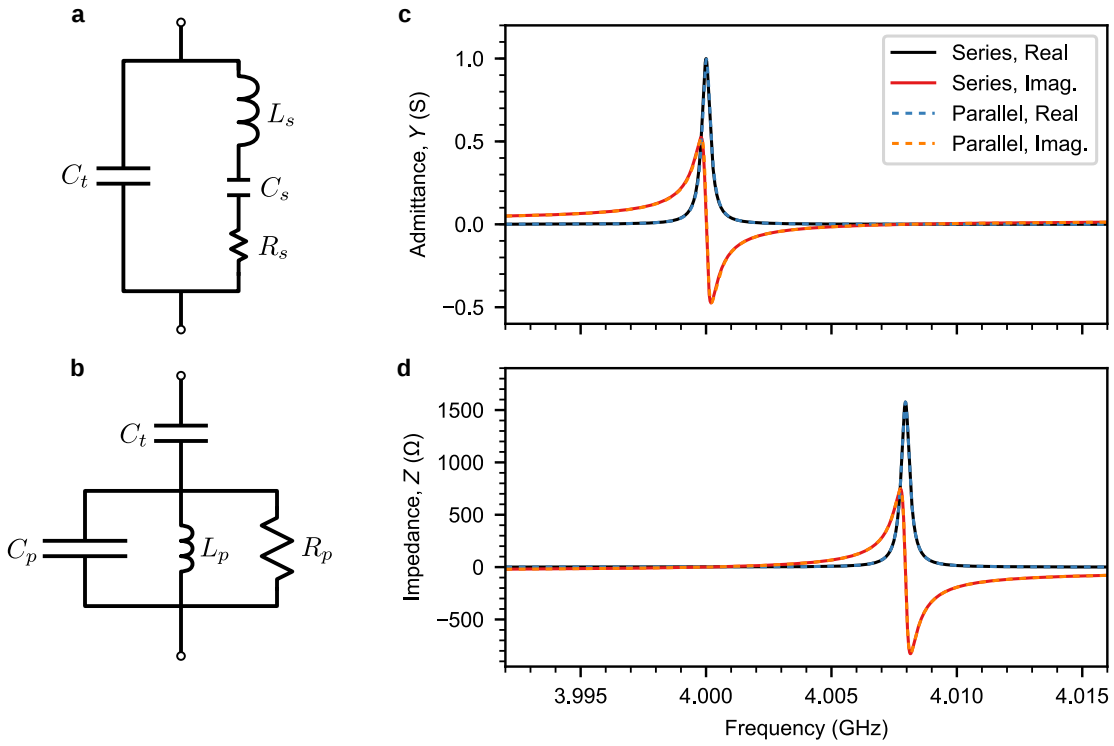

Figure 2.13: **Equivalent circuits for electromechanical resonances. a,** Butterworth-Van Dyke circuit model with a series RLC in parallel with the transducer capacitance. **b,** "Parallel BVD" circuit model with a parallel RLC in series with the transducer capacitance. **c,** Calculated admittance Y (real and imaginary parts) using each circuit model, starting from $\omega_s/2\pi = 4\,\mathrm{GHz}$, $Z_s = 10\,\mathrm{k\Omega}$, $Q = 10^4$, and $C_t = 1\,\mathrm{pF}$. **d,** Calculated impedance $Z = 1/Y$ using each circuit model (same parameters as **c**). As indicated in the legend, the black and red solid lines show the BVD, and the blue and orange dashed lines show the parallel BVD. They are in close agreement.

corresponding peaks in admittance and impedance at slightly different frequencies. The admittance peaks occur at the mechanical eigenfrequencies, and the impedance peaks are pulled slightly higher by the transducer capacitance. Here, we discuss two simple circuit models with very similar behavior.

Traditional Butterworth-Van Dyke Model

The first is the Butterworth-Van Dyke (BVD) model [15, 29], shown in Fig. 2.13a. The transducer capacitance C_t is in parallel with a series resonant circuit of R_s, L_s, and C_s. This is easy to generate from the acoustic admittance $Y_a(\omega)$; the series RLC is simply a fit to a peak in the acoustic admittance [66]. This is readily generalized to multiple modes by adding more series resonant circuits in parallel. This perspective emphasizes the series resonance (that is, the admittance peak), which has characteristic impedance $Z_s = \sqrt{L_s/C_s}$ and angular frequency $\omega_s = 1/\sqrt{L_s C_s}$. However, the circuit also has an impedance peak, which occurs when the RLC admittance cancels out the transducer capacitor admittance.

In our experiment, we want to avoid allowing the transducer to participate in the qubit capacitance, and we want tunable coupling; both of these point toward inductive coupling. This works most naturally coupling to a series resonance, so for our purposes, the traditional Butterworth-Van Dyke circuit is a good choice.

Parallel Butterworth-Van Dyke Model

There is a complementary circuit we wish to mention, which we will refer to as the "parallel BVD," depicted in Fig. 2.13b. The transducer capacitance C_t is in series with a parallel resonant circuit of R_p, L_p, and C_p. In this perspective, we emphasize the parallel resonance (that is, the impedance peak), which has characteristic impedance $Z_p = \sqrt{L_p/C_p}$ and angular frequency $\omega_p = 1/\sqrt{L_p C_p}$. This is a good way to look at an

electromechanical resonance when using capacitive coupling.

These two circuits are *not* precisely equivalent, but they are very close.[10] We show an example in Fig. 2.13. We can transform between the two circuits working under the assumption that the quality factors $Q_s = \sqrt{L_s/C_s}/R_s = Z_s/R_s$ and $Q_p = R_p/\sqrt{L_p/C_p} = R_p/Z_p$ are equal.[11] For example, we transform from a traditional BVD (C_t, R_s, L_s, C_s) to a parallel BVD (C_t, R_p, L_p, C_p). The parallel resonance angular frequency ω_p is given by

$$\omega_p^2 = \frac{1}{L_p C_p} = \frac{1}{L_s C_s}\left(1 + \frac{C_s}{C_t}\right). \tag{2.9}$$

Immediately, we have the product $L_p C_p$. At this frequency, we demand that both models give impedance $1/(i\omega_p C_t) + R_p$, implying

$$R_p = \frac{1}{\omega_p^2 C_t^2 R_s}. \tag{2.10}$$

Finally, assuming $Q_s = Q_p = Q$, we obtain

$$Z_p = \frac{R_p}{Q} = \frac{1}{\omega_p^2 C_t^2 R_s Q} = \frac{1}{\omega_p^2 C_t^2 Z_s}, \tag{2.11}$$

giving us the quotient $L_p/C_p = Z_p^2$. This completes the transformation. We observe good agreement between the circuit models, with the series resonance clearly displayed in the admittance, and the parallel resonance clearly displayed in the impedance.

If we consider the experiment of O'Connell et al. [70], for example, using this model makes the circuit analysis much simpler. Ignoring the resistors, we start with a traditional BVD based on the parameters from their Fig. 1: $C_t = 0.19\,\mathrm{pF}$, $L_s = 1.043\,\mu\mathrm{H}$, and

[10] Our transformation becomes worse with low quality factors; the two circuits agree on ω_p but start to disagree on ω_s.

[11] This is not necessarily the case, especially in strongly-coupled surface acoustic wave devices. For example, when the series and parallel resonances are at substantially different frequencies, they see different mirror reflections Γ.

$C_s = 0.655\,\text{fF}$. Using Eqn. 3.31 of Ref. [71] with a qubit capacitance $C_q = 1\,\text{pF}$ and coupling capacitance $C_c = 0.5\,\text{pF}$, we calculate coupling $\Omega/2\pi = 106\,\text{MHz}$.[12]

Using the transformation above, we arrive at $L_p = 12.33\,\text{pH}$ and $C_p = 55.21\,\text{pF}$. Using the parallel BVD, the circuit looks like two parallel LC circuits (the qubit, and L_p with C_p) connected by a capacitance, the series combination of C_c and C_t. Then we can use our Eqn. 3.21 to calculate $\Omega/2\pi = 2g/2\pi = 106\,\text{MHz}$, in agreement.

2.4.2 Piezoelectricity and characteristic impedance

We will discuss inductive coupling in more detail in the coming chapters, but here we discuss it in the context of designing our surface acoustic wave resonator. The relevant parameter is the characteristic impedance of the series RLC equivalent circuit to our resonance, $Z_s = \sqrt{L_s/C_s}$. The inductive coupling strength is larger for smaller characteristic impedance, or larger series capacitance C_s (see chapter 3). The series capacitance is roughly proportional to the piezoelectric coupling strength K^2 times the transducer capacitance [66]. As discussed above, both of these are much larger for lithium niobate than quartz or gallium arsenide; the product $K^2\epsilon_{\text{eff}}$ is about 500 times larger. This immensely improves the coupling. The consequence is that we can have a relatively noninvasive coupling circuit between the qubit and resonator while still achieving strong coupling. This allows us to achieve the desired separation and isolation for the qubit.

[12] This Ω is equal to $2g$ the way we define g in chapters 3 and 5.

Chapter 3

Superconducting qubits

A superconducting quantum bit (qubit) [26] is the key ingredient to generating and measuring quantum states in our experiments. We can use classical control pulses to manipulate and measure the quantum state in a qubit, and coupling it to a surface acoustic wave resonator enables experiments with nonclassical states of motion. In this chapter, we describe the essential features of the qubit we will use in chapter 5.

3.1 Overview

Qubits [76] are two-level quantum systems which we can control and measure. We will identify two basis states, $|g\rangle$ and $|e\rangle$, referring to the ground state and first excited state of a real system. The quantum state $|\psi\rangle$ of a qubit can be an arbitrary superposition of those two states (or, more generally, a statistical mixture of states).

Superconducting qubits are made from electromagnetic resonators with very low losses

at cryogenic temperatures. A low temperature $T \sim 10\,\mathrm{mK}$ gives us two important properties: minimal loss thanks to superconductivity ($k_B T \ll \Delta$, where Δ is the superconducting gap of the relevant material), and cooling the circuits to the quantum ground state ($k_B T \ll \hbar\omega_0$, where ω_0 is the angular frequency of the resonance).

3.1.1 Ideal qubits

An ideal qubit is a perfect two-level system. It can be mapped to a spin-$\frac{1}{2}$ particle in a magnetic field; we construct operators from the Pauli operators σ_x, σ_y, and σ_z. A simple Hamiltonian is

$$H = -\frac{1}{2}\hbar\omega_q\sigma_z, \tag{3.1}$$

where the eigenstates are $|g\rangle = |\uparrow_z\rangle$ (spin up along z) and $|e\rangle = |\downarrow_z\rangle$ (spin down along z). Another way to express this is with $\sigma_\pm = (\sigma_x \mp \sigma_y)/2$, where (neglecting an irrelevant constant offset)

$$H = \hbar\omega_q\sigma_+\sigma_-. \tag{3.2}$$

Jaynes-Cummings model

The Jaynes-Cummings model [44, 40, 88] describes interactions between a two-level system and a harmonic oscillator, typically cast as an atom with dipole moment $d \sim \sigma_- - \sigma_+$ in an electric field $E \sim a - a^\dagger$. We use this model to understand the interactions between a qubit and a mechanical resonator, and also separately for qubit readout. The coupling

Hamiltonian has the basic form $H_c \sim -d \cdot E$; here we use the simple form

$$H_c = -\hbar g(\sigma_- - \sigma_+)(a - a^\dagger) = \hbar g(-\sigma_- a + \sigma_- a^\dagger + \sigma_+ a - \sigma_+ a^\dagger), \tag{3.3}$$

where g is the coupling strength, incorporating the prefactors from d and E.[1] We will use the rotating-wave approximation, in which we neglect the $\sigma_- a$ and $\sigma_+ a^\dagger$ terms.[2] We arrive at the full Jaynes-Cummings Hamiltonian in the rotating-wave approximation,

$$H_{\mathrm{JC}} = \hbar\omega_r a^\dagger a - \frac{1}{2}\hbar\omega_q \sigma_z + \hbar g(\sigma_- a^\dagger + \sigma_+ a), \tag{3.4}$$

where we include the harmonic oscillator (ω_r, a) and qubit (ω_q, σ) along with the coupling term. This is the form we use to describe the interaction between a qubit and a mechanical resonator in chapter 5.

In some circumstances, we deliberately keep the qubit and oscillator detuned by angular frequency Δ, so $\omega_q = \omega_r + \Delta$. If $\omega_r \gg |\Delta| \gg |g|$, we are in the so-called "dispersive limit." We use this for qubit readout, where we couple the qubit to a detuned electromagnetic resonator. We can use these approximations to recast Eqn. 3.4 following an expansion in g/Δ, arriving at [88, 85]

$$H_d = \hbar\omega_r a^\dagger a - \frac{1}{2}\hbar\omega_q \sigma_z - \hbar\frac{g^2}{\Delta}\sigma_z a^\dagger a. \tag{3.5}$$

[1] Unfortunately, there is a collision of notation between the qubit ground state $|g\rangle$ and the coupling strength g.

[2] This is on the basis that the qubit and oscillator frequencies are fairly close together, so those processes are highly nonresonant (adding or removing two excitations at once). On the other hand, the $\sigma_- a^\dagger$ and $\sigma_+ a$ terms are close to resonant (swapping an excitation between the qubit and oscillator). This is a good approximation for the experiments in this thesis, although sometimes these terms can be important [84].

We define the dispersive shift[3] $\chi = -g^2/\Delta$. There are two useful interpretations of this.

$$H_d = \hbar\left(\omega_r + \chi\sigma_z\right) a^\dagger a - \frac{1}{2}\hbar\omega_q\sigma_z \tag{3.6}$$

$$H_d = \hbar\omega_r a^\dagger a - \frac{1}{2}\hbar\left(\omega_q - 2\chi a^\dagger a\right)\sigma_z \tag{3.7}$$

In Eqn. 3.6, we interpret it as a qubit-state-dependent shift of the oscillator frequency; it is pulled $\pm\chi$ depending on the qubit state. We will use this to measure the qubit state. In Eqn. 3.7, it is the *qubit* frequency that shifts; it is pulled $-2\chi n$, where n is the number of excitations in the resonator; this is called the "AC Stark shift." This is useful for using the qubit to measure the population of the oscillator, and it is also related to the dephasing the qubit experiences during measurement due to spread in the oscillator population n.

3.1.2 LC resonators

A circuit consisting of an inductor L and capacitor C connected together forms an LC resonator with resonance angular frequency $\omega_0 = 1/\sqrt{LC}$, the circuit realization of the simple harmonic oscillator discussed in chapter 1. Convenient variables are the capacitor charge $Q = CV$ and the inductor flux $\Phi = LI$, with voltage V and current I. This brings about the Hamiltonian

$$H = \frac{Q^2}{2C} + \frac{\Phi^2}{2L}. \tag{3.8}$$

[3]We will need a different formula for a transmon qubit dispersively coupled to a resonator; see below.

Under the right circumstances, this resonator can exhibit quantum behavior, in which case we consider Q and Φ operators. They have the familiar commutation relation

$$[Q, \Phi] = i\hbar, \tag{3.9}$$

and we may transform the Hamiltonian into the convenient form

$$H = \hbar\omega_0 \left(a^\dagger a + \frac{1}{2} \right) \tag{3.10}$$

$$a = \frac{1}{\sqrt{2\hbar}} \left(\sqrt{\frac{C}{L}}\Phi + i\sqrt{\frac{L}{C}}Q \right) \tag{3.11}$$

$$[a, a^\dagger] = 1. \tag{3.12}$$

Transmission line resonators

A convenient way to make a microwave resonator is using a segment of transmission line. In this work, we will use quarter-wave coplanar waveguide resonators [64, 45]. We will discuss one flavor of these in great detail in chapter 4. Here, we just mention that transmission line segments can host electromagnetic resonances. For quarter-wave resonators, the two ends have opposite boundary conditions; one is short-circuited and the other open-circuited. As the name suggests, the fundamental resonance occurs at the frequency where the resonator's length equals one quarter of the electromagnetic wavelength. The input impedance of the resonator looks quite different depending on which end you look into. If the far end is short-circuited, the input impedance near resonance is close to a parallel LC (impedance maximum). On the other hand, if the far end is open-circuited, the equivalent circuit is a series LC (admittance maximum) [75].

We use such a quarter-wave resonator for readout, with the qubit on the open-circuit end (seeing a parallel LC) and the measurement circuit on the short-circuit end (seeing a series LC).

3.1.3 Josephson junctions

The resonances discussed so far are *linear*—all their energy levels are equally spaced. This is problematic for our aspiration to make a qubit, where we focus on just two levels with a unique energy splitting $\hbar\omega_{ge}$. The solution is to incorporate a Josephson junction [48, 49], which acts as a dissipationless nonlinear inductor. There are many different sorts of superconducting qubits; here we will just discuss some Josephson junction basics [53] and introduce the type of qubit we use in this work, the transmon [54, 88, 7, 17].

Junction inductance

In a simple model of a superconductor [53], we describe a condensate of Cooper pairs [6] with an order parameter $\psi(\vec{r})$ with constant magnitude $|\psi(\vec{r})|^2$ equal to the Cooper pair density n. Of interest is the phase ϕ of the order parameter, where $\psi(\vec{r}) = \sqrt{n}e^{i\phi(\vec{r})}$.

A Josephson junction is a small interruption to the superconductor, small enough to allow Cooper pairs to quantum tunnel through it ($\sim$ nm). We implement Josephson junctions using a thin insulating layer of amorphous aluminum oxide between two aluminum electrodes; see appendix E for details. This interruption allows the superconducting phase ϕ to differ on either side; this phase difference δ is very important to the behavior of a Josesphson junction, as is the junction's critical current I_c. We illustrate

this in Fig. 3.1a. These are related to the current I through and voltage V across the junction by the Josephson relations:

$$I = I_c \sin(\delta) \tag{3.13}$$

$$V = \frac{\Phi_0}{2\pi}\frac{d\delta}{dt}, \tag{3.14}$$

where $\Phi_0 = \dfrac{h}{2e}$ is the flux quantum. To get to the inductance, differentiate Eqn. 3.13 with respect to time and substitute the expression for $d\delta/dt$ into Eqn. 3.14, so

$$V = \frac{\Phi_0}{2\pi I_c}\frac{1}{\cos(\delta)}\frac{dI}{dt} = L_j\frac{dI}{dt}, \tag{3.15}$$

defining an effective inductance L_j. We also define $L_{j0} = \dfrac{\Phi_0}{2\pi I_c}$ (the inductance when $\delta = 0$), so $L_j = \dfrac{L_{j0}}{\cos(\delta)}$. This is nonlinear (changing I changes δ and hence L_j) and can take on a wide range of values depending on δ. Josephson junctions also have some capacitance C_j between the electrodes. This can be important, but in this case, we can mostly ignore it. Our qubit has a much larger geometric capacitance in parallel with its junctions. We also use a Josephson junction as a tunable inductor in our coupler circuit (see below); it operates in a regime where its capacitance is not relevant.

DC squids

A DC superconducting quantum interference device (squid) consists of two Josephson junctions in parallel inside a superconducting loop [53]. A symmetric DC squid, composed of two identical junctions a and b with critical current I_j, acts like a single junction whose critical current depends on the external magnetic flux Φ_{ext} through the superconducting

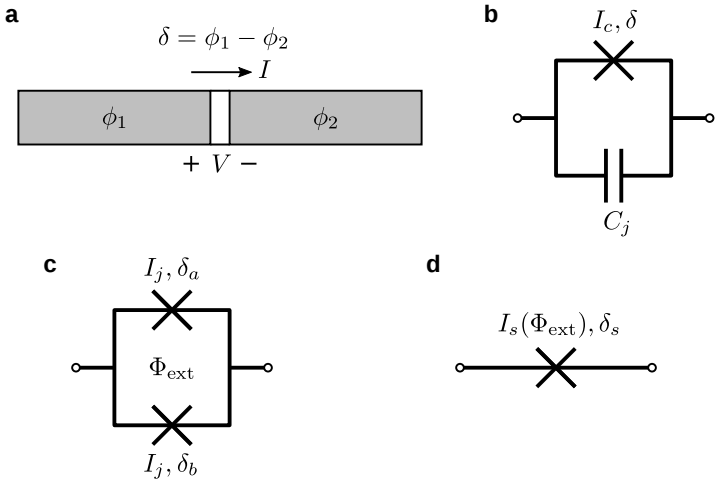

Figure 3.1: **Josephson junctions. a,** Schematic of a tunnel-barrier Josephson junction with phase δ, current I, and voltage V. Two pieces of superconductor (gray) are separated by a thin insulating barrier (white). **b,** Circuit diagram for **a** including the parallel capacitance C_j. **c,** DC squid composed of two symmetric junctions with critical currents I_j, phases δ_a and δ_b, and external flux bias Φ_{ext}. **d,** Equivalent single junction for **c**, where the effective critical current I_s depends on Φ_{ext}.

loop.[4] The effective junction's phase is $\delta_s = (\delta_a + \delta_b)/2$, and the critical current is

$$I_s = 2I_j \cos\left(\pi \frac{\Phi_{\text{ext}}}{\Phi_0}\right). \tag{3.16}$$

This is shown in Fig. 3.1c-d. We will use a DC squid in the qubit to make it frequency tunable.

RF squids

An RF squid consists of one Josephson junction interrupting a superconducting loop, which we use in the context of a tunable inductive coupler [17, 35, 50, 68, 78]. Here, an external magnetic flux Φ_{ext} through the superconducting loop manipulates the phase δ

[4]Some junction asymmetry is inevitable, and it can be quite useful, but we do not employ it here.

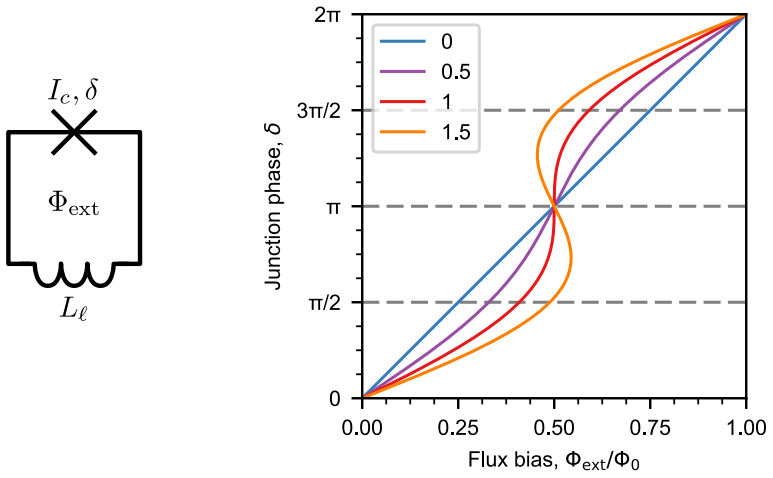

Figure 3.2: **RF squids.** Left: Circuit diagram of an RF squid with loop inductance L_ℓ, junction critical current I_c and phase δ, and external flux bias Φ_{ext}. Right: Plots from Eqn. 3.17 for different values of L_ℓ/L_{j0}, listed in the legend. The junction inductance $L_j = L_{j0}/\cos(\delta)$. The junction becomes high-impedance at $\delta = \pi/2$ and $3\pi/2$, and the junction inductance is $-L_{j0}$ at $\delta = \pi$. For $L_\ell > L_{j0}$, the junction cannot be biased to $\delta = \pi$.

across the junction, tuning its effective inductance L_j. Consider also the inductance L_ℓ of the loop itself. Then the relationship between the phase and the external flux bias is governed by [35]

$$\delta + \frac{L_\ell}{L_{j0}} \sin(\delta) = 2\pi \frac{\Phi_{\text{ext}}}{\Phi_0}. \tag{3.17}$$

We display this graphically in Fig. 3.2.

3.1.4 Transmon qubits

The transmon [54, 88] is a specific type of superconducting qubit where a Josephson junction (I_c) is shunted by a capacitor (C). This is a very successful approach to making

the qubit insensitive to charge noise. Essentially, the qubit energy levels are not changed very much in the presence of an external voltage, so the qubit energy $\hbar\omega_{ge}$ is very stable, substantially increasing the coherence time.

The transmon is governed by the Hamiltonian

$$H = \frac{Q^2}{2C} - \frac{\Phi_0}{2\pi} I_c \cos(\delta). \tag{3.18}$$

Note the similarity to the LC circuit Hamiltonian, Eqn. 3.8. The junction phase δ is closely related to the inductor magnetic flux Φ; they are both time integrals of the voltage. Sometimes, a metaphorical flux $\Phi = \int V(t)\, dt = \frac{\Phi_0}{2\pi}\delta$ is attributed to the junction [85]. As is conventional, we identify a charging energy $E_C = \frac{e^2}{2C}$ and a Josephson energy $E_J = \frac{\Phi_0}{2\pi} I_c$. The transmon design demands $E_J \gg E_C$; this is the condition that makes the qubit insensitive to charge noise. Then the qubit angular frequency $\omega_{ge} = \sqrt{8E_J E_C}/\hbar$.

This circuit is an *anharmonic* oscillator, acting like a particle in a cosine potential rather than a quadratic one. In addition to the ground state $|g\rangle$ and first excited state $|e\rangle$, we also must remember the second excited state $|f\rangle$, and there are yet more states above that. The anharmonicity $\eta = \omega_{ef} - \omega_{ge}$ is determined by the capacitance; $\eta = -E_C/\hbar$. A typical value is around $\eta \approx 2\pi \times (-200\,\mathrm{MHz})$. This nonlinearity allows us to isolate the two lowest levels, realizing a qubit. Note there is a tension between avoiding charge noise ($E_J \gg E_C$) and having sufficient anharmonicity to isolate the lowest two levels (large E_C). Conveniently, charge noise is *exponentially* suppressed in E_J/E_C, which makes it possible to strike a favorable balance. The choice of E_J and E_C is also constrained by the desired qubit frequency.

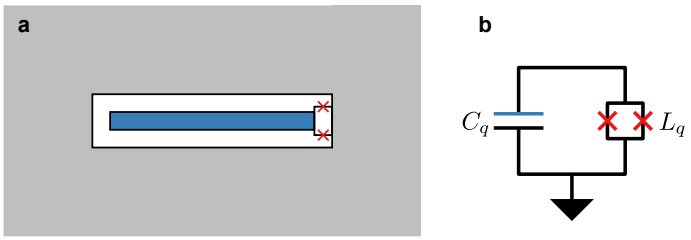

Figure 3.3: **Xmon transmon qubit. a,** Cartoon layout showing a basic design for an Xmon transmon qubit, a coplanar waveguide segment (blue) forming a capacitance to ground (gray) and a DC squid (red junctions). **b,** Circuit diagram.

We use planar transmon qubits based on the Xmon design [7, 85, 52, 17]. An Xmon is a "split transmon," where a DC squid plays the role of a tunable junction. One side of the DC squid is grounded, and the other connects to one plate of a low-loss capacitor made of a segment of coplanar waveguide (see Fig. 3.3). The circuit, then, is a capacitance $C_q \approx 100\,\mathrm{fF}$ and a DC squid inductance $L_q \approx 10\,\mathrm{nH}$ in parallel to ground. This corresponds to a frequency $\omega_{ge}/2\pi \approx 5.0\,\mathrm{GHz}$, anharmonicity $\eta/2\pi \approx -190\,\mathrm{MHz}$, and a characteristic impedance $Z_0^q = \sqrt{L_q/C_q} \approx 300\,\Omega$.

3.2 Control and readout

Two critical capabilities are manipulating and measuring the qubit state. We use well-established methods, primarily drawing from Refs. [85, 52, 18]. An optical micrograph of the particular qubit we use is shown in Fig. 3.4.

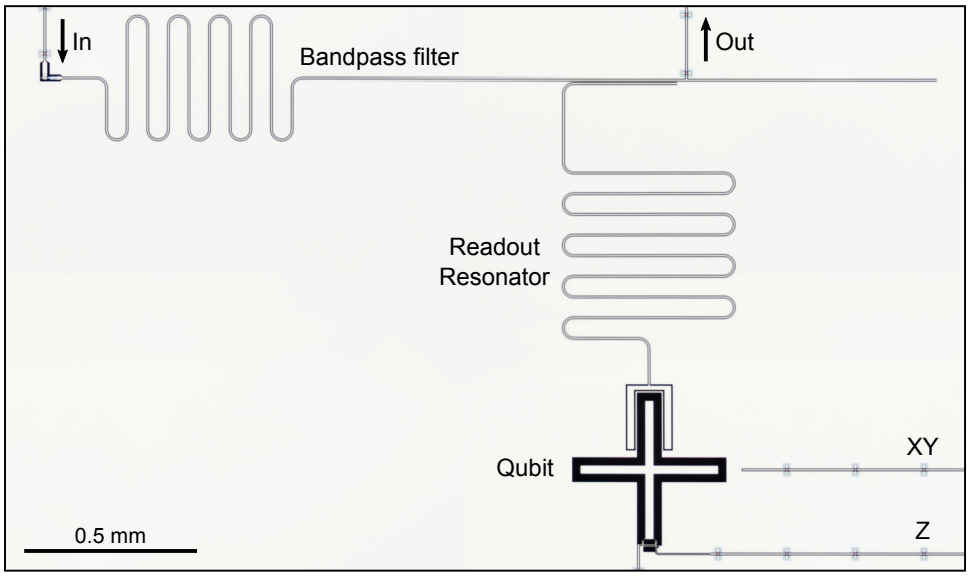

Figure 3.4: **Qubit circuit: readout and control.** Optical micrograph showing the essential readout and control elements of our qubit circuit. Top: Bandpass filter, made of a coplanar waveguide. Upper left: Input line for readout pulses, capacitively coupled to bandpass filter. Upper right: Output line for readout pulses, galvanically coupled to bandpass filter with low $Q_F \approx 20$. Center: Meandering readout resonator. Bottom: Qubit with labeled control lines, XY and Z. The line exiting the bottom of the image goes through the tunable coupler network to ground (not pictured).

3.2.1 Control

We have two control lines for the qubit, the XY line for resonant driving and the Z line for controlling the qubit frequency.

XY line

The XY line is configured to deliver microwave pulses up to around 5 GHz. These pulses, when resonant with the qubit frequency $\omega_{ge}/2\pi$, drive transitions between the $|g\rangle$ and $|e\rangle$ states. The line itself is a coplanar waveguide that ends in an open circuit near the qubit capacitor. This brings about a small capacitance C_{XY}. There is a balance between achieving strong enough coupling to quickly drive the qubit (reasonable pulse times are around 20 ns) without exposing the qubit to appreciable noise or loss.[5] The loss the qubit experiences through this capacitance can be summarized by a coupling quality factor [85]

$$Q_c = \left(\frac{C_q}{C_{XY}}\right)^2 \frac{Z_0^q}{Z_0^{\mathrm{TL}}}, \tag{3.19}$$

where $Z_0^{\mathrm{TL}} = 50\,\Omega$ is the coplanar waveguide (transmission line) characteristic impedance. We estimate the pictured $C_{XY} \approx 30$ aF, corresponding to $Q_c \sim 10^8$.

By finely controlling the amplitude, phase, frequency, and shape of the pulses, we can achieve arbitrary unitary transformations on the qubit state with microwave pulses. Another matter to keep in mind is the presence of the $|f\rangle$ state; we are careful to avoid exciting transitions between $|e\rangle$ and $|f\rangle$ and account for the effect of $|f\rangle$ on the desired transitions between $|g\rangle$ and $|e\rangle$ [19].

[5] Crosstalk is also a concern in systems with multiple qubits.

Z line

The Z line is a lower-frequency line delivering signals from DC up to around 200 MHz. The line is a coplanar waveguide that ends in a short to ground in the proximity of the qubit DC squid. Current flowing through the line brings about a magnetic flux bias Φ_{ext} through the DC squid, tuning its effective critical current. This allows us to control the qubit frequency $\omega_{ge}/2\pi$. It is crucial that these signals be low-noise; any noise in the current transfers directly to noise in the qubit frequency, which manifests itself as dephasing. We use a separate DC line, setting the "idle" flux bias for an entire pulse sequence, combined with arbitrary ≈200 MHz waveforms using a bias tee (see appendix D for details). We also must take care to achieve enough mutual inductance to the DC squid (∼1 pH gives $1\,\Phi_0$ of range from ±1 mA of current in the Z line) while not exposing the qubit to loss through the transmission line.[6]

These is also a similarly-configured control line for the tunable coupler, G, which is discussed below.

3.2.2 Readout

Qubit measurement is a difficult problem; we ordinarily want the qubit to be isolated from the environment, but occasionally we need to extract enough information from it to perform a projective quantum measurement. The method we employ is discussed in

[6]Ideally, the qubit itself would not couple to this bias line, but in practice there is inevitably some stray mutual coupling. With careful design, this can be much less than the ∼1 pH mutual inductance to the squid loop [52, 78]. There is a distinction between the DC current circulating in the squid loop and the microwave-frequency qubit current passing through the junctions in parallel.

great detail in Ref. [85]; here we provide a brief overview.

Dispersively coupled readout resonator

Earlier, we described the dispersive limit of the Jaynes-Cummings Hamiltonian. To perform readout, we dispersively couple the qubit to a dedicated readout resonator, which is in turn strongly coupled to a measurement transmission line. The idea is rooted in Eqn. 3.6, where the resonator frequency depends on the state of the qubit. Put another way, the qubit impedance loads the readout resonator, and due to the qubit's nonlinearity, the qubit impedance depends on whether it is in $|g\rangle$ or $|e\rangle$. We can readily measure the resonator frequency with a microwave transmission experiment. We measure the microwave transmission S_{21} at one frequency, near $\omega_r/2\pi$, and we observe a different value of S_{21} depending on the qubit state.

In this case, the readout resonator is a coplanar waveguide resonator, roughly 1 GHz above the qubit frequency with coupling $g/2\pi \approx 100\,\mathrm{MHz}$ brought about by a capacitor $C_r \approx 10\,\mathrm{fF}$. One important detail is that the expression for the dispersive shift shown above, $\chi = -g^2/\Delta$ (derived for a two-level qubit), needs to be corrected to take into account the transmon second excited state, $|f\rangle$ [54]:

$$\chi = -\frac{g^2}{\Delta}\frac{1}{1+\Delta/\eta}. \tag{3.20}$$

In addition to the dispersive shift χ, another important parameter is the rate κ_r at which energy leaves the readout resonator into the measurement transmission line. This

is also the rate at which the resonator may be excited by an external drive, so it has important implications for the duration of the measurement. It is beneficial to have the readout process take less than $\approx 1\,\mu s$.[7] The measurement duration will typically be a few times $1/\kappa_r$, suggesting $\kappa_r \sim 1/(100\,\text{ns})$ to $1/(10\,\text{ns})$. Optimal visibility (difference between $S_{21}^{|g\rangle}$ and $S_{21}^{|e\rangle}$) is obtained when $\chi = \kappa_r/2$. If χ is too small, the resonance dips overlap too much, and if χ is too large, the dips are so far apart that they aren't distinguished by measuring at the midpoint frequency.[8] An experimentally reasonable range for $\chi/2\pi$ is about 0.5 MHz to 5 MHz, which lines up well with the values for $1/\kappa_r$ mentioned above. However, there is a price to larger χ and κ_r: despite the large detuning Δ, the qubit can still lose energy through the transmission line; this is called "Purcell decay."

Bandpass filter

The main focus of Ref. [45, 85] is getting fast readout (large χ and κ_r) without burdening the qubit with appreciable loss. This is accomplished by using a second resonator in between the readout resonator and the transmission line. This second resonator is a bandpass filter: it facilitates the transfer of energy into the measurement transmission line near the readout frequency but suppresses it near the qubit frequency.

This is an added complication; it is possible to perform great experiments with a

[7] Longer readout times provide better signal to noise ratio, but taking too long is problematic because of energy decay in the qubit. It is also beneficial to have a fast measurement time, perhaps $\approx 100\,\text{ns}$, for the repetitive measurements needed for error correction schemes.

[8] The latter problem is not too bad; the readout resonator can be probed at $\omega_r^{|g\rangle}$ or $\omega_r^{|e\rangle}$ instead. It would just be faster to measure with larger κ_r.

similar readout resonator *without* a bandpass filter [8, 67, 82]. In our experiment, it was not obvious whether we would have long qubit lifetime T_1 in the presence of our mechanical resonator, so we included the filter to make the readout faster. As in Ref. [85], we use a quarter-wave coplanar waveguide with weak capacitive coupling to an input line ($Q_{\text{in}} \approx 1000$) and strong galvanic coupling to an output line ($Q_F \approx 20$). As in Ref. [51, 52], we use inductive coupling between the readout resonator and filter (see chapter 4 for a related discussion). The filter enhances κ_r by a factor of roughly Q_F while keeping the qubit safe from Purcell decay. It presents stronger coupling to the output transmission line at its resonance frequency (close to the readout resonator frequency) but suppressed coupling to the output at the qubit frequency.

3.3 Coupling

Our goal is to couple our qubit to a mechanical resonator. In chapter 2, we discuss some considerations from the perspective of a surface acoustic wave resonator. Here, we touch on a few common ways of coupling qubits and resonators. For a more detailed account, especially about the tunable inductive coupling scheme we use, see Ref. [68].

3.3.1 Capacitive coupling

One natural way of coupling circuits is with capacitors. Simply placing two transmons in proximity will engender a usable coupling capacitance C_c between them; see Fig. 3.5a.

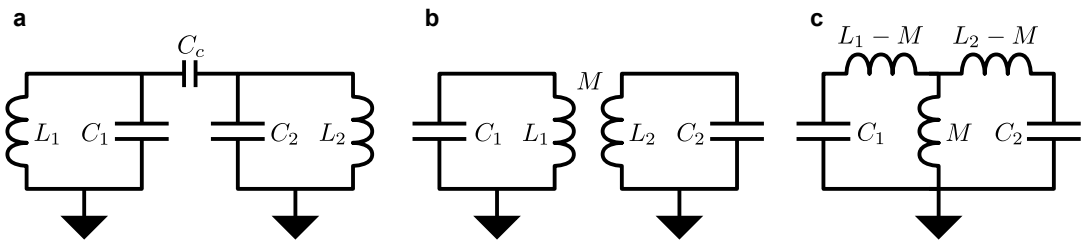

Figure 3.5: **Simple coupling circuits. a,** Circuit diagram of two LC resonators with coupling capacitance C_c. **b,** Circuit diagram of two LC resonators with mutual inductance M. **c,** Circuit diagram of two LC resonators coupled through a shared inductor M.

The coupling g for the circuit in Fig. 3.5a is

$$g = \frac{1}{2}\frac{C_c}{\sqrt{(C_1 + C_c)(C_2 + C_c)}}\sqrt{\omega_1\omega_2}. \tag{3.21}$$

Capacitive coupling involves one element driving a voltage across another; it is most natural when considering parallel resonances (impedance maxima). For fixed ω_i ($i = 1, 2$) and C_c, g is larger for smaller C_i (that is, larger $Z_i = \sqrt{L_i/C_i}$). As discussed above, we use capacitive coupling between our qubit and readout resonator.

3.3.2 Inductive coupling

Another way is with inductors. We discuss this in detail in chapter 4 in the context of coupling a resonator to a transmission line. One implementation uses mutual inductance M: two inductors in proximity, where current I through one brings about magnetic flux $\Phi = MI$ through the other. Another implementation is using a small shared inductance through which both devices pass current; then the coupling comes about from the small voltages induced across the shared inductor. These are shown in Fig. 3.5b-c. In both

cases, the coupling g is

$$g = \frac{1}{2}\frac{M}{\sqrt{L_1 L_2}}\sqrt{\omega_1 \omega_2}. \tag{3.22}$$

Inductive coupling involves one element driving current through another; it is most natural when considering series resonances (admittance maxima). For fixed ω_i and M, g is larger for smaller L_i (that is, smaller $Z_i = \sqrt{L_i/C_i}$). Inductive coupling is favorable for coupling to our mechanical resonator, both from the surface acoustic wave device perspective (see chapter 2) and from a hybrid integration perspective (see chapter 4). We use both implementations of inductive coupling in our tunable coupler circuit, which we discuss next.

3.3.3 Tunable inductive coupling

We can make things a bit more complicated by demanding that we be able to tune the coupling, to turn it on and off at will. This is very useful in experiments, and we will use it extensively in chapter 5 to control the interactions between our qubit and mechanical resonator. In the context of Josephson circuits, tunable inductive coupling is a natural choice. As discussed above, we can use Josephson junctions and superconducting loops in various configurations to create inductances that are controlled by external magnetic flux biases.

We use the gmon architecture [17, 35, 67, 82, 68], which is based on the Xmon transmon discussed above. There are two essential ingredients beyond the transmon itself. First, instead of directly grounding the qubit's DC squid, we ground it through a

small linear inductor L_g.[9] Second, we use that linear inductor to couple the qubit to an RF squid. The RF squid mediates the interaction between the various devices coupled to it. We control an external flux bias Φ_{ext} through the RF squid, allowing us to tune the effective inductance L_j of its junction. We operate in a regime where the nonlinearity of the coupler junction is not important, but it can be [35, 50].

To make the discussion concrete, we focus on the specific circuit that we use, shown in Fig. 3.6. This will be discussed further in chapter 5, in the context of coupling to a mechanical resonator. The coupler circuit is a segment of coplanar waveguide, shorted to ground on each side. The coplanar waveguide center trace is interrupted by a single Josephson junction, constituting an RF squid (including the current return path in the ground plane). We generate an external flux bias Φ_{ext} using a shorted control line, G, similar to the Z line discussed earlier for biasing the qubit DC squid.

The left branch, L_{g1}, is galvanically attached to the qubit DC squid and the coupler RF squid. This shared inductance to ground allows the qubit and coupler to interact. The right branch, L_{g2}, will be coupled with mutual inductance to a mechanical resonator; that is the subject of chapter 5. For the moment, the important point is that the qubit and resonator will be coupled if qubit current flows through L_{g2}. We control the path of the qubit current using the coupler junction inductance L_j. Biasing the junction phase to $\delta = \pi/2$ makes L_j very large, so the qubit current goes to ground through only L_{g1}, and the coupling is turned off. The coupling is maximized for $\delta = \pi$, where $L_j = -L_{j0}$,

[9] It is important to keep L_g much smaller than the qubit DC squid inductance L_q. This maintains the transmon nonlinearity and puts the coupler circuit at a low-voltage node, minimizing dielectric loss.

in which case much of the qubit current goes to ground through L_{g2}, bringing about the desired coupling.

Remark about crossovers

As an aside, we remark that the aluminum crossovers connecting the ground plane patches are very important to the functionality of the coupler. In designing a circuit like this, it is necessary to pay close attention to the flow of currents, including in the ground plane. The ground plane is cut into several pieces by the various coplanar waveguides, and the crossovers serve to connect them back together. See appendix E for fabrication information.

3.4 Single-qubit calibration and experiments

In this section, we go over some basic qubit experiments conducted on the single-qubit device we have been discussing. This is the same device we use in chapter 5, though here the experiments don't involve the mechanical resonator. We follow methods discussed in Refs. [85, 18], including detuned DRAG microwave pulses and flux pulse shape corrections.

3.4.1 Readout

As discussed above, we perform qubit readout using a dispersively coupled readout resonator and bandpass filter. To begin, we show a broad transmission S_{21} measurement

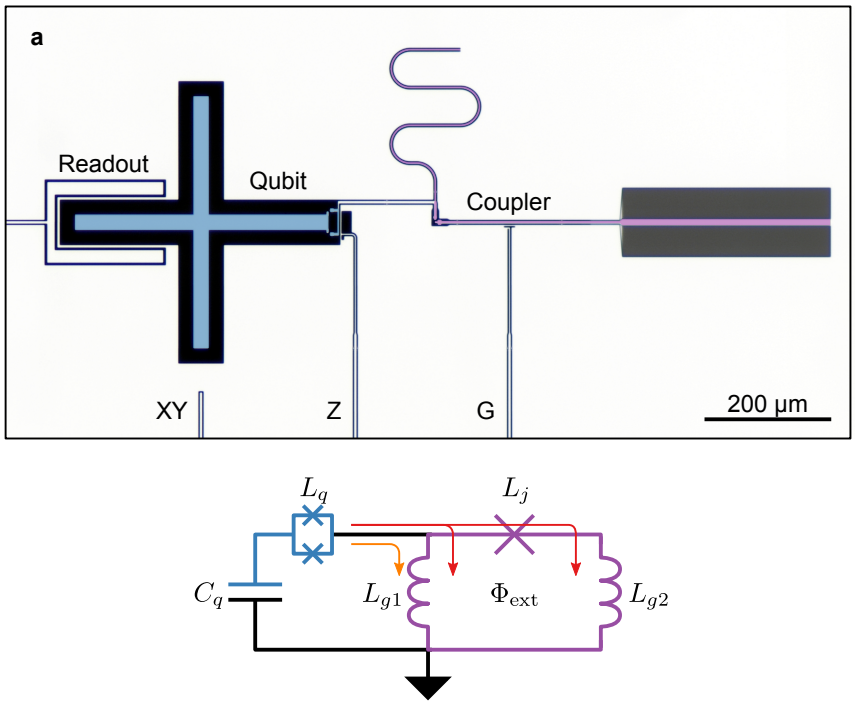

Figure 3.6: **Tunable inductive coupling circuit. a,** False-color optical micrograph of our qubit and tunable coupler network. The coupler flux bias is controlled by the G control line. Blue: Qubit. Purple: Coupler. Also see Fig. 3.4. Note this view is rotated and reflected with respect to Fig. 3.4; see chapter 5. **b,** Circuit diagram. We indicate the path of the qubit current with the coupling off (orange) or on (red).

through the readout circuit in Fig. 3.7a-b. We observe the broad (≈300 MHz) peak expected for the bandpass filter ($Q_F \approx 20$) with the narrow dip of the readout resonator centered on the filter. For subsequent measurements, we use custom electronics to measure the complex transmission amplitude $I + iQ$ (see appendix D).

We initially set up the readout frequency at the center of the dip with sufficiently low power to avoid saturating the qubit. This allows us to locate the qubit spectroscopically, where we scan the frequency f of a long (∼5 µs) microwave pulse on the qubit XY line while monitoring the readout transmission. When $f \approx \omega_{ge}/2\pi$, the qubit is partially excited, shifting the readout resonator frequency. We observe this as a peak in $|I + iQ|$, allowing us to determine ω_{ge}. Knowing ω_{ge}, we proceed with standard qubit experiments such as Rabi oscillations and tuning up XY microwave pulses for π and $\pi/2$ pulses.[10]

With a functional π pulse, we can prepare the qubit in $|g\rangle$ or $|e\rangle$. We measure the readout transmission as a function of frequency with the qubit prepared in $|g\rangle$ and $|e\rangle$ in Fig. 3.7c-d. The frequency offset between the resonances is $2\chi/2\pi$. As indicated in Eqn. 3.20, this depends on the qubit frequency $\omega_{ge} = \omega_r + \Delta$. Separately, as described in Ref. [85], we measure the readout resonator ringdown time $1/\kappa_r = 10$ ns. Given the accessible range of χ values, this κ_r is larger than optimal.

We optimize the readout by tuning the input power, pulse duration, pulse frequency, and qubit frequency during the readout sequence. We repeated prepare the qubit in $|g\rangle$ or $|e\rangle$ and then measure the demodulated amplitude $I + iQ$ of the readout pulse (see

[10] We also spectroscopically measure ω_{ef}, which is used in shaping the XY pulse envelopes. We optimize the XY pulses using the DRAG parameter α and a frequency offset [19].

appendix D). We observe adequate discrimination, a visibility of about 92%.[11] This could be improved with a smaller κ_r (decreasing the coupling between the readout resonator and bandpass filter) and a quantum-limited amplifier on the output [85].

3.4.2 Crosstalk

Crosstalk is the undesired side effects of signals in the control lines. Our circuit is relatively simple, just one qubit; the main crosstalk consideration is between the Z and G bias lines. Current I_Z in Z is meant to apply a flux bias Φ_Z to the qubit DC squid (controlling the qubit frequency), but it also causes some flux Φ_G to the coupler RF squid (controlling the coupling); the opposite is true of current I_G in G. This can be expressed in an inductance matrix, noting these are currents in the *bias lines*, not in the loops themselves. We also allow offsets Φ_i^0, the apparent flux through loop i with $I_Z = I_G = 0$:

$$\begin{bmatrix} \Phi_Z \\ \Phi_G \end{bmatrix} = \begin{bmatrix} M_{ZZ} & M_{ZG} \\ M_{GZ} & M_{GG} \end{bmatrix} \begin{bmatrix} I_Z \\ I_G \end{bmatrix} + \begin{bmatrix} \Phi_Z^0 \\ \Phi_G^0 \end{bmatrix}. \tag{3.23}$$

Determining $[M_{ij}]$ and $[\Phi_i^0]$ is very useful. The flux crosstalk in this design is substantial, and this calibration allows us to independently choose Φ_Z and Φ_G. We use this primarily for determining the DC biases mentioned above.

There are some complications in determining these crosstalk parameters. Measuring the qubit frequency is relatively easy, but measuring the coupling (here, the coupling to a mechanical resonator) is difficult; it would be better to do this calibration without involving the mechanical resonator. Also, as we discuss in more detail below, even in the

[11] When we attempt to prepare $|g\rangle$, we observe $P_e \approx 0.02$, and for $|e\rangle$, $P_e \approx 0.94$. This is also affected by the qubit thermal $|e\rangle$ population, which we measure to be about 1.7% in chapter 5.

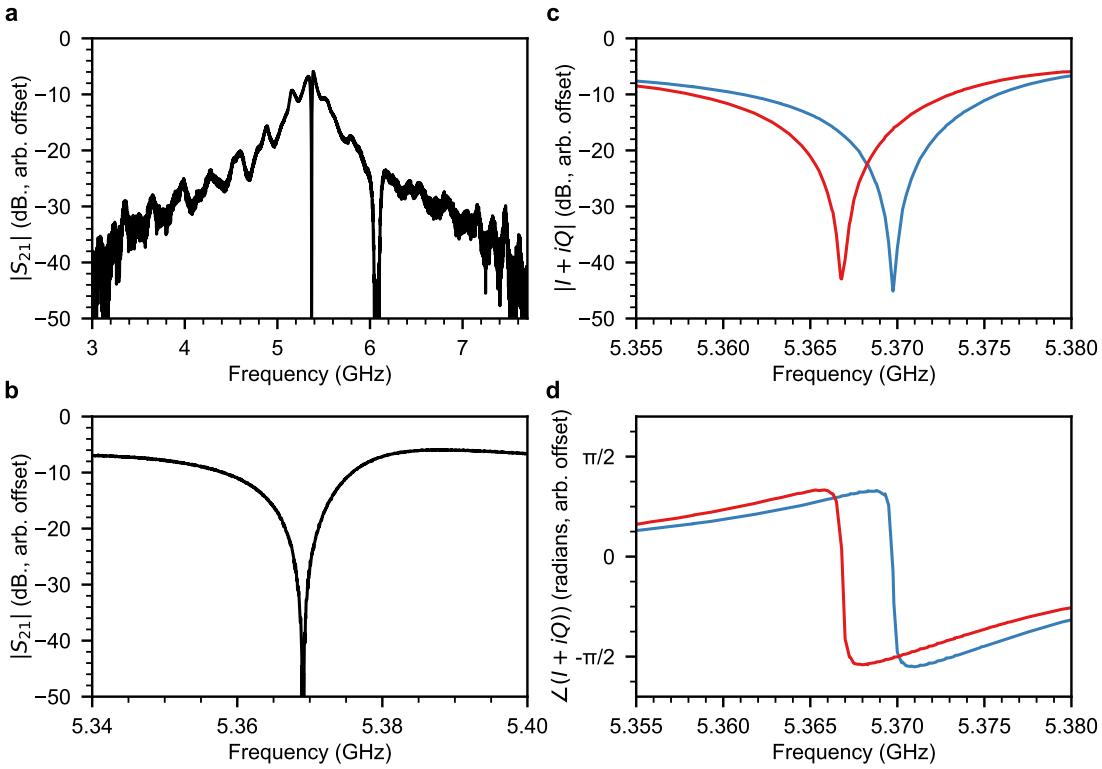

Figure 3.7: **Readout data. a,** Wide-frequency S_{21} measurement through the readout circuit showing the broad transmission peak of the filter and narrow dip of the readout resonator, measured with a vector network analyzer. The dip at 6.07 GHz is from a traveling wave parametric amplifier [60] (see appendix D). The overall level is arbitrary, dictated by the attenuation and amplification in the signal path. **b,** Zoomed-in scan near the readout resonator, as in **a**. **c-d,** Zoomed-in scan near the readout resonator, measured with qubit measurement electronics (see appendix D). Blue: Qubit prepared in $|g\rangle$. Red: Qubit prepared in $|e\rangle$. We measure the demodulated transmission amplitude $I + iQ$. We offset the magnitude to match **a-b** and subtract a line from the phase to account for signal delay. The frequency separation equals $2\chi/2\pi$, here about 3 MHz. Note χ depends on the detuning $\Delta = \omega_{ge} - \omega_r$.

absence of flux crosstalk, we still expect the coupler setting to influence the qubit frequency, as it changes the inductance the qubit sees to ground. Moreover, when changing DC biases, the qubit frequency also moves the readout resonator frequency, changing the optimal readout configuration.

We get around this by simply measuring the readout resonator instead. In our device, bias I_Z causes resonator frequency shifts of around 8 MHz, and I_G about 1 MHz. These shifts are periodic in the bias currents, as the squid flux responses are Φ_0-periodic. In the $\omega_r(\Phi_Z, \Phi_G)$ landscape, there is a convenient saddle point at $\Phi_Z = 0$ and $\Phi_G = \Phi_0/2$ repeated every $\Phi_0/2$ in Φ_Z and Φ_0 in Φ_G. We measure the readout transmission S_{21} at the saddle point frequency as a function of I_Z and I_G. This is shown in Fig. 3.8. The minima in transmission $|S_{21}|$ cross at the saddle points, allowing us to identify current points (I_Z, I_G) with flux values $\Phi_Z = n_z\Phi_0/2$ and $\Phi_G = (n_g + 1/2)\Phi_0$. From these points, we deduce $[M_{ij}]$ and $[\Phi_i^0]$ from Eqn. 3.23:

$$\begin{bmatrix} M_{ZZ} & M_{ZG} \\ M_{GZ} & M_{GG} \end{bmatrix} = \begin{bmatrix} 0.823 & 0.017 \\ 0.079 & 0.812 \end{bmatrix} \text{pH}; \quad \begin{bmatrix} \Phi_Z^0 \\ \Phi_G^0 \end{bmatrix} = \begin{bmatrix} -0.041 \\ 0.456 \end{bmatrix} \Phi_0. \tag{3.24}$$

There are also precise calibration techniques for measuring crosstalk from the arbitrary waveforms discussed above, using Ramsey interferometry [68]. In this device, the crosstalk is bad enough that those techniques failed; we use estimates from the DC-calibrated $[M_{ij}]$ when necessary. Future designs could improve this substantially. M_{GZ}, where current I_Z brings about flux Φ_G, is especially large, due to the large size of the coupler loop and its proximity to the Z line.

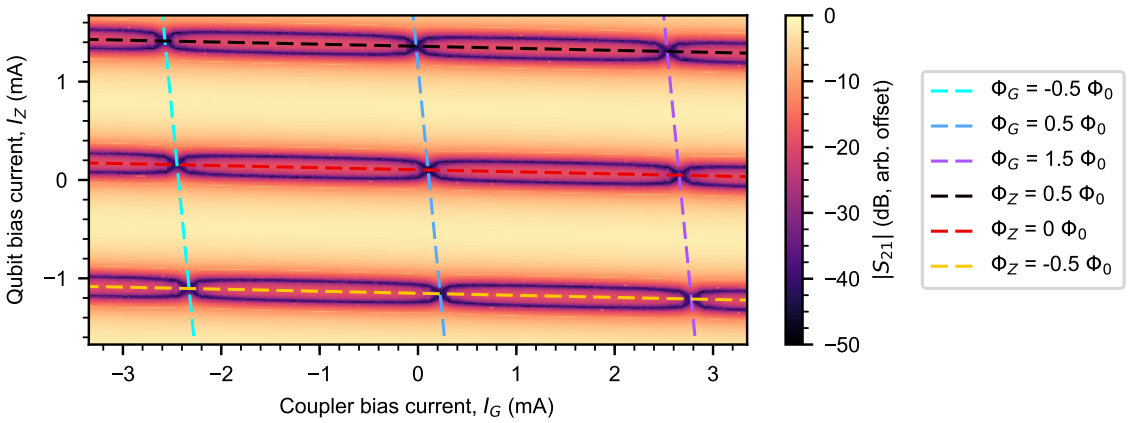

Figure 3.8: **Linear flux crosstalk.** Readout transmission magnitude $|S_{21}|$ (vector network analyzer, arbitrary offset) measured at the saddle point frequency versus bias currents I_Z and I_G. Overlaid: Linear constant-flux contours from Eqn. 3.23 with fitted parameters.

3.4.3 Linear circuit model

It is also useful to experimentally characterize the various circuit elements of the device. This allows us to validate the design and also will be used in chapter 5 together with the circuit model of the mechanical resonator discussed in chapter 2. We have several unknown parameters, primarily in the inductor network of the tunable coupler. In order to estimate those, we measure the qubit frequency $\omega_{ge}/2\pi$ as a function of coupler flux bias Φ_G, while we maintain $\Phi_Z = 0$. This is plotted in Fig. 3.9

We then fit this to the linear circuit model shown in Fig. 3.6. We incorporate the Φ_G dependence by assuming the coupler junction inductance follows $L_j = L_{j0}/\cos(\delta)$, where we calculate the junction phase δ from Φ_G and the inductances using Eqn 3.17. To

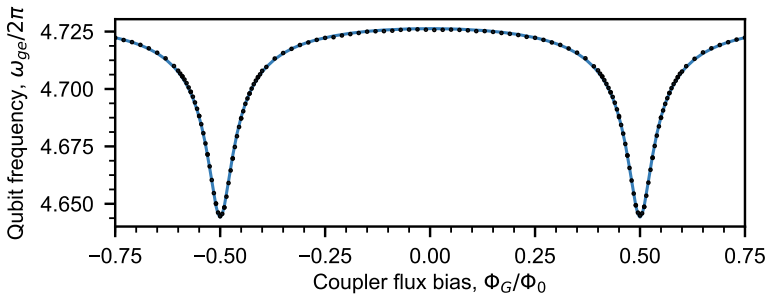

Figure 3.9: **Qubit frequency measurement.** Black points: Spectroscopically-determined qubit frequency $\omega_{ge}/2\pi$ as a function of coupler flux bias Φ_G. Blue line: Linear circuit model fit.

reduce the number of fit parameters, we fix $L_{j0} = 1.0\,\text{nH}$ based on room temperature and cryogenic DC measurements of test junctions. It would also be informative to measure $\omega_{ef}/2\pi$ in this scan; this helps constrain the qubit capacitance [68]. We arrive at the following parameters: $C_q = 110\,\text{fF}$, $L_q = 10.1\,\text{nH}$, $L_{g1} = 0.303\,\text{nH}$, and $L_{g2} = 0.403\,\text{nH}$. Note that the fitted L_{g2} includes all of the inductance to the right of the coupler junction in Fig. 3.6a. These are reasonably consistent with our design parameters.

3.4.4 Lifetime and coherence

Here, we present a few basic qubit measurements. This is the same device described in chapter 5, although in these measurements we do not interact with the mechanical resonator. In Fig. 3.10a-b, we measure the qubit energy lifetime T_1 from 3.5 GHz to 4.5 GHz. We observe a fairly consistent $T_1 \approx 20\,\mu\text{s}$. As we show in chapter 4, this is consistent with low-power internal quailty factor measurements of coplanar waveguide resonators with similar fabrication processes ($Q_i \approx 5 \times 10^5$).

We next consider dephasing. We perform these experiments at the qubit operation point used in chapter 5, where $\omega_{ge}/2\pi = 4.04\,\mathrm{GHz}$. Note the qubit frequency at the flux-insensitive point is 4.7 GHz. In Fig. 3.10c, we show the results of a Ramsey experiment. Although in chapter 5 we simply refer to a dephasing time $T_{2,\mathrm{Ramsey}}$, it is more precise to separate exponential decay ($T_{\phi,1}$, from white noise and energy relaxation) and Gaussian decay ($T_{\phi,2}$, from $1/f$ noise), using an envelope $\exp[-t/T_{\phi,1} - (t/T_{\phi,2})^2]$ [8]. Our fit suggests $T_{\phi,1} = (9 \pm 2)\,\mu\mathrm{s}$ and $T_{\phi,2} = (2.9 \pm 0.1)\,\mu\mathrm{s}$ (fit uncertainties). This lifetime and coherence time performance is consistent with previous experiments using similar qubit designs and fabrication techniques [8, 17, 51].

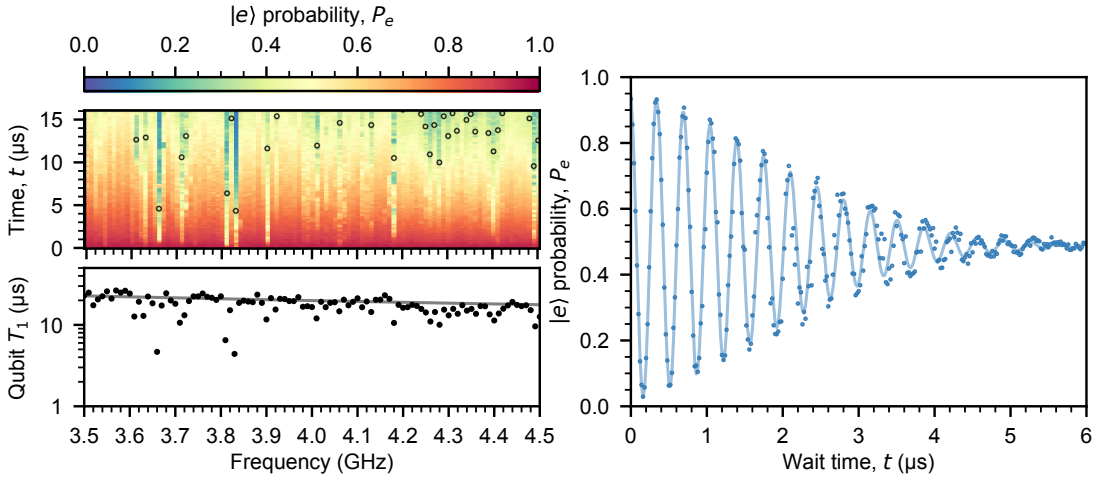

Figure 3.10: **Qubit lifetime and coherence times.** Upper left: Time-domain measurements of qubit lifetime T_1 over a wide range of qubit frequencies. The qubit is excited with a π pulse, and we bias the qubit to the desired frequency for a time t before measuring the qubit. The coupler flux Φ_G is set to minimize coupling the the surface acoustic wave device; see chapter 5. Black circles are fitted T_1 values. Many T_1 fits are $\approx$20 μs, above the plot range. Lower left: Fitted T_1 values. Line: Calculated $T_1 = Q/\omega$ for $Q = 5 \times 10^5$. Right: Ramsey experiment to determine $T_{\phi 1}$ and $T_{\phi 2}$. The qubit is excited with an $X_{\pi/2}$ pulse, we wait a time t, we perform a second $\pi/2$ pulse with relative phase $\phi = \omega_{\text{fringe}} t$, and we measure the qubit. Line: Fit to sinusoid with envelope $\exp[-t/T_{\phi,1} - (t/T_{\phi,2})^2]$.

Chapter 4

Flip-chip integration

So far, we have discussed SAW resonators and superconducting qubits in isolation. In this chapter, we explore a technique for combining two separate chips into a flip-chip assembly. This is a key enabling technology for the experiments in chapter 5.

4.1 Hybrid quantum systems

We have a glaring problem: we fabricate the SAW resonators on lithium niobate, due to its strong piezoelectricity, but it is doubtful a good superconducting qubit could survive on lithium niobate.[1] Instead, we prefer to fabricate the qubits on sapphire, which is chemically inert, low-loss, and robust—and for which we have an established, reliable fabrication procedure.

This is a common sort of problem when trying to bring disparate technologies to-

[1]Such a qubit would rapidly lose energy into bulk acoustic waves, and there would be substantial fabrication difficulties. This has been done, though the work is unpublished [2].

gether, including hybrid quantum systems [70, 90, 103, 87, 56, 20]. Different quantum systems have their own strengths and weaknesses. They also have their own materials constraints and fabrication issues. It would be useful to make separate devices for the different systems and then integrate those devices together.

4.2 Flip-chip integration

One approach to doing this is judiciously attaching two separate chips face to face: flip-chip integration. This is an established technology developed for semiconductor integrated circuits decades ago [57].

4.2.1 Metal bump bonding

In the context of integrated circuits, the main goal is to create many galvanic contacts between the two chips. This is accomplished with a soft metal "bump bonds," frequently made of indium. Indium is popular for cryogenic infrared sensors, as it has favorable low-temperature properties [74].

More recently, flip-chip technology has gained attention in the superconducting qubits community [81, 33]. As experiments scale from tens to hundreds of qubits in 2-dimensional arrays, it becomes difficult to route the necessary control wiring to each qubit. One solution is to use a flip-chip assembly with signals transferring between the two chips, allowing some separation between the control wiring and the qubits themselves. Indium is a natural choice, being well-established for cold flip-chip assemblies, and indium is

a superconductor ($T_c = 3.4\,\mathrm{K}$). The fabrication is somewhat involved, requiring layers under the indium to prevent diffusion and surface treatments to avoid oxidation. It is also necessary to have indium on both chips.

4.2.2 Epoxy spacers and glue

We use an alternative technique that is much simpler and more accessible, with the added benefit that it is easy to undo so that chips can be reused. The price we pay is abandoning galvanic connections between the chips. This is a technique for small-scale experiments in hybrid quantum systems, not for building a quantum computer.

The idea is to use photolithography to pattern epoxy spacers on one chip. The thickness of the spacers will determine the distance between the chips; about 1 µm to 100 µm is accessible, depending on the application. We then manually apply a small amount of photoresist (acting as glue) to the periphery of one chip. Next, we place the chips in a standard contact mask aligner, meant for photolithography, and use that to align the chips and bring them together. This is easiest with at least one visibly-transparent substrate.

This involves just one lithographic process beyond what is needed to fabricate the individual chips, and no specialized equipment or materials are needed. We use photoresist as glue; since it dissolves easily in acetone, we are able to cleanly separate and reuse chips that have been bonded together.

4.3 Test experiment: coplanar waveguide resonators

Superconducting circuits are very sensitive to material loss [69, 64, 77, 97], and the photoresist involved in this procedure could be problematic for qubit performance. We test this with a simple experiment where we embed superconducting coplanar waveguide resonators in a glued flip-chip assembly. Testing these sorts of resonators is a good proxy for qubit measurements [98, 28]. We use a standard "hanger" measurement configuration where we measure the transmission coefficient S_{21} through a transmission line that is coupled to a coplanar waveguide resonator—but the resonator and transmission line are on separate chips.

4.3.1 Coupling method

As we have mentioned, there will be no galvanic connection between the chips, so the chips will communicate through electromagnetic fields. There are two natural choices, capacitive coupling (electric fields) and inductive coupling (magnetic fields).

Capacitive coupling

Capacitive coupling is easy to see: simply make a parallel-plate capacitor using a large electrode on each chip. The resultant capacitance is approximately $\epsilon_0 A/d$ for overlap area A and chip separation d. It is easy to design such a capacitor to be unaffected by substantial lateral misalignment using a cross geometry, though it is clearly very sensitive to chip separation d. There's another problem. This capacitance alone is not enough to

drive a voltage across an impedance on the electrically-floating chip. It is necessary to involve another capacitance on the other side of the load, probably a large capacitance between the electrically-floating chip's "ground plane" and the actually-grounded ground plane of the other chip.

Inductive coupling

We adopt the alternative, mutual inductive coupling M. We have an inductor L on each chip, and current I through one inductor brings about magnetic flux $\Phi = MI$ through the other inductor. This integrates well with our goals of coupling to a series resonance (admittance maximum—see chapter 2) with tunable coupling (see chapter 3). Inductive coupling naturally works without galvanic connections, without the need to drive voltage between the ground planes.

Before looking at the details of the implementation, we first consider inductive coupling in general, with more depth than the discussion in chapter 2. The simplest circuit is depicted in Fig. 4.1a. Note the sign convention on the currents I_i, both going into the network: this is the convention for an impedance matrix Z, different from an $ABCD$ matrix [75]. The voltages and currents are related by

$$\begin{bmatrix} V_1 \\ V_2 \end{bmatrix} = \begin{bmatrix} L_1 & M \\ M & L_2 \end{bmatrix} \begin{bmatrix} dI_1/dt \\ dI_2/dt \end{bmatrix} = i\omega \begin{bmatrix} L_1 & M \\ M & L_2 \end{bmatrix} \begin{bmatrix} I_1 \\ I_2 \end{bmatrix} = Z \begin{bmatrix} I_1 \\ I_2 \end{bmatrix}, \tag{4.1}$$

where we identify the impedance matrix Z. This circuit is equivalent to the one shown in Fig. 4.1b, with an important distinction: Eqn. 4.1 still holds for the circuit in Fig. 4.1a even if the ground wires are not connected. We use this equivalence in the tunable

coupling circuit (see chapter 2 and chapter 5): a shared inductance to ground is like having a mutual inductance.

4.3.2 Hanger network calculations

In this coplanar waveguide resonator experiment, we wish to use the "hanger" configuration mentioned above. The relevant circuit is shown in Fig. 4.1d, where the currents I_i have the convention of the $ABCD$ matrix, which we will calculate shortly. This will allow us to analyze the device in greater detail later. To aid in keeping all the signs correct, also refer to Fig. 4.1c, which is just Fig. 4.1a rearranged to look like the "hanger" geometry.

$ABCD$ matrix

The $ABCD$ matrix also relates the voltages and currents at each port, in the following way [75]:

$$\begin{bmatrix} V_1 \\ I_1 \end{bmatrix} = \begin{bmatrix} A & B \\ C & D \end{bmatrix} \begin{bmatrix} V_2 \\ I_2 \end{bmatrix}. \tag{4.2}$$

This is useful for cascading 2-port networks using matrix multiplication, but here, we just use it because it is convenient for this particular calculation. Note that, unlike with the scattering matrix S, we consider the total voltages V_i and I_i, not incoming and outgoing amplitudes.

Now we solve for the $ABCD$ matrix of the network in Fig. 4.1d. Immediately, $I_1 = I_2$ because the current in that line has nowhere else to go; this means $C = 0$ and $D = 1$.

Considering the impedance Z and then the inductance L_c, we have

$$V_3 = -I_3 Z \tag{4.3}$$

$$V_3 = i\omega L_c I_3 + i\omega M I_2. \tag{4.4}$$

This allows us to eliminate I_3:

$$I_3 = -\frac{i\omega M}{i\omega L_c + Z} I_2. \tag{4.5}$$

Considering the voltage across the inductance L_f,

$$V_1 - V_2 = i\omega L_f I_2 + i\omega M I_3 \tag{4.6}$$

$$= \left(i\omega L_f + \frac{\omega^2 M^2}{i\omega L_c + Z} \right) I_2, \tag{4.7}$$

at which point we have the whole $ABCD$ matrix. We now take $L_f \to 0$ so that we get the desired identity matrix when $M \to 0$.[2] We also define $Z_r = i\omega L_c + Z$, incorporating the coupling inductor back into what will be our hanging resonator. With that, we have the full $ABCD$ matrix: $A = D = 1$, $C = 0$, and

$$B = \frac{\omega^2 M^2}{Z_r}. \tag{4.8}$$

This has a simple equivalent circuit, solely a series impedance B, depicted in Fig. 4.1e.

[2]This is essentially "absorbing" L_f back into the feed transmission line, which is quite appropriate if we have not changed the transmission line geometry, which will mostly be the case. We will also take into account small impedance mismatches (such as a bit of extra inductance) below.

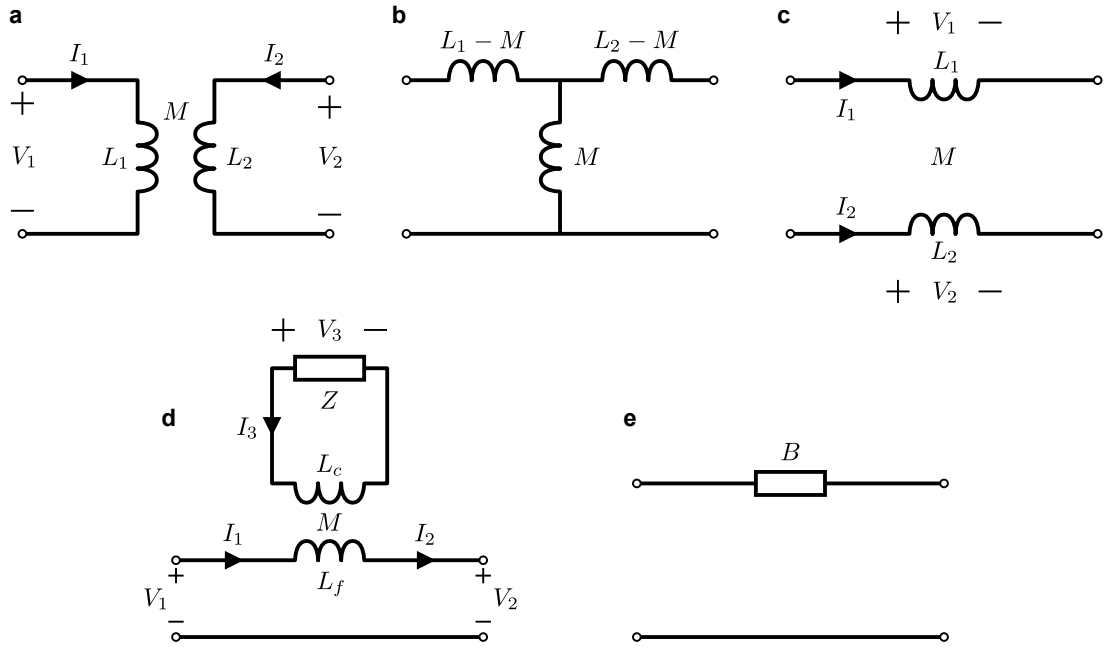

Figure 4.1: **Circuits for inductive coupling. a,** Simple circuit model of a two-port microwave network consisting of two inductors, L_1 and L_2, with mutual inductance M. The currents I_i and voltages V_i are configured as in an impedance matrix Z. **b,** Equivalent "tee" network to the circuit in **a**. **c,** The same circuit in **a** deformed to bring us closer to the "hanger" circuit model employed in this coplanar waveguide resonator experiment. **d,** "Hanger" circuit model, drawn for calculating the equivalent $ABCD$ matrix. The feed waveguide has inductance L_f with mutual inductance M to a coupling inductor L_c which is connected in series with an impedance Z. **e,** Equivalent circuit model for **d** determined with the $ABCD$ matrix.

Quarter-wave resonator

We use an open-circuit quarter-wave coplanar waveguide resonator [75], depicted in Fig. 4.2a. The transmission line has characteristic impedance Z_0^{TL}, effective relative permittivity ϵ_{eff}, and loss α.[3] This has a series resonance suitable for inductive coupling; a convenient lumped-element equivalent circuit shown is in Fig. 4.2b, valid near the resonance frequency $f_0 = \omega_0/2\pi$. In terms of the transmission line properties,

$$\ell = \frac{\pi c}{2\omega_0\sqrt{\epsilon_{\mathrm{eff}}}} \tag{4.9}$$

$$L = \frac{Z_0^{\mathrm{TL}}\pi}{4\omega_0} \tag{4.10}$$

$$C = \frac{1}{\omega_0^2 L} \tag{4.11}$$

$$R = Z_0^{\mathrm{TL}}\alpha\ell, \tag{4.12}$$

where c is the speed of light in vacuum, so the phase velocity in the transmission line is $v = c/\sqrt{\epsilon_{\mathrm{eff}}}$. Note that the characteristic impedance of this *resonance*, $Z_0^r = \sqrt{L/C} = \frac{\pi}{4}Z_0^{\mathrm{TL}}$, is different from the characteristic impedance of the underlying transmission line.

We connect this to the "hanger" geometry discussed earlier in Fig. 4.2c-d. In this configuration, the Z_r of Eqn. 4.8 is

$$Z_r = i\omega L + \frac{1}{i\omega C} + R. \tag{4.13}$$

In this experiment, the "coupling inductor" is actually a small length of transmission line

[3]The effective relative permittivity is related to the substrate relative permittivity. For a small coplanar waveguide on a substrate with relative permittivity ϵ_{sub}, $\epsilon_{\mathrm{eff}} = (1+\epsilon_{\mathrm{sub}})/2$. It is a bit more complicated in the flip-chip geometry.

near the shorted end of the resonator; we just incorporate it into the same equivalent lumped inductance L for the whole resonator.

Quality factors

It is very useful to characterize these resonators in terms of of quality factors. The internal quality factor Q_i is determined by loss in the resonator; in terms of the transmission line attenuation,

$$Q_i = \frac{\beta_0}{2\alpha} = \frac{\omega_0}{2\alpha v}, \tag{4.14}$$

where $\beta = \omega/v$ [75]. Near the quarter-wave resonance frequency ω_0, we consider β and α in terms of the fractional frequency shift $\Delta\omega/\omega_0 = \delta x$:

$$\beta\ell = \frac{\pi}{2}\frac{\omega}{\omega_0} = \frac{\pi}{2}(1+\delta x) \tag{4.15}$$

$$\alpha\ell = \frac{\beta_0\ell}{2Q_i} = \frac{\pi}{4Q_i}. \tag{4.16}$$

The coupling quality factor Q_c quantifies how energy leaves the resonator into the coupled transmission line. We calculate this using the lumped-element model in Fig. 4.2. We replace the measurement transmission line on each side with an impedance $Z_0^{\mathrm{TL}} = 50\,\Omega$ to ground. Current through the inductance L_f goes through both Z_0^{TL}'s in series, so they present a load $Z = 2Z_0^{\mathrm{TL}}$. Using Eqn. 4.1, we find an equivalent impedance Z_L of the inductance L with mutual coupling M to L_f and Z:

$$Z_L = i\omega L + \frac{\omega^2 M^2}{i\omega L_f + Z} \approx i\omega L + \frac{\omega^2 M^2}{Z}. \tag{4.17}$$

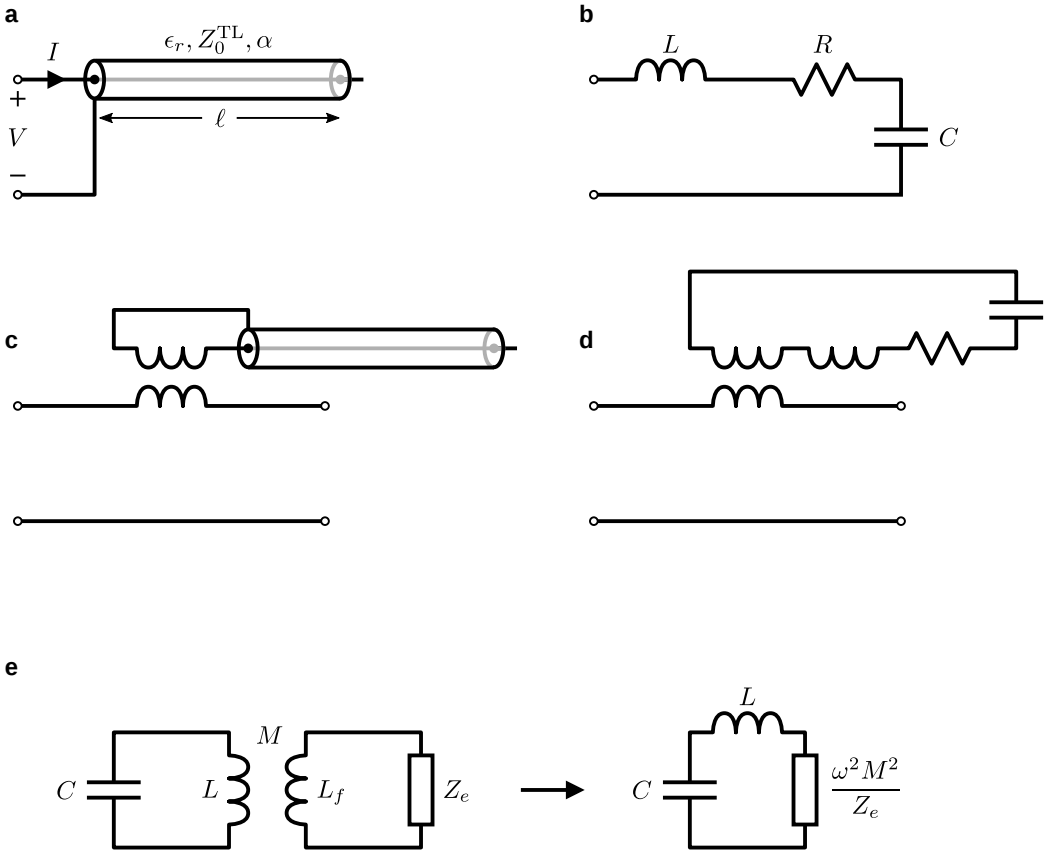

Figure 4.2: **Quarter-wave resonator. a,** One-port network, looking into an open-circuit quarter-wave resonator with length ℓ. **b,** Equivalent series RLC circuit for **a** near its resonance frequency. **c,** Open-circuit quarter-wave resonator inductively coupled to a transmission line in a "hanger" arrangement. The coupling inductor would actually be a small length of transmission line. **d,** "Hanger" arrangement with the equivalent circuit from **b**. **e,** Lumped-element model for calculating the coupling quality factor Q_c, made from **d** with no internal loss ($R = 0$) and the measurement transmission line replaced with a lumped-element impedance $Z_e = 2Z_0^{\mathrm{TL}}$.

This suggests an equivalent series RLC circuit for the resonator loaded by the transmission line, also shown in Fig. 4.2. The loading series resistance at resonance is $R_L = \frac{\omega_0^2 M^2}{2Z_0^{\mathrm{TL}}}$, giving a quality factor

$$Q_c = \frac{Z_0^r}{R_L} = \frac{\pi}{4} Z_0^{\mathrm{TL}} \frac{2Z_0^{\mathrm{TL}}}{\omega_0^2 M^2} = \frac{\pi}{2} \left(\frac{Z_0^{\mathrm{TL}}}{\omega_0 M} \right)^2 . \tag{4.18}$$

Transmission S_{21}

We calculate the transmission S_{21} through the measurement waveguide analogously to Refs. [63, 64], where they use capacitively-coupled, short-circuit quarter-wave resonators. The input impedance of an open-circuit transmission line segment of length ℓ is [75]

$$Z_r = Z_0^{\mathrm{TL}} \frac{1 + i \tan(\beta\ell) \tanh(\alpha\ell)}{\tanh(\alpha\ell) + i \tan(\beta\ell)}. \tag{4.19}$$

We apply Eqn. 4.15 and 4.16 and expansions of tan and tanh:

$$Z_r \approx \frac{4Q_i Z_0^{\mathrm{TL}}}{\pi} \frac{1 - i\frac{1}{2Q_i \delta x}}{1 - i\frac{8Q_i}{\pi^2 \delta x}} \tag{4.20}$$

$$= \frac{\pi Z_0^{\mathrm{TL}}}{4Q_i} \frac{1 + i2Q_i \delta x}{1 + i\frac{\pi^2 \delta x}{8Q_i}} \tag{4.21}$$

$$\approx \frac{\pi Z_0^{\mathrm{TL}}}{4Q_i} \left(1 + i2Q_i \delta x\right). \tag{4.22}$$

This goes into Eqn. 4.8, where we approximate $B \approx \omega_0^2 M^2/Z_r$.[4] Finally, we use the simple formula for $1/S_{21}$ transmitting through a series impedance B [75]:

$$\frac{1}{S_{21}} = 1 + \frac{B}{2Z_0^{\mathrm{TL}}} \tag{4.23}$$

$$\approx 1 + \frac{Q_i}{Q_c}\frac{1}{1 + i2Q_i\delta x}. \tag{4.24}$$

As in Ref. [64], we consider a small impedance mismatch ΔZ in series with B, where we assume ΔZ is approximately constant near ω_0. When performing the experiment, the overall level of $|S_{21}|$ is offset by attenuation and amplification; it will also be slightly offset due to ΔZ. When we normalize S_{21} to $\tilde{S}_{21}$ by assuming the transmission just off the resonance should give $|\tilde{S}_{21}| = 1$, this also involves ΔZ. It scales the second term in Eqn. 4.24 by a complex number near unity, $1 + \frac{\Delta Z}{2Z_0^{\mathrm{TL}}}$. We absorb the magnitude into a rescaled coupling quality factor Q_c^* and leave the phase in the form $e^{i\phi}$, as in Ref. [64], conveniently arriving at the same expression for the normalized inverse transmission,

$$\frac{1}{\tilde{S}_{21}} \approx 1 + \frac{Q_i}{Q_c^*}e^{i\phi}\frac{1}{1 + i2Q_i\delta x}. \tag{4.25}$$

Below, we use this function to fit the experimental data for Q_i and Q_c^* (which we will just refer to as Q_c).

[4] Expanding $\omega^2 = \omega_0^2(1 + 2\delta x + (\delta x)^2)$, the terms in δx will be dominated by the $Q_i\delta x$ term in Eqn. 4.22.

Photon number

It is useful to know the steady-state energy in the resonator as a function of input power P. Suppose we are driving the measurement line with power P (voltage amplitude $V = \sqrt{2PZ_0^{\mathrm{TL}}}$) at the resonance frequency ω_0. We first calculate the current I_2 through the impedance B in Fig. 4.1e:

$$I_2 = \frac{S_{21}V}{Z_0^{\mathrm{TL}}} = \frac{Q_c}{Q_i + Q_c}\frac{V}{Z_0^{\mathrm{TL}}}. \tag{4.26}$$

Next, we convert this to the resonator current I_3, using Eqn. 4.5 with $Z_r = R$ at ω_0:

$$I_3 = -\frac{i\omega M}{Z_r}I_2 = -\frac{i\omega_0 M}{R}\frac{Q_c}{Q_i + Q_c}\frac{V}{Z_0^{\mathrm{TL}}}. \tag{4.27}$$

We now convert this to the total energy U stored in the resonator,

$$U = \frac{1}{2}L|I_3|^2 = \frac{1}{2}L\left(\frac{\omega_0 M}{R}\frac{Q_c}{Q_i + Q_c}\frac{V}{Z_0^{\mathrm{TL}}}\right)^2. \tag{4.28}$$

We substitute out L (using Eqn. 4.10), R (using $Q_i = \frac{\pi}{4}\frac{Z_0^{\mathrm{TL}}}{R}$), and $\omega_0 M$ (using Eqn. 4.18):

$$U = \frac{1}{2} \times \frac{\pi}{4}\frac{Z_0^{\mathrm{TL}}}{\omega_0} \times \frac{\pi}{2}\frac{(Z_0^{\mathrm{TL}})^2}{Q_c} \times \left(\frac{4}{\pi}\frac{Q_i}{Z_0^{\mathrm{TL}}}\right)^2 \times \left(\frac{Q_c}{Q_i + Q_c}\frac{V}{Z_0^{\mathrm{TL}}}\right)^2 \tag{4.29}$$

$$= \frac{2Q_c}{\omega_0}\left(\frac{Q_i}{Q_i + Q_c}\right)^2 P. \tag{4.30}$$

Finally, we convert this energy to an average photon number

$$n = \frac{U}{\hbar\omega_0} = \frac{2Q_c}{\omega_0}\left(\frac{Q_i}{Q_i + Q_c}\right)^2 \frac{P}{\hbar\omega_0}. \tag{4.31}$$

4.3.3 Implementation: simulations of mutual inductance

We use two coplanar waveguides (a simple, well-understood geometry), one on each chip, overlaid to achieve strong mutual inductance. This also makes the couplers gradiometric, insensitive to uniform magnetic flux. We study this coupling method using finite element simulation (Sonnet). The geometry is shown in Fig. 4.3, which we model as two inductors L with mutual inductance M (see Fig. 4.1). It consists of two matching, shorted coplanar waveguide segments on separate sapphire substrates, as in the flip-chip geometry.

We use the simulation to calculate the impedance matrix Z [75] of the two port network at 5 GHz. For this circuit, the impedance matrix has the form of Z in Eqn. 4.1 with $L_1 = L_2 = L$. We then calculate the mutual inductive coupling strength $M/L = Z_{21}/Z_{11}$.[5] We consider two coplanar waveguide sizes. In both cases, the center trace width $w = 20\,\mu\text{m}$. We use two different ground plane spacings s, $10\,\mu\text{m}$ (which gives a convenient characteristic impedance near $50\,\Omega$) and $40\,\mu\text{m}$ (which gives stronger mutual inductance in this geometry). We plot the simulated M/L for these two geometries as a function of the relative position of the two inductors. We simulate the effects of lateral misalignment Δy and inter-chip spacing d. The results are shown in Fig. 4.3. This geometry maintains good coupling even in the presence of several μm of misalignment in any direction. As a function of chip spacing d, M/L decreases much more slowly than $1/d$, which is the dependence a parallel plate capacitance would have.

The value $M/L \approx 0.5$ is also quite favorable for such a simple geometry. It is compa-

[5] There is actually a minor sign issue here. The Sonnet simulation geometry has one inductor "turned around" compared to the circuit model, so really $M/L = -Z_{21}/Z_{11}$ the way we want to define it.

rable to the mutual inductance attained in Ref. [67], where they interleave loops of narrow wires in the same plane using air bridge crossovers. For adjacent coplanar waveguides in the same plane, it is difficult to exceed $M/L \approx 0.1$.

4.3.4 Device details

We now turn to the actual experiment, eight coplanar waveguide resonators inductively coupled to a transmission line on a separate chip.

Design

The coupling geometry we describe above is very flexible. We can access several orders of magnitude of coupling quality factor Q_c, from around 10^2 to 10^6. We set out to demonstrate this by designing eight coplanar waveguide resonators. The resonators are all composed of coplanar waveguide with center trace width $w = 20\,\mu\text{m}$ and ground plane spacing $s = 10\,\mu\text{m}$, which gives a characteristic impedance $Z_0^{\text{TL}} \approx 50\,\Omega$ on sapphire. Each has a slightly different length (and hence frequency), so we can interrogate them individually.

The coupler designs for the resonators are listed in Table 4.1. All the couplers have center trace width $w = 20\,\mu\text{m}$, matching the rest of the resonator waveguide. Resonator 1 has a very aggressive coupler to push Q_c near 10^2, where we increase the ground plane spacing. As we go down the table, we adjust the coupler to be less aggressive (decreasing M, increasing Q_c). In resonators 5-8, we introduce an intentional offset Δy. This allows us to increase Q_c and also provides an experiment for how misalignment affects the

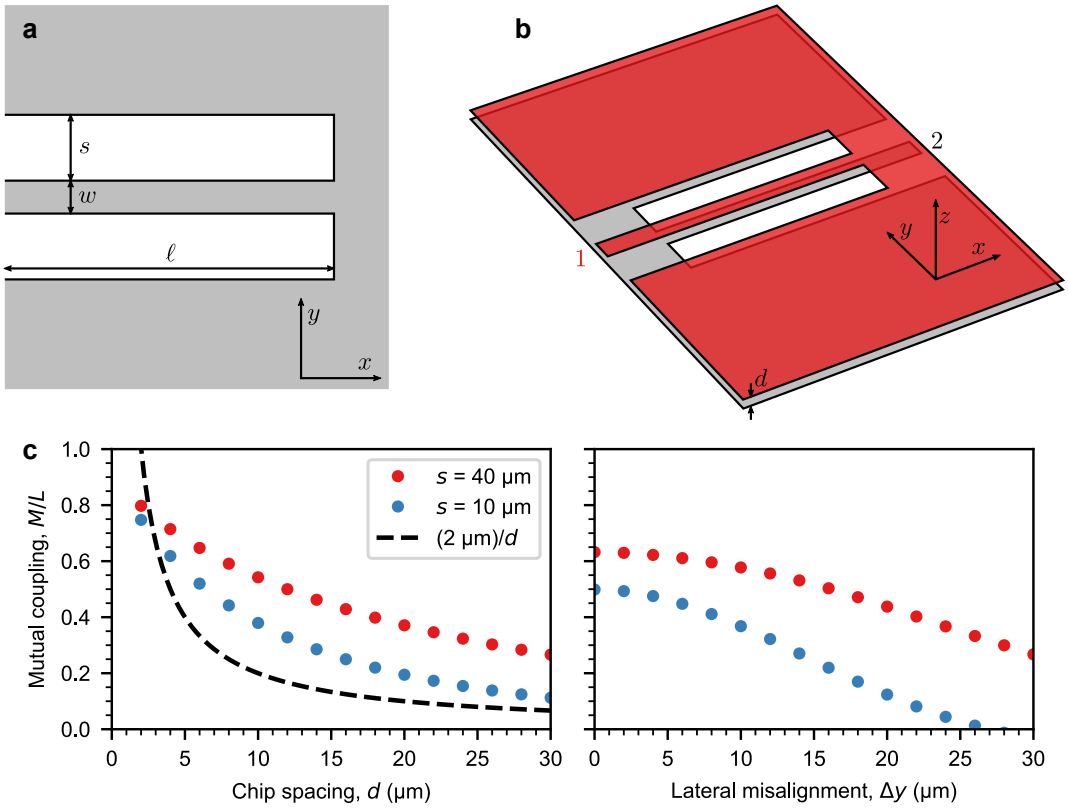

Figure 4.3: **Simulations of inductive coupling. a,** Top-view schematic of an inductor made of a shorted coplanar waveguide segment with center trace width w, ground plane space s, and length ℓ (gray is metal). **b,** Perspective-view schematic similar to our Sonnet simulation geometry. Two inductors (as in **a**) are overlaid on top of each other, facing opposite directions. The red inductor (with port 1), is suspended distance d above the blue inductor (with port 2). In the simulation, vacuum is between the red and blue layers, and sapphire is outside the two layers. **c,** Finite element simulations with a geometry like in **b** subject to various alignment conditions. We study two coplanar waveguide geometries, $s = 40\,\mu\text{m}$ and $10\,\mu\text{m}$, both with $w = 20\,\mu\text{m}$. Left: We vary the vertical spacing d between the chips. M/L decreases much more slowly than $\sim 1/d$. Right: We vary the lateral misalignment Δy between the chips, with $d = 6.5\,\mu\text{m}$ fixed. M/L is close to constant for $\Delta y < 5\,\mu\text{m}$ and falls off slowly after that. M/L actually changes sign for $s = 10\,\mu\text{m}$ at $\Delta y > 26\,\mu\text{m}$ because opposite spaces of the coplanar waveguide start to line up.

Resonator	Coupler space s_c (µm)	Coupler length ℓ_c	Offset Δy (µm)	Design Q_c
1	40	300	0	2.3×10^2
2	10	300	0	6.9×10^2
3	10	100	0	6.0×10^3
4	10	40	0	3.2×10^4
5	10	40	5	4.5×10^4
6	10	40	10	6.3×10^4
7	10	40	15	1.5×10^5
8	10	40	20	5.9×10^5

Table 4.1: Coupler design information for the eight coplanar waveguide resonators.

coupling, something we investigated in the simulations in Fig. 4.3.

Fabrication

We lay out the design with a coplanar waveguide crossing the center of the bottom chip (again $w = 20\,\mu\text{m}$ and $s = 10\,\mu\text{m}$). The eight resonators are laid out on the second, smaller chip in a 4×2 array, each with the appropriate coupler above the central waveguide. We include room for the epoxy and glue, which will be discussed below.

The primary fabrication process is depositing 100 nm aluminum on a clean, double side polished sapphire wafer and then etching a pattern (primarily the various coplanar waveguides) into the aluminum using photolithography and inductively coupled plasma etching. We then pattern SU-8 epoxy spacers on the periphery of each resonator chip using photolithography. These fabrication processes are detailed in appendix E. The spacers are about 6.5 µm thick, and once hard baked, they are quite robust, immune to solvents like acetone. We dice the sample into individual chips *after* defining the epoxy spacers. The completed chips are shown in Fig. 4.4. In this case, we fabricate both halves

of the assembly on the same wafer, but that is not necessary; we will demonstrate this by combining two different materials in chapter 5.

Flip-chip assembly details

We bond two chips together in a standard manual mask aligner (Karl Suss MJB4). We use the mask vacuum to suspend one chip (here, the larger 6 mm × 6 mm chip) upside down. A machined acrylic plate serves to transfer the vacuum from the metal mask holder to the chip. This chip remains fixed in place during the bonding procedure. It is important that this chip be double side polished and transparent (visible light is easiest, though in principle this could be done through silicon with an infrared camera).

The second chip has the resonators and the epoxy spacers. The epoxy pattern is also designed to "wall off" the region where we will apply glue to prevent it from spreading to the resonators. For the glue, we use nLOF 2070 photoresist, though surely other choices would work. It is a good viscosity for manual application, it fills the gap between the chips well, and it easily dissolves in acetone. We do observe that after two thermal cycles to mK temperatures, it becomes very brittle. We apply the glue manually using a splintered wooden handle from a cotton swab, watching under a binocular microscope while holding the chip with tweezers. We use about 10 nL of glue, covering roughly 2 mm along two opposite edges. This requires a bit of finesse.

We increase the "thickness setting" dial to lower the sample chuck all the way down. We then load the second chip onto the mask aligner's sample chuck and raise the contact lever to engage the sample vacuum, while keeping the sample about 1 mm below the

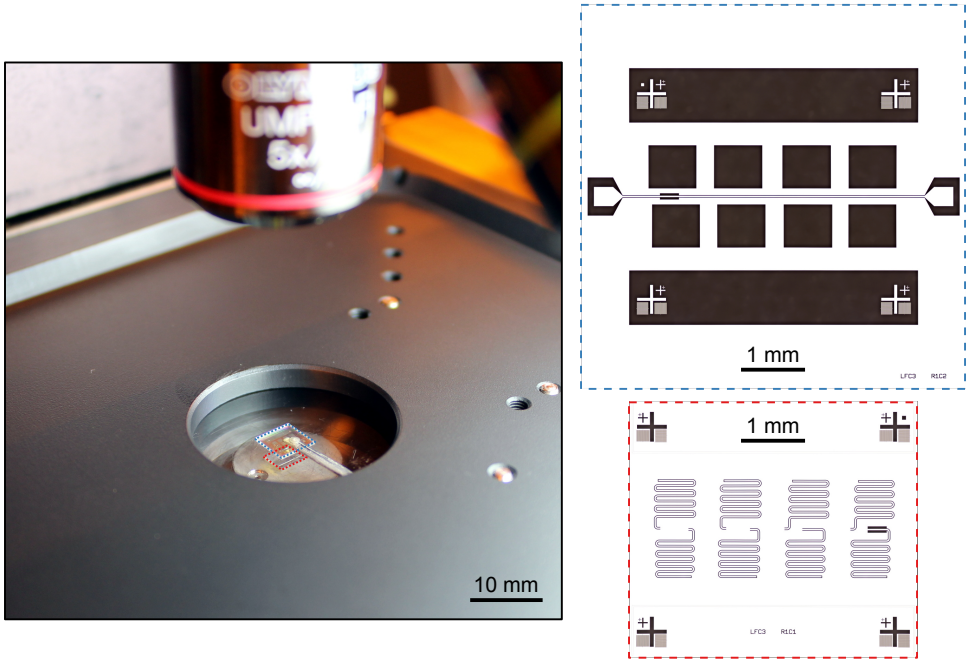

Figure 4.4: **Aligning chips in the manual mask aligner.** Left: Photograph of the flip-chip bonding process. The two chips (outlined in false color) are loaded in the mask aligner. We observe the chips through the microscope objective to carry out the alignment. Right: Composite optical micrographs of complete chips. Colored outlines correspond to the outlines on the left. Top: 6 mm × 6 mm bottom chip with measurement transmission line running from left to right, between two pads for wirebonds. Bottom: 4.5 mm × 4 mm top chip with eight coplanar waveguide resonators.

suspended chip. We then iteratively align the sample (translation and rotation) while raising it up to the suspended chip using the "thickness setting" dial. A photograph showing the chips in the aligner under a microscope objective is shown in Fig. 4.4. As the chips become close, the photoresist clearly contacts the suspended chip and starts to spread out. The chips are in good contact when attempting to raise the sample no longer spreads out the photoresist, and optical interference patterns become visible (due to the suspended chip being pushed against the acrylic plate).

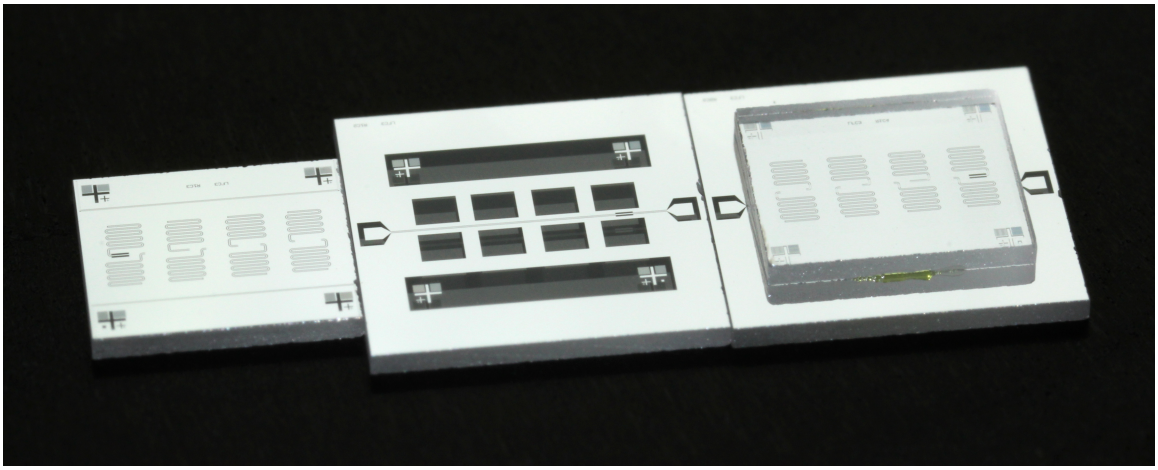

Figure 4.5: **Flip-chip assembly.** Photograph illustrating the flip-chip assembly (perspective view). Left: Smaller chip (4.5 mm × 4 mm) with eight coplanar waveguide resonators. Center: Larger chip (6 mm × 6 mm) with the measurement transmission line. Right: Completed assembly, the one we cool down and measure.

At this point, the flip-chip assembly is quite fragile; handling it can easily misalign the chips by ∼10 µm. It is necessary to cure the photoresist glue with a bake. We accomplish this safely by leaving the assembly clamped inside the mask aligner and heating the acrylic plate with a hot air gun (Aoyue 852). We estimate the chip temperature reaches about 60 °C from a hot air temperature of 100 °C. We heat the acrylic plate for 10 minutes and then let it cool for 10 minutes before removing the assembly; now it is safe to handle. We show a photograph of the completed assembly in Fig. 4.5.

In this process, we have a typical lateral misalignment of up to about 2 µm and rotation misalignment of up to about 0.5 mrad (0.03°). If the alignment is unsatisfactory, it is easy to separate the chips by soaking the assembly in acetone, and then bonding can be attempted again. We find that the inter-chip spacing is consistently less than 10 µm; spacing exceeding that is easily discerned in an optical microscope at high magnification.

In Fig. 4.6, we illustrate typical alignment and inter-chip spacing.

4.3.5 Experimental results

We wirebond the assembly shown in Fig. 4.5 and cool it down to 7 mK in a dilution refrigerator. We measure the microwave transmission through the device with a vector network analyzer (Agilent PNA-L). The input line is heavily attenuated and filtered, and the output line is amplified with a cryogenic amplifier (Low Noise Factory HEMT) and room temperature amplifiers (Miteq AFS3). See appendix D for details.

We first measure over a broad frequency range, shown in Fig. 4.7. We observe the eight desired resonances near 6 GHz as designed. The resonators with aggressive coupling (the deepest dips) are at higher frequencies than expected, likely from an error accounting for the inductance of the couplers or the loading from the transmission line. Fortunately, each resonance is still individually resolvable. There is also an unwanted resonance of unknown origin at 4.5 GHz. We measure its $Q_i \approx 6 \times 10^4$ and $Q_c \approx 5 \times 10^4$. It may be a slotline mode in the transmission line, a parallel-plate mode between the chips, a circulating mode around the perimeter of the floating chip, or something else.

We next zoom in on each of the eight resonances and measure them at high power. These results are shown for three representative resonators in Fig. 4.8. These measurements all have the same input power, so the photon number varies substantially for each resonator depending on its Q_c, and this also impacts the Q_i. We summarize the fitted Q_c values in Table 4.2 and Fig. 4.9. We achieve the desired range, reasonably consistent

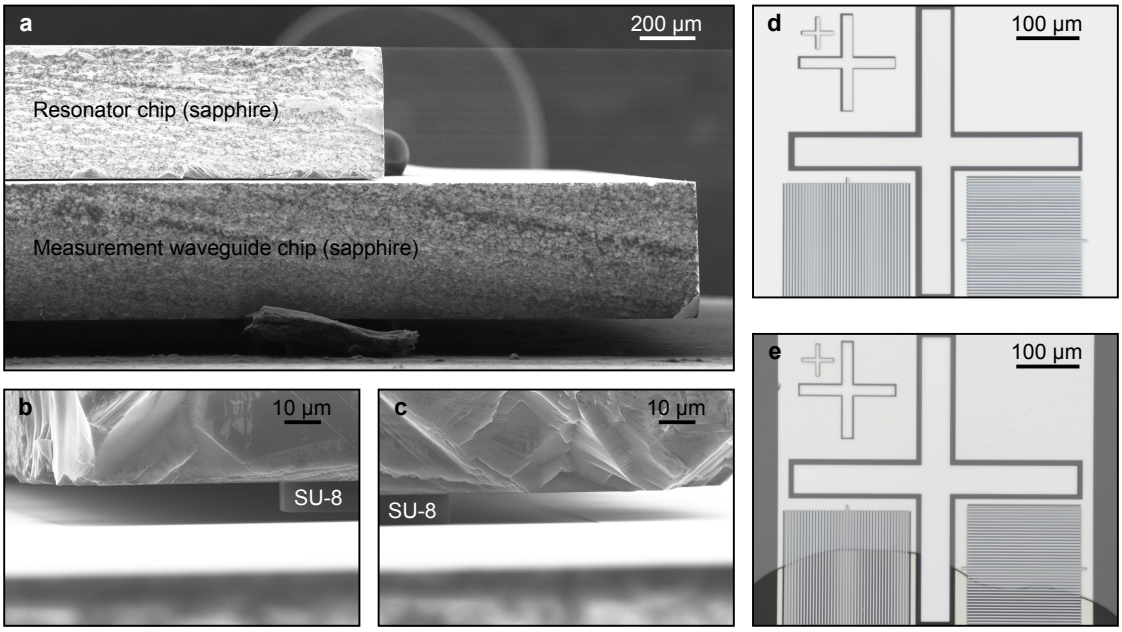

Figure 4.6: **Flip-chip alignment. a-c,** Scanning electron micrographs near grazing incidence showing a completed assembly. Based on optical microscopy, this is a typical sample. **b-c,** Zooming in near the corners of the resonator chip to see the SU-8 epoxy (labeled) and spacing between the chip. In **b**, there is a gap of about 2.1 µm (total space 8.3 µm). In **c**, there is no discernable gap (total space 6.2 µm). This different suggests a tilt of about 0.5 mrad. **d-e,** Representative alignment marks of completed assemblies, viewed through the back of the 6 mm sapphire chip with an optical microscope. **d,** The coplanar waveguide resonator device cooled down and measured in this chapter. Alignment error is about 2 µm. **e,** The surface acoustic wave and qubit device used in chapter 5. Alignment error is less than 0.5 µm. The arrays of lines at the bottom of **d** and **e** are Vernier scales with 0.25 µm graduation difference. Typical planar rotation error (not pictured) is less than 0.5 mrad.

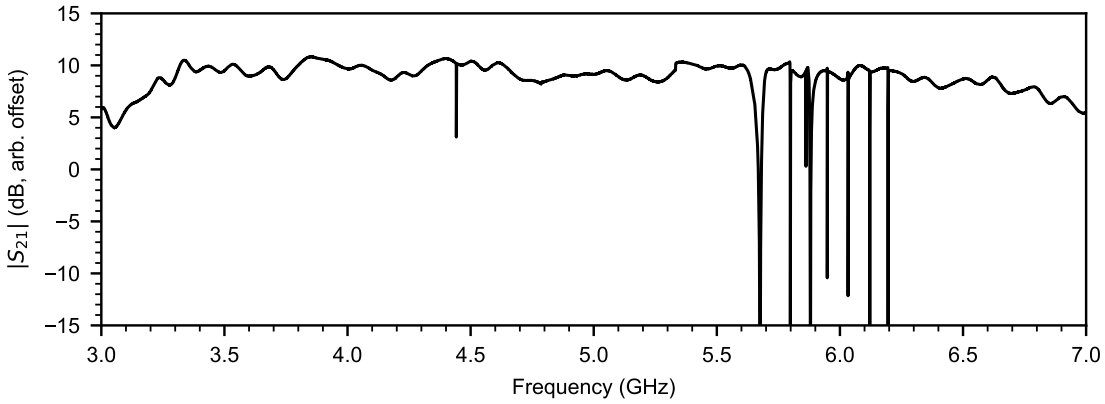

Figure 4.7: **Broad scan.** Transmission magnitude through the device over a broad frequency range. The eight designed resonances are around 6 GHz, and there is an additional unwanted resonance at 4.5 GHz. The smooth ripples are typical, attributed to impedance mismatches in the measurement signal path such as SMA connections and wirebonds. This is raw data; the overall level is arbitrary, dictated by the attenuation and amplification in the signal path. The frequency spacing of this scan is 31.25 kHz.

with the design values.

For the three highest-Q_c resonances, we repeat this measurement for a wide range of powers. The low-power measurements, where the energy in the resonator is near $\hbar\omega_0$, suggest how qubits might perform in a similar situation [64, 28]. The results are plotted in Fig. 4.10. The internal quality factor has the typical power dependence, plateauing at high photon number and decreasing by roughly an order of magnitude at low photon number. We observe low power $Q_i \approx 5\times10^5$, consistent with previous results with similar fabrication [64]. This suggests that the flip-chip assembly, including the copious epoxy and glue, is not detrimental to the resonator performance. As we will see in chapter 5, the qubit performance we observe is consistent with these Q_i measurements.

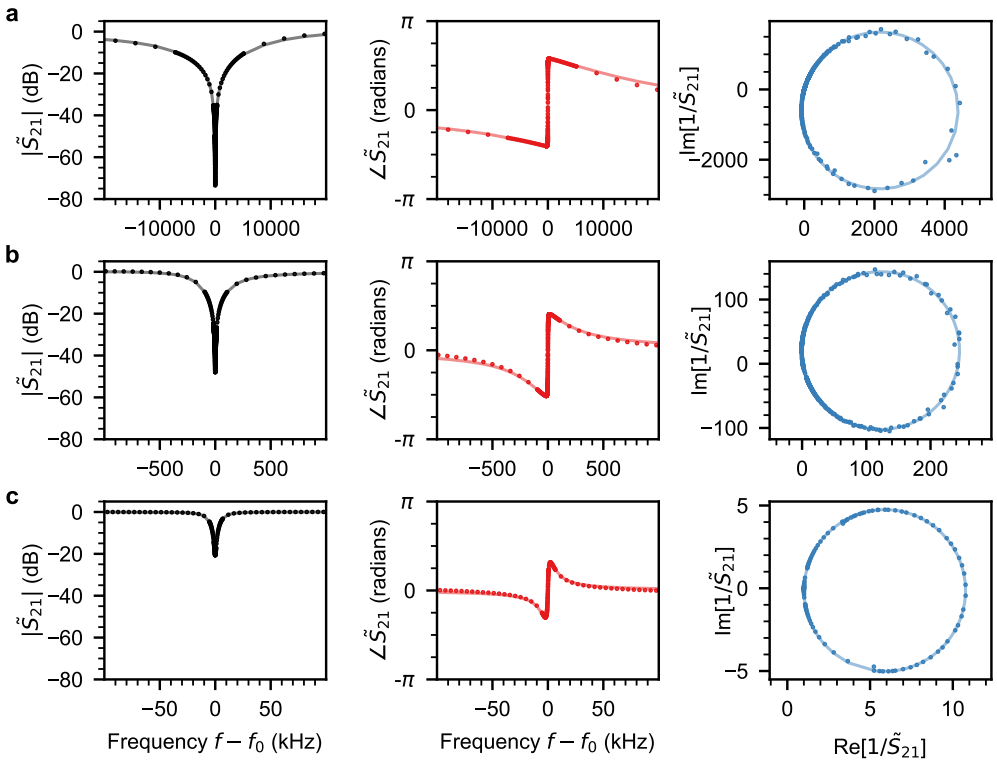

Figure 4.8: **Representative high-power scans.** We plot normalized microwave transmission $\tilde{S}_{21}$ for resonances 1 (**a**), 4 (**b**), and 8 (**c**). Points are experimental data, and light lines are from fits to Eqn. 4.25. Left (black): Magnitude. Center (red): Phase. Right (blue): Complex-valued $1/\tilde{S}_{21}$. Note the differing frequency scale. The three measurements occur at the same input power, resulting in vastly different photon numbers, about 1.6×10^3 (**a**), 1.1×10^5 (**b**), and 4.0×10^6 (**c**).

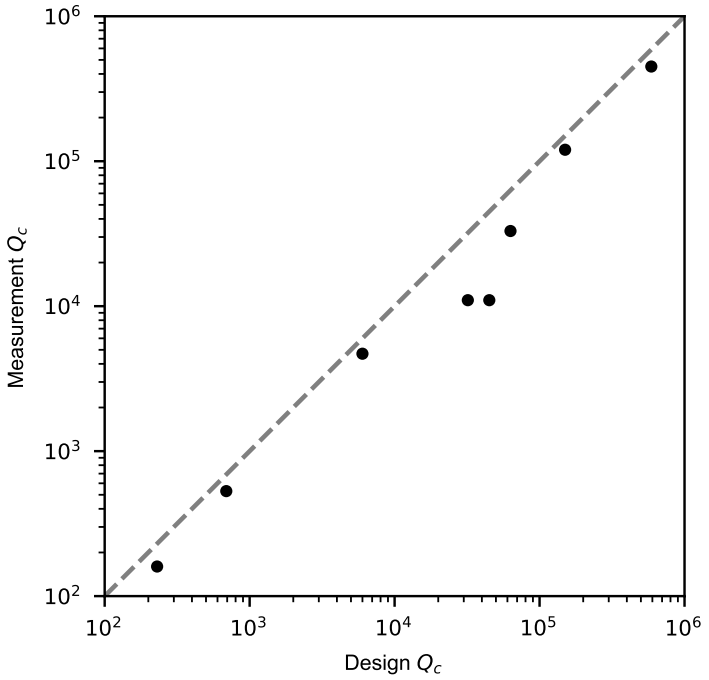

Figure 4.9: **Coupling quality factors.** Comparison of design and measurement coupling quality factors Q_c. Uncertainty in the fitted Q_c values is about 2%, smaller than the data points.

Resonator	Design Q_c	Measured Q_c
1	2.3×10^2	1.6×10^2
2	6.9×10^2	5.3×10^2
3	6.0×10^3	4.7×10^3
4	3.2×10^4	1.1×10^4
5	4.5×10^4	1.1×10^4
6	6.3×10^4	3.3×10^4
7	1.5×10^5	1.2×10^5
8	5.9×10^5	4.5×10^5

Table 4.2: Design and measured coupling quality factors Q_c for the eight coplanar waveguide resonators.

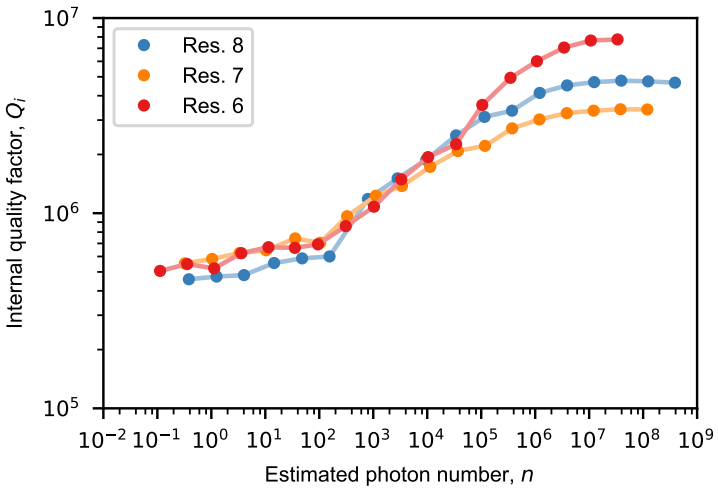

Figure 4.10: **Power dependence of internal quality factor.** Measured internal quality factors Q_i versus photon number for the three highest-Q_c resonators. Uncertainty in the fitted Q_i values is about 10%.

Chapter 5

Quantum control of surface acoustic wave phonons

In the previous three chapters, we have separately considered SAW resonators, superconducting qubits, and flip-chip integration. In this chapter, we bring these ideas together to experimentally realize quantum control of SAW phonons. We explain the hybrid device, a superconducting qubit and a SAW resonator on separate chips, and then present experimental results, culminating in the characterization of the quantum superposition $|0\rangle + |1\rangle$ in the SAW resonator.

5.1 Device description

We use a hybrid device composed of two chips. The first is a $2\,\mathrm{mm} \times 4\,\mathrm{mm}$ lithium niobate chip with the single-mode SAW resonator, discussed in chapter 2. The second

is a $6\,\text{mm} \times 6\,\text{mm}$ sapphire chip with the superconducting qubit, tunable coupler, and control wiring, discussed in chapter 3. The device is illustrated in Fig. 5.1. The control lines are labeled in Fig. 5.1d. Each line corresponds to a coplanar waveguide on the sapphire chip. On the left is the readout chain, described in detail in chapter 3, which is connected to separate input and output lines. Along the bottom are the qubit and coupler control lines: XY to resonantly drive the qubit, Z to tune the qubit frequency, and G to tune the coupler inductance.

On the right is a dedicated microwave line, D, for resonantly driving the SAW resonator. It has its own small inductive coupler to the SAW transducer. The coupling between the D line and the SAW resonator can be quantified by a coupling quality factor Q_c; it is designed to be $\sim 10^5$, much higher than the internal quality factor of the resonator ($< 10^4$), so very little energy leaves the resonator through this line. As discussed in chapter 3, driving a *linear* system such as our acoustic resonance with a classical control pulse brings about a coherent state $|\alpha\rangle$. This dedicated drive line will prove very useful in some experiments, but distinctly quantum behavior will come from interactions with the qubit.

The qubit and coupler circuit is characterized in chapter 3. The coupling between qubit and resonator comes from a mutual inductance $M = 0.13\,\text{nH}$ between two overlaid planar inductors, one on each chip. This is the same inductive coupling mechanism used in chapter 4. As described in chapter 3, we use the G control line to tune the coupling between the qubit and SAW resonator. The coupler circuit is essentially a current divider;

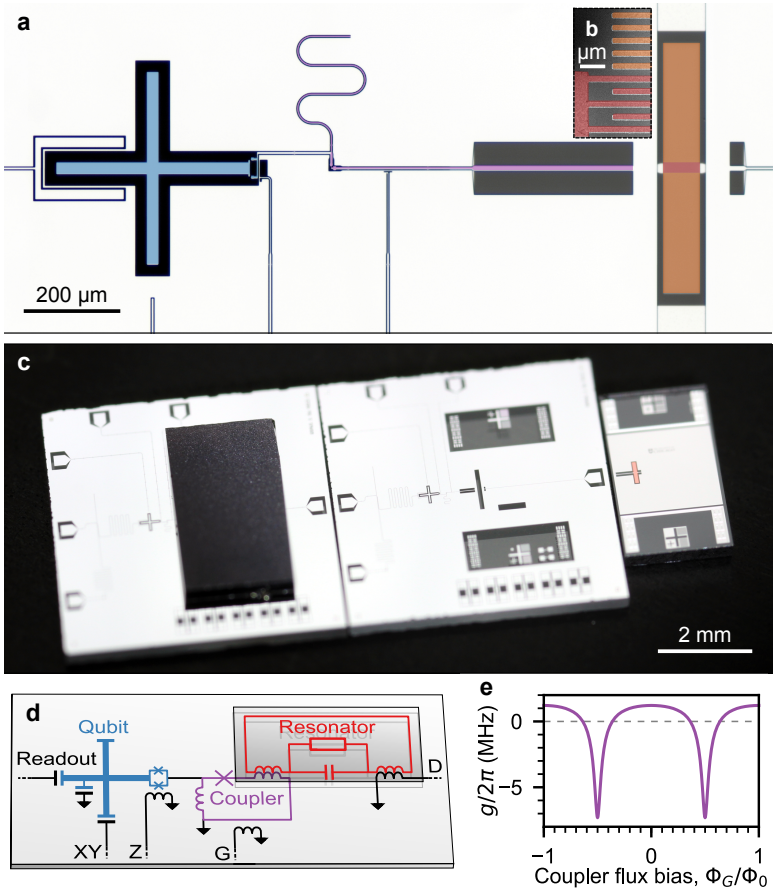

Figure 5.1: **Device description. a,** False-color optical micrograph of a transmon qubit (left, blue) and a SAW resonator (right, red transducer, orange mirrors) which interact via a tunable coupler (center, purple). The device is viewed from below through the transparent sapphire substrate, with the SAW resonator viewed through the sapphire chip on a separate lithium niobate substrate, the two separated by about 7 μm. **b,** Scanning electron micrograph of the SAW resonator with false color on the patterned aluminum film. Red: Upper left corner of the transducer. Orange: Mirror. **c,** Photograph showing the flip-chip assembly. Right: 2 mm × 4 mm lithium niobate chip with SAW resonator (red) connected to coupling inductors (horizontal lines). Center: 6 mm × 6 mm sapphire chip with qubit, coupler, and control wiring. Left: Flip-chip assembly. The SAW resonator lithium niobate chip (dark rectangle) is inverted, aligned, and affixed to the qubit sapphire chip (see Supplementary Information). **d,** Schematic circuit diagram, drawn in perspective. Each labeled control line corresponds to an external control or measurement line. The resonator is on a separate chip, represented by the small gray rectangle floating above the qubit plane. The overlaid inductors experience mutual inductive coupling. **e,** Qubit-resonator coupling $g/2\pi$ calculated for a range of coupler flux bias values Φ_G using the linear circuit model in **d** with parameters extracted from experiments.

it controls whether current from the qubit passes through the right coupling inductor, which is coupled to the SAW resonator. Current in the G control line changes the magnetic flux Φ_G through the coupler loop. This flux bias changes the phase δ across the coupler junction, setting its inductance $L_j = L_{j0}/\cos(\delta)$ (here, $L_{j0} = 1.0\,\mathrm{nH}$). When we make L_j large ($\delta \approx \pi/2$), all of the qubit current goes through the left coupler inductor, so the coupling is turned off. For small L_j, some qubit current goes through the right coupling inductor, where it interacts with the SAW resonator. It turns out the coupling is maximized when $\delta = \pi$, so $L_j = -L_{j0}$.

As in chapter 4, there is no galvanic connection between the two chips, but our coupling scheme does not require one. This brings about a large capacitance of around 5 pF between the electrically-floating "ground plane" of the SAW chip and the actually-grounded ground plane of the qubit chip, but we avoid applying any voltage across that capacitance.

5.2 Basic characterization

In this section, we present experimental results involving basic interaction between the qubit and SAW resonator. The essential qubit readout and control characterization for this device is in chapter 3; for those experiments, the coupling is turned off. Here, we use the qubit to characterize the coupling and the SAW device.

5.2.1 Wide frequency scan

First, we look at a broad frequency range, 3.5 GHz to 4.5 GHz. We excite the qubit to $|e\rangle$, bias it to the desired frequency, and set the coupling to the desired level. We then wait for a time t before measuring the qubit excited state probability P_e. The results are displayed in Fig. 5.2. We consider three representative coupler settings spanning our full tuning range. In Fig. 5.2a, the coupling is minimized; this dataset is also shown in chapter 3. We observe $T_1 \approx 20\,\mu s$. This is consistent with the low-power internal quality factors of the coplanar waveguides measured in chapter 4, $Q_i = 5 \times 10^5$.

We repeat the experiment with a moderate coupling setting (Fig. 5.2b) and with the coupling maximized (Fig. 5.2c). We take crosstalk into account by calibrating the qubit frequency as a function of Φ_Z under each of the three coupler settings independently, but we do not compensate for the effect of the applied Φ_Z pulse on the coupling due to crosstalk. The latter effect is quite small: the qubit frequency is very sensitive to Φ_Z here, so only small pulses are needed, while the coupling is much less sensitive to Φ_Z. We also perform qubit Ramsey experiments (see chapter 3) for these three coupler settings, at 3.5 GHz, 4.0 GHz, and 4.5 GHz. In each case, $T_{2,\mathrm{Ramsey}} \approx 1\,\mu s$ to $3\,\mu s$. This T_1 and $T_{2,\mathrm{Ramsey}}$ performance is consistent with previous experiments using similar qubit designs and fabrication techniques [8, 17, 51].

Having nonzero coupling shortens the qubit lifetime and makes it strongly frequency-dependent, as the transducer converts electromagnetic energy from the qubit into acoustic waves. The characteristic sinc-shaped transducer response (see chapter 2) is visible in the

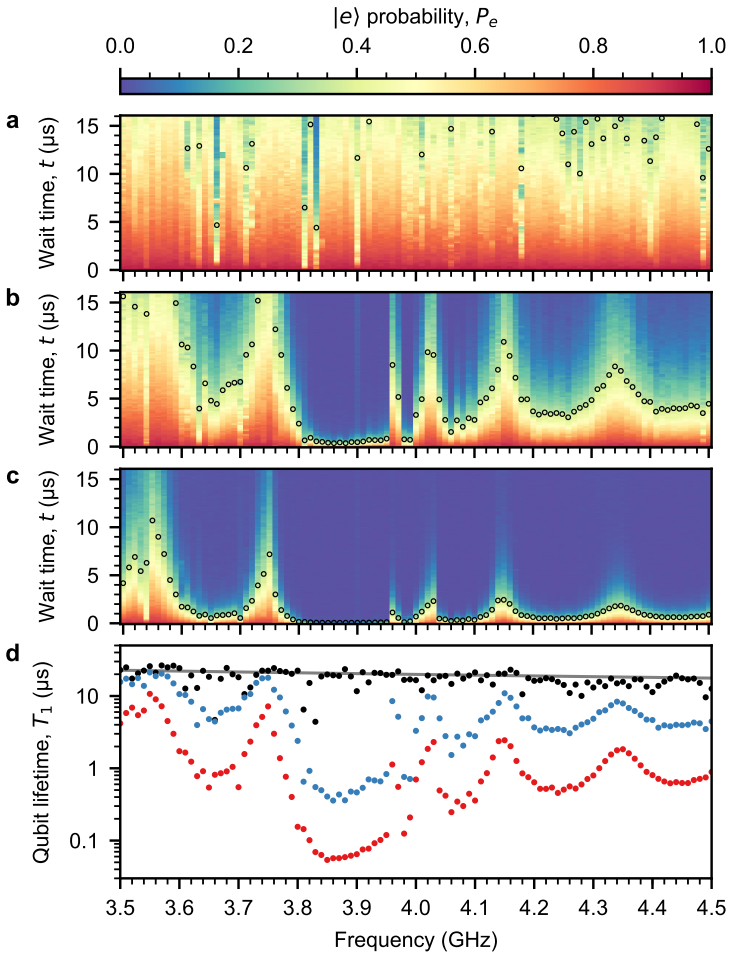

Figure 5.2: **Qubit T_1 scans. a-c,** Time-domain measurements of qubit lifetime T_1 over a wide range of qubit frequencies. The coupler flux Φ_G is different for each scan: **a** $0.35\Phi_0$, **b** $0.44\Phi_0$, and **c** $0.5\Phi_0$. Black circles are fitted T_1 values. In **a**, many T_1 fits are $\approx$20 µs, above the plot range. **d,** Fitted T_1 values plotted on a logarithmic scale, colored **a** black, **b** blue, and **c** red. Gray line: Calculated $T_1 = Q/\omega$ for $Q = 5 \times 10^5$.

T_1 maxima at 3.55 GHz, 3.75 GHz, 4.15 GHz, and 4.35 GHz. The features near 4.0 GHz involve the SAW mirrors, and we take a closer look there next.

Coupling on/off ratio

As a brief aside, an interesting figure of merit for a tunable coupling scheme is the "on/off ratio," the maximum coupling rate divided by the minimum coupling rate. We obtain a lower bound on the on/off ratio from the results in Fig. 5.2. We focus on the behavior at 3.850 GHz, where the transducer efficiently launches traveling phonons. This is the qubit's dominant loss mechanism at 3.850 GHz in Fig. 5.2b and c. At that frequency, with the coupling minimized, $T_1 = 19.8\,\mu s$, and with the coupling maximized, $T_1 = 54\,ns$. This suggest a lower bound of $(54\,ns)^{-1}/(19.8\,\mu s)^{-1} = 366$ for the on/off ratio.

5.2.2 Focusing near the resonance

We repeat the scan from Fig. 5.2b with finer frequency resolution near 4.0 GHz. This is where we expect the SAW mirrors to work, based on the design ($\lambda = 1.0\,\mu m$, $v = 4.0\,km/s$) and the experiments in chapter 2. We set $\Phi_G = 0.44\Phi_0$; this is convenient because the coupling is large enough to clearly display the frequency dependence of the SAW device, but it is small enough to not exhibit resonant swapping between the qubit and the SAW resonance. The dominant decay channel for the qubit is acoustic loss from the transducer. We plot the qubit loss $1/Q = 1/(\omega_{ge}T_1)$ as a function of qubit frequency $\omega_{ge}/2\pi$ in Fig. 5.3a, both with high resolution data at $\Phi_G = 0.44\Phi_0$ (moderate coupling) and low resolution data at $\Phi_G = 0.35\Phi_0$ (minimum coupling, from Fig. 5.2a). The

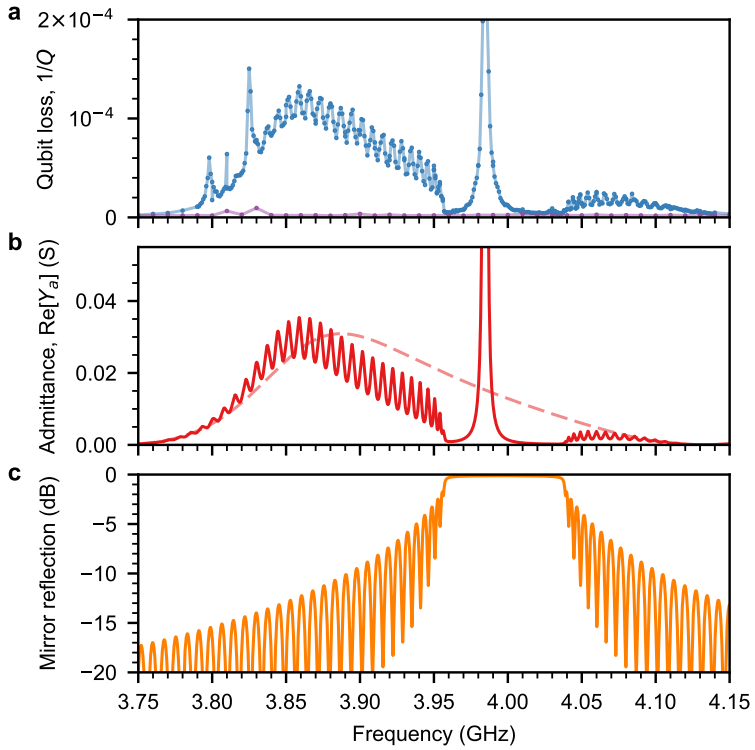

Figure 5.3: **Characterization and modeling of SAW admittance. a,** Measured qubit loss $1/Q$ as a function of qubit frequency $\omega_{ge}/2\pi$. Blue: $\Phi_G = 0.44\Phi_0$ (moderate coupling). Purple: $\Phi_G = 0.35\Phi_0$ (minimum coupling). **b,** Real part of SAW resonator acoustic admittance $\mathrm{Re}[Y_a]$, calculated with a numerical model (see Supplementary Information). Red line: Admittance of the full resonator model. The SAW resonance is the large peak at 3.985 GHz. Pink dashed line: Admittance calculated for the transducer alone, without the mirror structure. **c,** Magnitude of the model mirror reflection.

minimum-coupling $1/Q$ is near $1/(5 \times 10^5)$, as discussed earlier, and does not have much frequency dependence. However, the moderate-coupling $1/Q$ exhibits a strong frequency dependence. As we'll see, we can account for most of this frequency dependence with a model of the SAW device.

Modeling the SAW device

We observe a striking resemblance between the measured qubit loss $1/Q$ and the expected admittance of the SAW device. As discussed in chapter 2 and detailed in appendix A, we use a 1-dimensional electromechanical numerical model of the SAW device, the P-matrix [66]. With the coupling small enough to avoid resonant swapping, the real part of the SAW acoustic admittance $\mathrm{Re}[Y_a(\omega)]$ essentially presents a frequency-dependent loss to the qubit. From the circuit model perspective (see Fig. 5.1d), it's like a frequency-dependent resistance R through which the qubit is driving current. From the acoustic perspective, the qubit is driving the transducer, which converts energy into acoustic waves, where it is "lost" from the qubit.

In Fig. 5.3b-c, we illustrate the frequency dependence of a P-matrix model of the SAW device. Fig. 5.3b shows the admittance of the resonator model, which is based on the design parameters and fine-tuned to match the observed $1/Q$ frequency dependence. The SAW transducer itself can efficiently emit phonons over a wide range of frequencies, roughly from 3.8 GHz to 4.1 GHz, owing to its small number of finger pairs (20 pairs) [66]. The SAW mirror reflects efficiently in the mirror stop band from 3.96 GHz to 4.04 GHz. The resultant interference frustrates the transducer emission except when

a resonance condition is met, in this case at the single SAW resonance frequency of $\omega_r/2\pi = 3.985\,\mathrm{GHz}$. The resonator admittance near that resonance can be approximated by an equivalent resonant electrical circuit, constituting the Butterworth-van Dyke model (see chapter 2) [66]. Outside the mirror stop band, the mirror reflection decreases rapidly, and the transducer is free to emit traveling phonons. The qubit sees this as increased loss, especially from 3.85 GHz to 3.90 GHz, where the transducer is most efficient. The ripples in the out-of-band mirror reflection arise from the finite extent of each mirror (500 lines). These features are clearly displayed in the measured qubit loss. The qubit also weakly couples to unidentified resonances near 3.8 GHz. The SAW resonance at 3.985 GHz will be the focus of the rest of the chapter.

The full model is composed of a transducer model and a mirror model, both using the coupling-of-modes method [66]. We begin with the lithographically-determined device parameters and standard material parameters from Ref. [66]. We tune the mirrors' effective wave speed v_m and amplitude reflection per line r_m to reproduce the apparent stop band observed in Fig. 5.3a. We tune the transducer's speed v_t and reflection r_t to place the resonance at 3.985 GHz and reproduce the apparent asymmetric transducer response. We introduce uniform propagation loss η in both the transducer and mirror and adjust the loss so that the quality factor Q of an approximating series RLC circuit fitted to the peak in the model admittance $Y_a(\omega)$ is consistent with the resonator lifetime T_{1r} measurement (see below). These are the values used in Fig. 5.3: $v_m = 4027.0\,\mathrm{m/s}$, $v_t = 4012.5\,\mathrm{m/s}$, $r_m = -0.032i$, $r_t = -0.015i$, and $\eta = 851\,\mathrm{Np/m}$. The reported speed for a nonmetal-

lized surface at room temperature is 3979 m/s. The mirror and transducer parameters are expected to differ; the metal lines in the mirror are electrically floating, which gives stronger reflectivity. These values are consistent with cryogenic measurements of similar SAW resonators using a vector network analyzer (see chapter 2). The model series RLC circuit gives an equivalent $C_s = 12.10\,\text{fF}$, $L_s = 131.8\,\text{nH}$, and $R_s = 0.890\,\Omega$.

5.3 Resonant experiments

At this point, we have established basic qubit and coupler functionality, and we have located the SAW resonance. We now proceed to experiments involving resonant interactions between the qubit and SAW resonance. As discussed in chapter 3 and appendix B, this is a realization of the Jaynes-Cummings model with the rotating wave approximation [40, 43]. The Hamiltonian of interest is

$$H = \hbar\omega_r a^\dagger a + \hbar\omega_{ge}\sigma_+\sigma_- + \hbar g(\sigma_+ a + \sigma_- a^\dagger), \tag{5.1}$$

with SAW resonance frequency $\omega_r/2\pi = 3.985\,\text{GHz}$ and lowering operator a, qubit frequency $\omega_{ge}/2\pi$ (up to 4.7 GHz) and lowering operator σ_-, and coupling rate $g/2\pi$ (between $+1.2\,\text{MHz}$ and $-7.3\,\text{MHz}$). This neglects interactions with other aspects of the SAW admittance $Y_a(\omega)$: in these experiments, we avoid unwanted qubit loss by normally keeping the coupling small, only pulsing the coupling on when deliberately interacting with the SAW resonance.

5.3.1 Strong, tunable coupling to a single mechanical mode

We begin with some basic experiments focusing on the SAW resonance. First, we perform qubit spectroscopy near the SAW resonance under different coupling conditions. The qubit is biased to $\omega_{ge} = \omega_r + \Delta$ (detuning Δ), and then we drive the qubit XY line with a microwave pulse at frequency f near $\omega_r/2\pi$.[1] Finally, we measure the qubit.

We execute 2D scans over detuning Δ and drive frequency f. We repeat this experiment subject to the same three representative coupler settings used in Fig. 5.2, spanning the full tuning range of coupling strength $|g|$. The results are shown in Fig. 5.4a. In the minimum-coupling experiment, we simply observe a diagonal line tracking the qubit frequency; there is no visible interaction with the resonance. However, as we turn up the coupling, an avoided crossing emerges, characteristic of the resonant interaction. With the qubit tuned near the resonance ($|\Delta| \lesssim |g|$), the qubit and SAW resonance hybridize appreciably. We achieve a maximum coupling rate $|g|/2\pi = (7.3 \pm 0.1)\,\mathrm{MHz}$.

Next, we employ that maximum coupling in a simple time domain experiment, Rabi swapping. In this experiment, we first excite the qubit to $|e\rangle$, so the qubit/resonator system is in the state $|e, 0\rangle$ (qubit excited, zero phonons in the resonator). Next, we maximize the coupling and bias the qubit to detuning Δ. We allow the qubit and resonator to interact for a time τ and then measure the qubit. We plot the results, scanning detuning Δ and interaction time τ, in Fig. 5.4c. We observe the signatures of strong

[1] The pulse has a 500 ns long rectangular envelope. The 500 ns duration is the source of the apparent linewidth of about 2 MHz in the data in Fig. 5.4a. The amplitude is chosen so that the pulse is approximately a π pulse for the qubit in isolation (taking $|g\rangle$ to $|e\rangle$ when resonant with the qubit). This is why the measured qubit $|e\rangle$ probability P_e reaches close to 1.0.

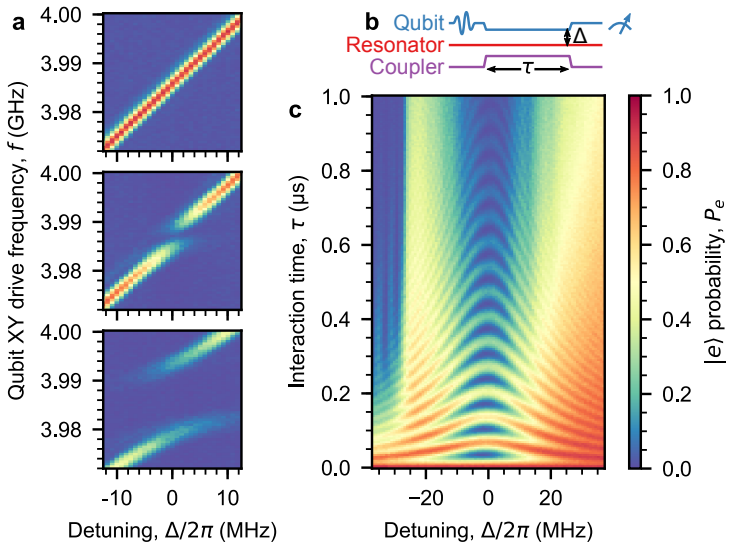

Figure 5.4: **Qubit interaction with a single mechanical mode. a,** Qubit spectroscopy near the resonator frequency for three different coupler settings. The qubit is biased to $\omega_r + \Delta$ and driven with a 500 ns long pulse at frequency f; qubit $|e\rangle$ probability P_e is plotted. Top: Minimum coupling, $g/2\pi = (0.0 \pm 0.1)$ MHz ($\Phi_G = 0.35\Phi_0$). Middle: Moderate coupling, $g/2\pi = (-2.3 \pm 0.1)$ MHz ($\Phi_G = 0.44\Phi_0$). Bottom: Maximum coupling, $g/2\pi = (-7.3 \pm 0.1)$ MHz ($\Phi_G = 0.5\Phi_0$). **b,** Rabi-swap pulse sequence. The qubit is excited to $|e\rangle$, and then the qubit is biased to $\omega_r + \Delta$ while the coupling strength is maximized. The qubit and resonator interact for a time τ, and the qubit state is then measured. **c,** Rabi-swap experiment results. Probability P_e for the qubit $|e\rangle$ state versus detuning Δ and interaction time τ. The color scale on the right applies to both **a** and **c**.

coupling between the qubit and a single mode, the SAW resonance: high-contrast oscillations in the characteristic chevron pattern, where there is a photon-phonon exchange each half-oscillation, and the period of oscillations reaches a maximum of $2\pi/(2|g|)$ at zero detuning. We also see the edge of the SAW mirror stop band around $\Delta/2\pi = -27\,\mathrm{MHz}$; this is present in Fig. 5.3 at 3.958 GHz as well. The number and amplitude of the swaps is primarily limited by the resonator lifetime T_{1r}.

We can understand this swapping in terms of the Jaynes-Cummings Hamiltonian, Eqn. 5.1. As before, we use the simple product basis states $|g, n\rangle$ and $|e, n\rangle$, where g and e refer to the qubit ground state and first excited state, respectively, and n refers to a phonon Fock state of n phonons. These are also eigenstates of Eqn. 5.1 when the coupling $g = 0$.[2] However, when the coupling $g \neq 0$, the eigenstates are combinations of $|g, n+1\rangle$ and $|e, n\rangle$ (with the exception of the ground state, which is simply $|g, 0\rangle$). In the Rabi swapping experiment, we begin in the state $|e, 0\rangle$, and when we turn on the interaction (by maximizing the coupling $|g|$ and setting the detuning $\Delta = 0$), we observe swapping between $|e, 0\rangle$ and $|g, 1\rangle$. That is because $|e, 0\rangle$ is not an eigenstate of Eqn. 5.1 when the coupling $g \neq 0$. Instead (setting $\Delta = 0$ for simplicity), the one-excitation eigenstates are $|\psi_1^{\pm}\rangle = \frac{1}{\sqrt{2}}(|g, 1\rangle \pm |e, 0\rangle)$, and the energy splitting between those eigenstates is $2\hbar g$ (this is where the avoided crossing comes from). We can then express the initial state in terms of eigenstates: $|e, 0\rangle = \frac{1}{\sqrt{2}}\left(|\psi_1^+\rangle - |\psi_1^-\rangle\right)$. Due to the energy splitting between the eigenstates, during time evolution following the Hamiltonian, the system oscillates

[2] Unfortunately, there is a collision of notation between the qubit ground state $|g\rangle$ and the coupling rate $g/2\pi$.

between $|e,0\rangle$ and $|g,1\rangle$. See appendix B for information on calculating the evolution in the presence of imperfections like loss and dephasing.

We use this experiment to define an important operation, a single-phonon swap, which exchanges the amplitudes of $|e,0\rangle$ and $|g,1\rangle$. This is executed by setting the qubit frequency to ω_r and turning on the coupling for approximately 37 ns.[3]

5.3.2 Quantum ground state

As discussed in chapter 1, these modes near 4 GHz should be very close to their ground states if they are thermalized under 50 mK.[4] However, empirically, superconducting qubit circuits don't quite thermalize to the refrigerator temperature, for reasons such as thermal radiation, quasiparticles, or other noise in the input or output lines [9, 34, 46]. It also isn't necessarily the case that a mechanical mode would thermalize. This means it is important to measure just how close the qubit and resonator get to their respective ground states.

Qubit population

To start, we focus on measuring the qubit's thermal $|e\rangle$ population. We adopt a technique called Rabi population measurement from Refs. [34, 20]. Driven transitions between $|e\rangle$ and the transmon second excited state $|f\rangle$ are used to quantify the $|e\rangle$ population by measuring the amplitudes of Rabi-like oscillations. We use a resonant pulse at frequency

[3]The swap time is nominally $2\pi/(4|g|)$, which is 34 ns for $g/2\pi = 7.3$ MHz; we end up with 37 ns in the experiment because of the $\sim$ ns risetime in the Z and G control pulses.

[4]For all the experiments in this chapter, the mixing chamber RuOx thermometer reads <7 mK.

$\omega_{ef}/2\pi$; the amplitude is normalized to the amplitude which approximately swaps $|e\rangle$ and $|f\rangle$, calibrated separately. The $|f\rangle$ thermal population is assumed to be negligible, as validated by these experiments.

Initially, the qubit state is well-described by the density matrix

$$\rho_q = (1-\epsilon_q)|g\rangle\langle g| + \epsilon_q|e\rangle\langle e| + 0|f\rangle\langle f|, \tag{5.2}$$

where $\epsilon_q \ll 1$ is the qubit's thermal $|e\rangle$ population, the quantity we wish to determine. We proceed with two experiments. The pulse sequences and results are shown in Fig. 5.5. First, we probe ϵ_q directly. We begin by applying a pulse at $\omega_{ef}/2\pi$. We vary the amplitude of this pulse in different experimental runs. This exchanges some of the $|e\rangle$ population with the (initially zero) $|f\rangle$ population. We now wish to measure the oscillations of the final $|e\rangle$ population as a function of pulse amplitude. We accomplish this by executing a standard π pulse, which completely exchanges the $|g\rangle$ and $|e\rangle$ populations, and then we measure the qubit $|g\rangle$ population directly.[5] The result is oscillations in $|g\rangle$ probability P_g with pulse amplitude. The peak-to-peak amplitude A_e of this oscillation is closely related to ϵ_q. However, it is affected by readout bias and visibility, so we need a second experiment to accurately determine ϵ_q.

The previous experiment was essentially measuring ϵ_q subject to readout imperfections, and we cancel those imperfections by also measuring $1-\epsilon_q$ in a similar manner.

[5] In our configuration, the readout actually distinguishes between "$|g\rangle$" and "not $|g\rangle$," so the $|e\rangle$ and $|f\rangle$ populations are "lumped together." It is possible to reliably distinguish $|g\rangle$, $|e\rangle$, and $|f\rangle$ in single-shot readout with better optimization of the readout circuit and amplification chain [84]. In the other experiments, $|f\rangle$ population is negligible, but it is very important here.

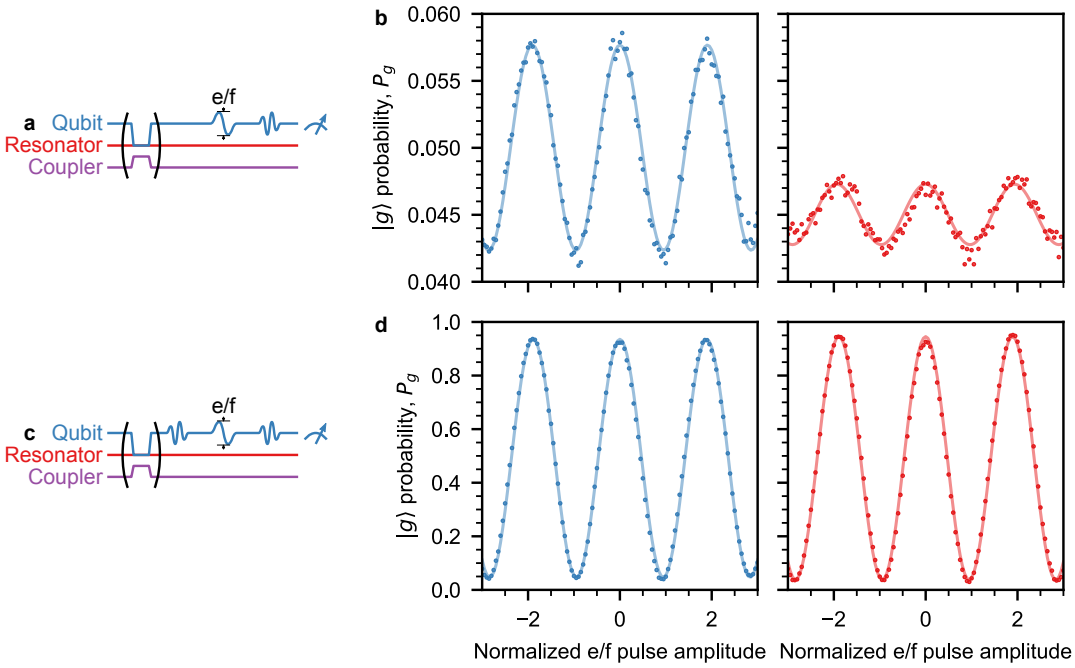

Figure 5.5: **Qubit and resonator thermometry. a,** Rabi population sequence for the excited state measurement. Following an optional swap operation, the qubit is driven with a pulse at ω_{ef} with variable amplitude and then an X_π pulse. **b,** Excited state measurement results. The small-amplitude oscillations indicate small initial excited state populations. **c,** Pulse sequence for the ground state measurement, the same as **a** with an additional X_π pulse before the ω_{ef} pulse. **d,** Ground state measurement results. The large-amplitude oscillations show near-unity initial ground state populations. In **b, d:** Left/blue: Qubit alone (no swap). Right/red: Swap. Points are from measurements; lines are cosine fits. Negative values on the horizontal axis correspond to e/f pulses with relative phase of π radians.

The experiment begins with a standard π pulse, after which the qubit state looks like

$$\rho_q = \epsilon_q|g\rangle\langle g| + (1-\epsilon_q)|e\rangle\langle e| + 0|f\rangle\langle f|. \tag{5.3}$$

We then proceed in the same manner as before, driving transitions between $|e\rangle$ and $|f\rangle$ and then deducing the $|e\rangle$ population by executing a π pulse and measuring the $|g\rangle$ population. This produces much larger-amplitude oscillations (peak-to-peak amplitude A_g), as $1-\epsilon_q \approx 1$.

Finally, we combine these results to calculate the qubit's thermal $|e\rangle$ population,

$$\epsilon_q = \frac{A_e}{A_e + A_g}. \tag{5.4}$$

In our case, A_g is very close to 1, so the correction is not very important. However, the idea is to compensate for linear readout bias and visibility, where the measured probability P_{measured} is related to the actual probability P_{actual} by

$$P_{\text{measured}} = vP_{\text{actual}} + P_0, \tag{5.5}$$

subject to visibility v and bias P_0. Roughly, taking the *amplitudes* of the oscillations removes the bias P_0, and then Eqn. 5.4 cancels out the visibility v:

$$\frac{A_e}{A_e + A_g} = \frac{v\epsilon_q}{v\epsilon_q + v(1-\epsilon_q)} = \epsilon_q. \tag{5.6}$$

Performing this experiment, as shown in Fig. 5.5, we determine that the qubit's thermal $|e\rangle$ population $\epsilon_q = 0.0169 \pm 0.0002$.

SAW resonator population

We have a similar situation in the SAW resonator; its initial state is well-described by

$$\rho_r = (1-\epsilon_r)|0\rangle\langle 0| + \epsilon_r|1\rangle\langle 1| + 0|2\rangle\langle 2|, \tag{5.7}$$

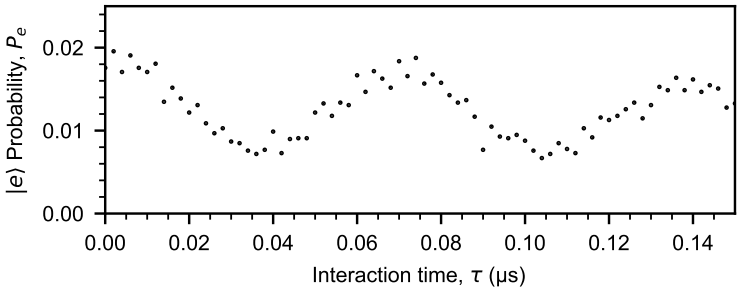

Figure 5.6: **Swapping of small thermal excited state populations.** The qubit and resonator begin in their equilibrium states, near $|g,0\rangle$ with small thermal excitations ϵ_q and ϵ_r. The qubit is biased to ω_r (detuning $\Delta = 0$) while the coupling strength is maximized. The qubit and resonator interact for a time τ, and the qubit state is then measured. The small oscillations show the exchange of the qubit thermal population with the smaller resonator thermal population.

where $\epsilon_r \ll 1$ is the SAW resonator's thermal $|1\rangle$ population. The idea is to use our swap operation (which exchanges $|e,0\rangle$ and $|g,1\rangle$ populations) to switch ϵ_r and ϵ_q, and then use the qubit to find ϵ_r. As an initial experiment, we attempt to observe this exchange in the time domain. We simply turn on the coupling and set the detuning $\Delta = 0$ for interaction time τ and then measure the qubit. The results are shown in Fig. 5.6. We observe oscillations at the same frequency as the Rabi swaps in Fig. 5.4, but the $|e\rangle$ populations are all much lower, as the only energy in the system is small thermal excitations. This experiment suggests $\epsilon_r < \epsilon_q$ (the SAW resonator is "colder" than the qubit), so the coming swap-and-measure experiment should give us an upper bound on the SAW resonator thermal population ϵ_r.

Combining the initial qubit (Eqn. 5.2) and resonator (Eqn. 5.7) density matrices, we

obtain

$$\begin{aligned}\rho = (1-\epsilon_q)(1-\epsilon_r)|g,0\rangle\langle g,0| + (1-\epsilon_q)\epsilon_r|g,1\rangle\langle g,1| \\ + \epsilon_q(1-\epsilon_r)|e,0\rangle\langle e,0| + \epsilon_q\epsilon_r|e,1\rangle\langle e,1|.\end{aligned} \tag{5.8}$$

Following a swap operation, the $|e,0\rangle$ and $|g,1\rangle$ populations are exchanged. There is a nuance here: the swap operation involves the hybridization of the single-excitation states $|e,0\rangle$ and $|g,1\rangle$, but there is also hybridization of the two-excitation states $|e,1\rangle$ and $|g,2\rangle$. The resultant swapping between $|e,1\rangle$ and $|g,2\rangle$ occurs at a faster rate (by a factor of $\sqrt{2}$). These thermal populations $\epsilon \sim 10^{-2}$, so terms in Eqn. 5.8 then fall into three categories: $O(1)$, $O(\epsilon \sim 10^{-2})$, and $O(\epsilon^2 \sim 10^{-4})$. The $|e,1\rangle$ term is $O(\epsilon^2)$, so it is insignificant compared to the $O(\epsilon)$ $|g,1\rangle$ and $|e,0\rangle$ terms. Under the approximation that the swap does nothing to the small $|e,1\rangle$ population, we obtain

$$\begin{aligned}\rho_{\text{swapped}} = (1-\epsilon_q)(1-\epsilon_r)|g,0\rangle\langle g,0| + \epsilon_q(1-\epsilon_r)|g,1\rangle\langle g,1| \\ + (1-\epsilon_q)\epsilon_r|e,0\rangle\langle e,0| + \epsilon_q\epsilon_r|e,1\rangle\langle e,1|.\end{aligned} \tag{5.9}$$

We then perform a partial trace to find the qubit's state in isolation,

$$\rho_{q,\text{swapped}} = \langle 0|\rho_{\text{swapped}}|0\rangle + \langle 1|\rho_{\text{swapped}}|1\rangle \tag{5.10}$$

$$= \left[(1-\epsilon_q)(1-\epsilon_r) + \epsilon_q(1-\epsilon_r)\right]|g\rangle\langle g| + \left[(1-\epsilon_q)\epsilon_r + \epsilon_q\epsilon_r\right]|e\rangle\langle e| \tag{5.11}$$

$$= (1-\epsilon_r)|g\rangle\langle g| + \epsilon_r|e\rangle\langle e|. \tag{5.12}$$

Following the swap operation, the qubit has taken on the thermal population from the resonator. Since we know $\epsilon_r < \epsilon_q$, imperfections in the swap and subsequent heating in the qubit would make our measurement in the qubit higher than the initial resonator population. However, these effects should be small; the swap has high contrast (above 90%), and the duration of the Rabi population measurement sequence ($\approx$100 ns) is much shorter than the qubit's characteristic thermalization time ($T_1 \sim 10\,\mu$s).

We carry out the experiment, first executing a swap and then immediately proceeding with the Rabi population measurement sequence. The results are plotted in Fig. 5.5. We obtain a post-swap qubit excited state population of 0.0049 ± 0.0002, an upper bound on the resonator thermal $|1\rangle$ population ϵ_r. This suggests the SAW resonator is at least 99.5% in its quantum ground state of motion.

5.3.3 Single-phonon T_1 and T_2

We now turn to the SAW resonator single-phonon lifetime T_{1r} and coherence time T_{2r}. The T_{1r} measurement is simple. We excite the qubit to $|e\rangle$ with an X_π pulse, swap that into the resonator (nominally creating $|1\rangle$), let that state decay for a time t, swap the state back into the qubit, and measure the qubit. The results are shown in Fig. 5.7. We observe the expected exponential decay, consistent with energy lifetime $T_{1r} = (148 \pm 1)$ ns. The probability at $t = 0$ is about 0.7; this is less than 1.0 because of loss (primarily in the resonator) during the swaps. The point at $t = 0$ is closely related to Fig. 5.4c at detuning $\Delta = 0$ and interaction time $\tau \approx 70$ ns. This lifetime, together with the maximum coupling

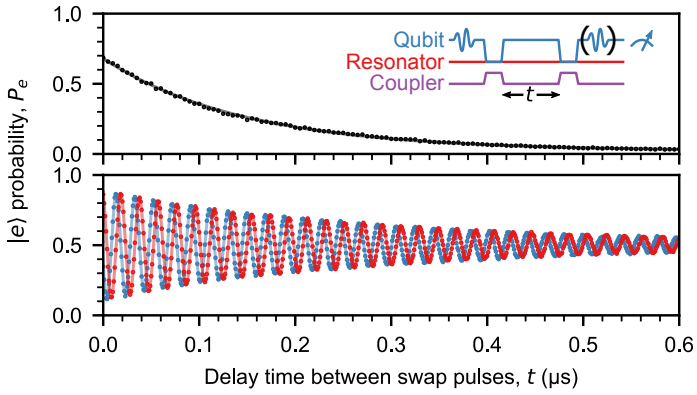

Figure 5.7: **Single-phonon evolution.** Top: Energy lifetime T_{1r} experiment (points) plotted with exponential-decay fit. Bottom: Coherence time T_{2r} experiment (points) plotted with decaying sinusoidal fits. Inset: Pulse sequence. The qubit is excited with an X_π (for T_{1r}) or $X_{\pi/2}$ (for T_{2r}) pulse, we execute a swap, we wait a delay time t, we execute another swap, and we measure the qubit. For the T_{2r} experiment, the qubit measurement is preceded by a second $\pi/2$ pulse (blue: $X_{\pi/2}$, red: $Y_{\pi/2}$) for qubit tomography (see below).

$|g|/2\pi = (7.3 \pm 0.1)\,\mathrm{MHz}$, is the main limitation on the subsequent experiments. It is dominated by loss in the transducer and mirrors, which could include scattering into bulk acoustic modes and other material losses in the interfaces and aluminum lines.

Next, we measure the single-phonon coherence time T_{2r}. This experiment involves generating a quantum superposition of $|0\rangle$ and $|1\rangle$ and observing how it decays; it is affected by the energy lifetime T_{1r} measured above, and it also detects any additional dephasing brought about by instability in the resonance frequency. Here, we pay close attention to the phases and frequencies. We excite the qubit with an $X_{\pi/2}$ pulse, bringing it to $\frac{1}{\sqrt{2}}(|g\rangle - i|e\rangle)$. We then execute a swap (nominally creating $\frac{1}{\sqrt{2}}(|0\rangle - i|1\rangle)$, although there is some subtlety in the relative phase because of the difference between the resonator and qubit idle frequencies) and wait for a time t.

During the wait, the qubit is idling at $\omega_{ge}/2\pi = 4.038\,\mathrm{GHz}$. The phase reference frame of the experiment is rotating at the qubit idle frequency, so the relative phase of the SAW resonator state should evolve at the idle detuning frequency $\Delta/2\pi = 53\,\mathrm{MHz}$.

We then swap the state back into the qubit. At this point, directly measuring the qubit $|e\rangle$ probability P_e will result in exponential decay with T_{1r}. Instead, we need to perform a second $\pi/2$ pulse before measuring the qubit. That measurement strongly depends on the phase alignment of the $\pi/2$ pulse and the superposition state in the qubit. We actually perform full tomography on the qubit (see below for details) to measure it along the X and Y directions. These measurements are shown in Fig. 5.7. We observe the expected exponentially-decaying oscillations, 90° out of phase. The oscillations are at the idle detuning frequency $\Delta/2\pi = 53\,\mathrm{MHz}$, exhibiting quantum interference between the resonator state and the qubit tomography pulses. We obtain $T_{2r} = (293 \pm 1)\,\mathrm{ns}$, where the ratio $T_{2r}/T_{1r} \approx 2$ is consistent with little to no additional phase decoherence, as expected for a harmonic oscillator.

Towards $|2\rangle$

It would be very interesting to successively excite the qubit and swap excitations into the qubit several times to realize more exotic quantum states, as has been demonstrated with a qubit and a coplanar waveguide resonator [43]. Our device is right on the threshold of having this capability. We illustrate this by attempting to create the two-phonon Fock state $|2\rangle$ by twice exciting the qubit and swapping its excitation into the SAW resonator. We show the result in Fig. 5.8. The experiment is limited by the resonator

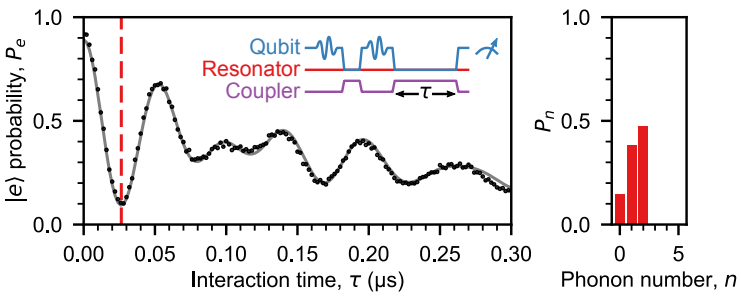

Figure 5.8: **Generation of the $|2\rangle$ state.** Left: Qubit evolution nominally starting in $|e,1\rangle$. Black points: Experiment. Gray line: Numerical model. Red dashed line: Time when the resonator is closest to $|2\rangle$. Inset: Experiment pulse sequence. The qubit is excited (X_π), that is swapped into the resonator, the qubit is excited again (X_π), and then the qubit interacts with the resonator for time τ. Right: The phonon number probability distribution at the red dashed line in **a** calculated from the numerical model.

lifetime T_{1r}, which is comparable to the duration of the pulse sequence to generate $|2\rangle$, about 100 ns. We do observe higher-frequency oscillations in the initial interaction, as expected in the Jaynes-Cummings model. The experiment is in excellent agreement with our numerical model of the system (see appendix B). The resonator state is closest to $|2\rangle$ at the minimum in P_e near interaction time $\tau = 26$ ns. At that time, the resonator state suggested by the model is a statistical mixture

$$\rho_r = 0.145|0\rangle\langle 0| + 0.382|1\rangle\langle 1| + 0.473|2\rangle\langle 2|. \tag{5.13}$$

5.3.4 Qubit tomography

Our qubit measurement naturally distinguishes between the qubit energy eigenstates $|g\rangle$ and $|e\rangle$, which we identify with the Z basis, but it is also useful to measure qubits along

the X and Y directions. Measuring along all three directions gives the full qubit density matrix; this is referred to as qubit tomography. This was touched on in the discussion of the phonon coherence time T_{2r} experiment (see above). Here, we discuss it in greater detail and present additional experiments.

To conduct qubit tomography, the standard qubit $|e\rangle$ probability P_e measurement follows a tomography microwave pulse. We repeat the experiment using each of these tomography pulses: $X_{\pi/2}$, $X_{-\pi/2}$, $Y_{\pi/2}$, $Y_{-\pi/2}$, X_{π}, $X_{-\pi}$, Y_{π}, $Y_{-\pi}$, and no pulse. The negative phase pulses ensure a symmetric measurement. For example, the qubit measurement along the Y direction is $[P(X_{-\pi/2}) + (1 - P(X_{\pi/2}))]/2$. Put that way, in Figs. 5.7 and 5.9, blue is measurement along -Y, and red is measurement along X. The tomography allows construction of a Bloch vector representing the qubit state with entries $(\langle\sigma_X\rangle, \langle\sigma_Y\rangle, \langle\sigma_Z\rangle)$, where $\langle\sigma_i\rangle = 2P(i) - 1$ is the expectation value of the Pauli operator i, and $P(i)$ is the measured probability of the qubit along direction $i = X, Y, Z$.

We conduct additional experiments with qubit tomography to study the interaction between the qubit and SAW resonator. In Fig. 5.9a, we show Rabi swapping between $|e, 0\rangle$ and $|g, 1\rangle$. Ideally, the X and Y measurements would be at $P_e = 0.5$; imperfections in state preparation or the swap pulses introduce errors resulting in small oscillations about $P_e = 0.5$ at the idle detuning frequency. We also plot the length of the qubit Bloch vector, which becomes small halfway through a swap, when the qubit is near a uniform statistical mixture. This is because we only measure the qubit, while some of the energy is left unmeasured in the resonator. The Bloch vector recovers on each

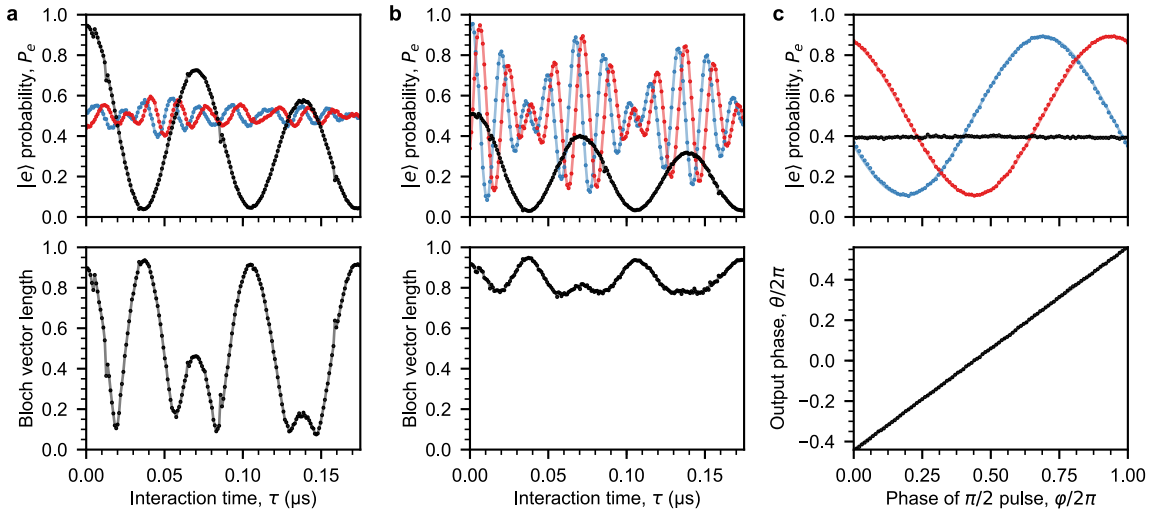

Figure 5.9: **Qubit tomography and interaction with the SAW resonator.** Top row: Qubit tomography results. Black, blue, and red show measurement along Z, -Y, and X, respectively. **a,** Resonant Rabi swapping, as in Fig. 5.4c at $\Delta = 0$. The qubit starts in $|e\rangle$. Top: Qubit tomography. Bottom: Bloch vector length calculated from tomography. **b,** Resonant Rabi swapping with the qubit starting in $\frac{1}{\sqrt{2}}(|g\rangle - i|e\rangle)$. **c,** Measurement of the phase of superposition states after swapping in and out of the resonator. Top: Qubit tomography of the final state with constant and sinusoidal fits. Bottom: Final state phase θ, measured from the X axis, with unity-slope linear fit.

oscillation, suggesting entanglement between the qubit and resonator. In Fig. 5.9b, we show a similar experiment with the qubit starting in the superposition $\frac{1}{\sqrt{2}}(|g\rangle - i|e\rangle)$. Following one swap, the qubit is near the ground state, and as the state swaps back into the qubit, we observe large X and Y oscillations, showing that the superposition persists. In Fig. 5.9c, we demonstrate control of the phase of the superposition of the SAW resonator. The qubit starts in $\frac{1}{\sqrt{2}}\left(|g\rangle - ie^{i\phi}|e\rangle\right)$. The state is swapped into the resonator, we wait 5 ns, and then the state is swapped back to the qubit. We then measure the final state phase θ; it equals ϕ plus an offset determined by the relative phase accumulated during the sequence.

5.3.5 Coherent states

So far, we have been exciting the SAW resonator by taking energy from the qubit. We have another, more direct way: the D control line shown in Fig. 5.1, discussed earlier. In brief, a microwave input line ends in a shorted coplanar waveguide with weak mutual inductive coupling to the transducer in the SAW resonator, so a resonant microwave pulse excites the resonance. This is used to execute coherent displacements of the resonator state by complex amplitude α, represented by the operator $D_\alpha = \exp\left(\alpha a^\dagger - \alpha^* a\right)$.

We conduct two experiments with displaced resonator states. Fig. 5.10a has the qubit interact with a coherent state $|\alpha\rangle$; for larger α, we see the higher frequencies characteristic of higher harmonic oscillator levels. In Fig. 5.10b, the resonator is prepared in (nominally) $|1\rangle$ prior to the displacement. We see excellent agreement between the experiment and

numerical model. One interesting feature present in the experiment, but not captured by the model, is the weak revivals around 0.2 µs and $|\alpha| = 5$. This may involve interactions with higher qubit levels; the model only uses two. For this modeling, we use 50 harmonic oscillator levels; otherwise, it is as discussed in appendix B. We use the numerical model to create a *prediction* of the experimental results using the pulse sequence and parameters from the previous experiments.

We need a calibration between the experimental pulse amplitude and the displacement amplitude α. We take a slice of the experiment in Fig. 5.10a where the interaction time τ is precisely the duration of our swap pulse. We fit the experiment to the numerical model (see appendix B) with one parameter; that parameter is the calibration to convert between experimental pulse amplitudes and α values.

5.3.6 Wigner tomography

Wigner tomography [58, 5, 10, 40, 43, 96] is a way of experimentally mapping out the Wigner function of a harmonic oscillator coupled to a qubit. This contains the same information as the density matrix; it is a direct characterization of the quantum state. Here, we take a close look at the states $|0\rangle$, $|1\rangle$, and a superposition $\frac{1}{\sqrt{2}}(|0\rangle + |1\rangle)$ (see above for a discussion about the phase of this superposition state). We closely follow the experimental methods of Ref. [43], though here we have a mechanical resonator and tunable coupling.

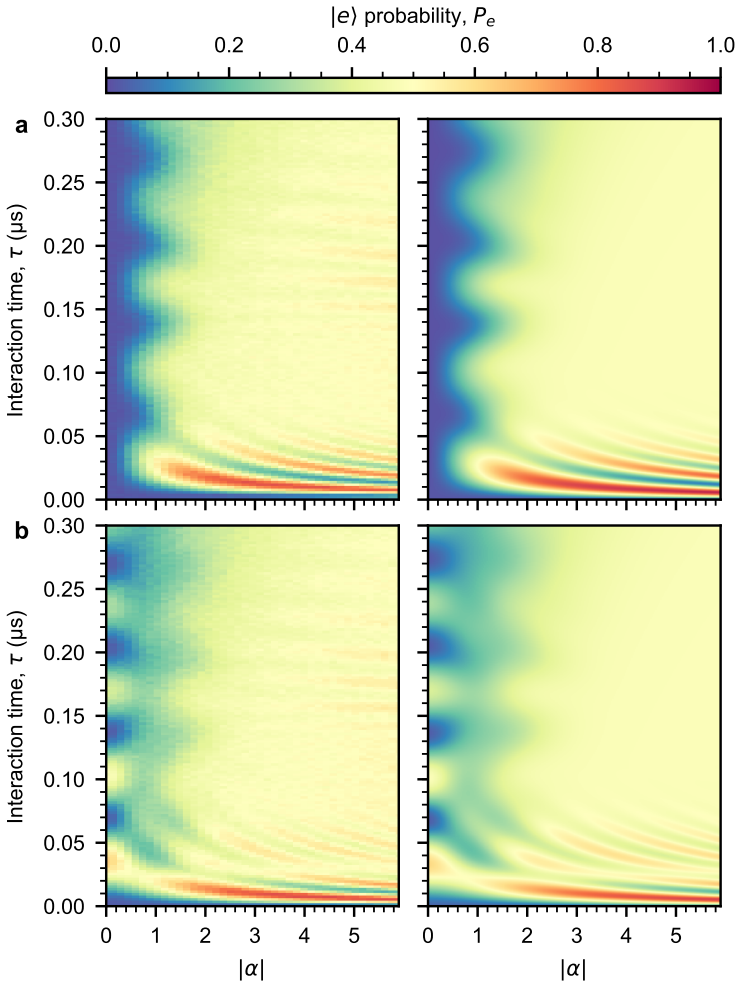

Figure 5.10: **Qubit interaction with displaced SAW resonator states.** Left: Experiment. Right: Numerical model prediction. The qubit begins in $|g\rangle$ and interacts with a displaced resonator state. **a,** Initial resonator state $D_\alpha|0\rangle = |\alpha\rangle$. **b,** Initial resonator state $D_\alpha|1\rangle$.

Experiment overview

The Wigner function is a real-valued function of α. It is proportional to the phonon number parity of the resonator state after it is displaced by $-\alpha$ (note the sign). Consider the density matrix ρ of an initial resonator state we wish to characterize. Displacing the state by $-\alpha$, it becomes

$$\rho'(-\alpha) = D_{-\alpha}\rho D_{-\alpha}^{\dagger} = D_{-\alpha}\rho D_{\alpha}. \tag{5.14}$$

Considering its diagonal entries ρ'_{nn}, we compute the phonon number parity

$$\Pi = \sum_{n=0}^{\infty}(-1)^n \rho'_{nn}. \tag{5.15}$$

Finally, here is the expression for the Wigner function:

$$W(\alpha) = \frac{2}{\pi}\sum_{n=0}^{\infty}(-1)^n \rho'_{nn}(-\alpha). \tag{5.16}$$

In practice, these sums are truncated at some N above which ρ'_{nn} is negligible for every α; here we use $N = 9$.

The main experimental challenge is deducing the phonon number parity; following Ref. [43], we use time-domain resonant interactions with the qubit. First, as before, we prepare the desired state in the resonator. Second, we displace the resonator state with complex coherent amplitude $-\alpha$; this amplitude is the parameter we will be scanning (real and imaginary part, or equivalently, magnitude and phase). Third, we allow the qubit and resonator to interact for a time τ, and finally, we measure the qubit (just $|e\rangle$ probability, not qubit tomography). This is very similar to what we show in Fig. 5.10. For each desired resonator state, we scan the interaction time τ, Re[α], and Im[α]. From

here, we analyze each α value individually to determine $W(\alpha)$.

Example

Here, we consider one representative "pixel" of the Wigner tomography for $|1\rangle$, in particular $-\alpha = 0.5$. The associated experiment is the time evolution of the qubit $|e\rangle$ probability as the qubit interacts with the displaced resonator state; this is plotted in Fig. 5.11. This is closely related to the experiment in Fig. 5.10b. When we calculate the "numerical model" data for Fig. 5.10, we use the model to *predict* what would happen based on our knowledge of the system parameters and pulse sequence.

Here, we do something different. This procedure does not know about the state preparation or displacement. We ask the model, "Which initial phonon probability distribution P_n best explains the observed qubit evolution $P_e(\tau)$?" To answer this question, we use a least-squares optimization to find the probability distribution P_n ($n = 0, 1, \ldots 9$) that, when inserted into our model, generates $P_e(\tau)$ closest to the experimental observation. In Fig. 5.11, we plot the fitted distribution P_n and the evolution $P_e(\tau)$ it implies. We do this same calculation for each displacement $-\alpha$, generating a set of probability distributions $\{P_n(-\alpha)\}$, from which we calculate the Wigner function $W(\alpha)$ using Eqn. 5.16. For further details, see appendix C.

Wigner functions

We perform this experiment and analysis on $|0\rangle$, $|1\rangle$, and a superposition $\frac{1}{\sqrt{2}}(|0\rangle + |1\rangle)$. The results are displayed in Fig. 5.12, along with the independent predictions of the

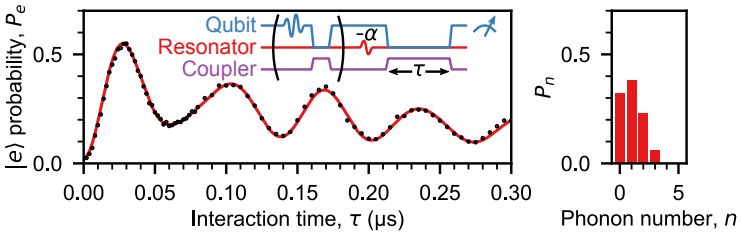

Figure 5.11: **Example qubit time evolution.** Left: Example Wigner tomography experiment showing the qubit evolution as it interacts with a displaced resonator $|1\rangle$ state (black points). Inset: Mechanical state synthesis and Wigner tomography pulse sequence. If needed, the qubit is excited to the desired state, which is then swapped into the resonator. To determine the Wigner function $W(\alpha)$, the resonator state is displaced with coherent amplitude $-\alpha$. The qubit interacts with the displaced resonator state for a time τ before it is measured, allowing the phonon number distribution of the displaced state to be determined. Right: Example phonon number distribution P_n resulting from a fit to the experiment (red line in the left plot).

numerical model. We observe excellent agreement between the experimental results and the predictions, with the key features of the Wigner functions clearly displayed, including negative values (characteristic of non-classical states) and a distinct dependence on the phase of α for the superposition state.

As we have discussed, there is some nuance about the phase of the superposition state. We demonstrate complete control of that phase in Fig. 5.9c. For the Wigner tomography experiment, we generate the superposition from the qubit state $\frac{1}{\sqrt{2}}(|e\rangle - i|g\rangle)$. The details of the pulse sequence will bring about a somewhat arbitrary phase shift, the time integral of the detuning $\Delta(t)$. This manifests itself in a rotation of the Wigner function; we manually rotate the result 90° to align it with $\frac{1}{\sqrt{2}}(|0\rangle + |1\rangle)$, as in Ref. [43].

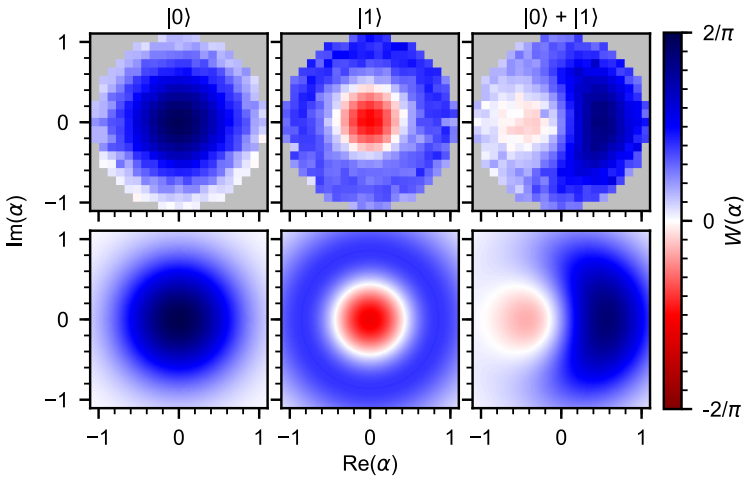

Figure 5.12: **Wigner tomography of SAW resonator quantum states.** Top: Experimental results. Bottom: Prediction of the numerical model.

Density matrices and fidelities

We convert the measured Wigner functions into density matrices. We use 4×4 matrices ($n = 0, 1, 2, 3$), as we expect the populations above $n = 1$ will be very small. We ask the model, "Which density matrix, subject to a set of displacements $\{-\alpha\}$, best explains the observed probability distributions $\{P_n(-\alpha)\}$?" Again, we use least-squares optimization to accomplish this; see appendix C for details. From the density matrix ρ and the desired resonator state $|\psi\rangle$, we calculate the fidelity $F = \sqrt{\langle\psi|\rho|\psi\rangle}$.

We print the density matrices calculated from the experiment below. We have not rotated the superposition state, and we calculate its fidelity by comparing it to the closest state of the form $\frac{1}{\sqrt{2}}\left(|g\rangle + e^{i\phi}|e\rangle\right)$ (in this case, $\phi = \pi/2$). Each entry, real and imaginary

part, has an uncertainty of roughly 0.01.

$$\rho_0 = \begin{bmatrix} 0.971 & -0.023i & 0.001+0.001i & 0.008i \\ 0.023i & 0.002 & 0.001-0.004i & -0.005-0.001i \\ 0.001-0.001i & 0.001+0.004i & 0.011 & -0.002-0.013i \\ -0.008i & -0.005+0.001i & -0.002+0.013i & 0.016 \end{bmatrix} \tag{5.17}$$

This gives a fidelity $F(|0\rangle) = 0.985 \pm 0.005$. The numerical prediction has fidelity 0.998, primarily limited by thermal occupation.

$$\rho_1 = \begin{bmatrix} 0.231 & 0.001+0.047i & -0.001i & 0.001+0.003i \\ 0.001-0.047i & 0.737 & 0.004+0.051i & 0.002i \\ 0.001i & 0.004-0.051i & 0.020 & -0.004-0.014i \\ 0.001-0.003i & -0.002i & -0.004+0.014i & 0.012 \end{bmatrix} \tag{5.18}$$

This gives a fidelity $F(|1\rangle) = 0.858 \pm 0.007$. The numerical prediction has fidelity 0.879, primarily limited by loss in the SAW resonator.

$$\rho_{0+1} = \begin{bmatrix} 0.610 & -0.399i & 0.008-0.005i & 0.002-0.003i \\ 0.399i & 0.377 & 0.007-0.010i & -0.009+0.001i \\ 0.008+0.005i & 0.007+0.010i & 0.003 & -0.002-0.003i \\ 0.002+0.003i & -0.009-0.001i & -0.002+0.003i & 0.010 \end{bmatrix} \tag{5.19}$$

This gives a fidelity $F\left(\frac{1}{\sqrt{2}}(|0\rangle + i|1\rangle)\right) = 0.945 \pm 0.006$. The numerical prediction has fidelity 0.962, primarily limited by loss in the SAW resonator.

Chapter 6

Conclusion

Having presented the background and experimental results in detail, we finally take a step back to review the key results of this thesis and briefly discuss the outlook for follow-up research.

6.1 Summary

Surface acoustic wave devices represent a mature technology in classical signal processing, and there are hopes that they could be useful in emerging quantum technologies. In this thesis, we have taken a significant step in that direction.

We begin by discussing surface acoustic wave resonators with strong electromechanical coupling. This strong coupling comes from the outstanding piezoelectric properties of lithium niobate, and it allows us to couple a surface acoustic wave resonator to a superconducting qubit without compromising qubit performance. We then describe supercon-

ducting qubits, a promising technology for quantum computing, in particular discussing tunable inductive coupling, which is crucial for protecting the qubit from unwanted interactions and loss. Motivated by the need to couple two quantum devices on separate substrates, we explore a simple technique for flip-chip integration, which is meant to be accessible to any lab capable of contact photolithography.

Finally, we bring our qubit and surface acoustic wave resonator together in a flip-chip assembly with tunable coupling. We demonstrate good qubit performance, clear measurement and modeling of the surface acoustic wave device, and strong tunable coupling. The surface acoustic wave resonator is cooled to the quantum ground state of motion with at least 99.5% probability. We measure the properties of a single phonon and closely examine the interaction with the qubit. We also examine coherent states of the surface acoustic wave resonator. We then apply several experimental techniques together to conduct Wigner tomography, fully characterizing several surface acoustic wave quantum states. Most significantly, we demonstrate the quantum superposition $|0\rangle + |1\rangle$ with fidelity $94.5 \pm 0.6\%$.

6.2 Outlook

We hope this work can serve as a foundation for a wide variety of novel quantum experiments. Our hybrid architecture is naturally scalable, and it could be adapted to experiments with bulk acoustic waves [20] and electro-optomechanical devices [12, 94]. This experiment is relatively simple, coupling a qubit to a single mechanical mode. The

main limitation here is the phonon energy lifetime $T_{1r} = 148\,\text{ns}$ together with the maximum coupling rate $|g|/2\pi = 7.3\,\text{MHz}$. There is room for improvement in both of these, for example from refining the design and fabrication of the surface acoustic wave resonator and using a more aggressive coupling circuit. Such improvements may enable natural extensions of this work involving more exotic mechanical quantum states in one or more acoustic modes.

Another research direction is to use *traveling* surface acoustic waves launched and detected by transducers with tunable inductive coupling to superconducting qubits. This is a natural arena for bringing numerous quantum optics experiments into the acoustic domain using phononic "flying qubits." There may also be technological applications such as filtering and other manipulations of tightly-confined, slowly-propagating quantum signals.

Finally, this work represents a key piece in the "hybrid quantum systems" puzzle. Many other systems, such as optical photons and spins in semiconductors, can couple to surface acoustic waves. Integration of several of these systems in one experiment is a worthy, challenging goal.

Appendix A

Surface acoustic wave modeling

We use a standard approach for modeling SAW devices, the P-matrix (see Ref. [66], especially appendix D). This is essential for both designing devices and understanding experiments.

A.1 P-matrix

The P-matrix is a 3×3 matrix where each element is frequency-dependent (we're implicitly working in the frequency domain). It is reminiscent of the n-port microwave network scattering matrix S [75]. The P-matrix represents a device with two acoustic ports, to the left (port 1) and right (port 2), and one electrical port (port 3).

A.1.1 Definition

The P-matrix relates incoming and outgoing waves at the three ports. This is easiest to think of in terms of a transducer, where incident acoustic waves can reflect, transmit, or be converted into electrical signals, and incident electrical signals can reflect or be converted into acoustic waves. An acoustic wave is described by a complex amplitude A, proportional to (and in phase with) the surface potential accompanying the acoustic wave, such that the power in the wave is $\frac{1}{2}|A|^2$. We identify an amplitude for the incoming and outgoing waves at each acoustic port (1 and 2), as well as the current I and voltage V at the electrical port (3). The P-matrix is defined according to

$$\begin{bmatrix} A_{1,\text{out}} \\ A_{2,\text{out}} \\ I \end{bmatrix} = \begin{bmatrix} P_{11} & P_{12} & P_{13} \\ P_{21} & P_{22} & P_{23} \\ P_{31} & P_{32} & P_{33} \end{bmatrix} \begin{bmatrix} A_{1,\text{in}} \\ A_{2,\text{in}} \\ V \end{bmatrix}. \tag{A.1}$$

This is illustrated in Fig. A.1a.

A.1.2 Physical interpretation

The upper-left portion (indices 1 and 2) is essentially a 2-port scattering matrix for acoustic waves, in close analogy to the microwave scattering matrix S. These are the only nonzero elements in passive components such as open spaces and mirrors (see below).

The lower-right element P_{33} is the electrical admittance Y of the device; in the absence of incident acoustic waves ($A_{i,\text{in}} = 0$), $I = P_{33}V$. This includes the capacitance C of the transducer in parallel with the acoustic admittance: $Y(\omega) = i\omega C + Y_a(\omega)$.

The other elements P_{i3} and P_{3i} are related to transduction. For a short-circuited

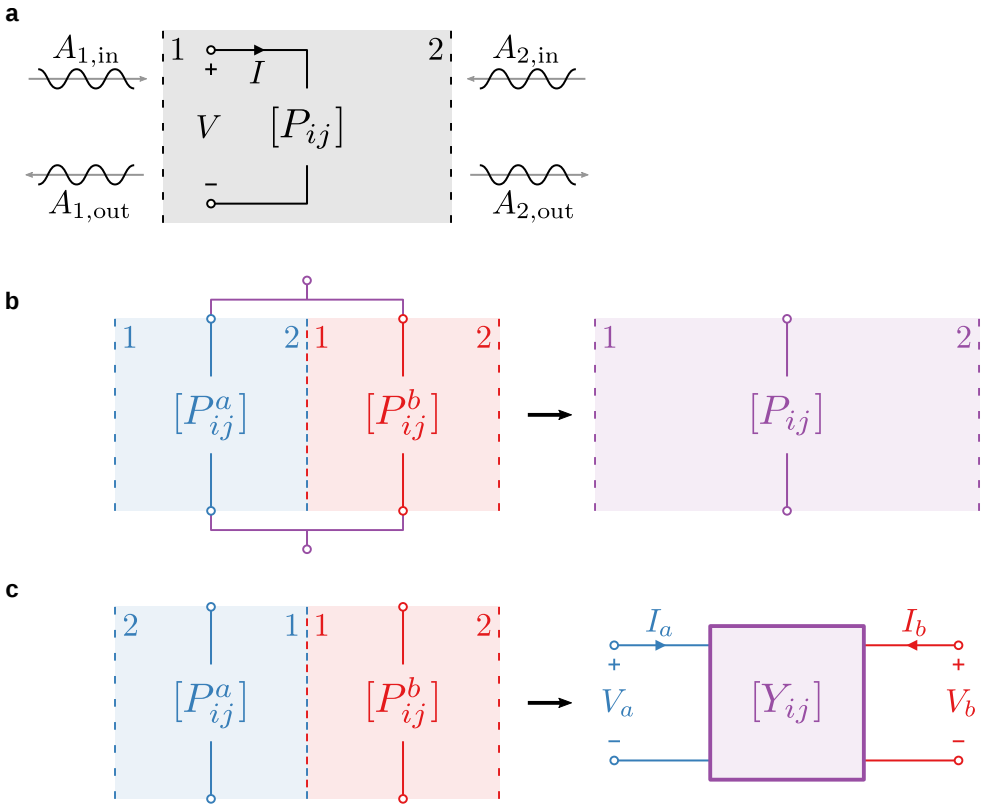

Figure A.1: ***P*-matrix diagrams.** Based on figures from Ref. [66], appendix D. **a,** Illustration of the definition of the P-matrix, relating the current I and voltage V at the electrical port with the ingoing and outgoing surface acoustic waves A at each acoustic port. **b,** Cascading two P-matrices P^a and P^b together into a composite P matrix. Port 2 of a is placed on port 1 of b, and their electrical ports are tied in parallel. **c,** Generating a 2-port microwave network from two P matrices. Port 1 of a is placed on port 1 of b, and we generate the 2-port admittance matrix Y.

transducer ($V = 0$) with an acoustic wave incident on port 1 ($A_{2,\text{in}} = 0$), the induced current in the transducer is $I = P_{31}A_{1,\text{in}}$. On the other hand, for an applied voltage V with no incident acoustic waves ($A_{i,\text{in}} = 0$), we get outgoing acoustic waves $A_{i,\text{out}} = P_{i3}V$.

Due to reciprocity, we have several constraints between the elements:

$$P_{21} = P_{12} \tag{A.2}$$

$$P_{31} = -2P_{13} \tag{A.3}$$

$$P_{32} = -2P_{23}. \tag{A.4}$$

A.2 Device components

A useful SAW device is composed of several different components, such as transducers, open spaces, and mirrors. It is useful to model them separately and combine them to make a full model of a device.

A.2.1 Open space

Open space isn't really considered a component in Ref. [66], but we found it helpful. This is closely analogous to a transmission line as a part of a microwave network. This could be made more complicated by considering the small reflections brought about by loss, but it works very well as it is. Here $P_{21} = P_{12}$ are nonzero, primarily just phase factors, and the other elements are zero. In terms of the wave speed v and length L,

$$P_{21} = \exp[-i\omega L/v]\,. \tag{A.5}$$

A.2.2 Mirror

As discussed in chapter 2, we make acoustic Bragg mirrors out of periodic lines. Each line reflects a small amplitude ($|r| \sim 1\%$). For an acoustic wave with wavelength λ close to the periodicity of the mirror, near-unity reflections occur.

In our simulations, we use the coupling-of-modes model, which is based on the coupling of the left-moving and right-moving acoustic modes inside the grating. This lets us easily use similar models for the transducer and mirrors. The calculations are somewhat involved and beyond the scope of this thesis. For details, see Ref. [66], section 8.2.

The mirror has a frequency range where it works well (fractional bandwidth $\Delta f/f \approx 2|r|/\pi$). In that range, $|P_{11}|$ and $|P_{22}|$ are close to 1, while $|P_{21}|$ and $|P_{12}|$ are small. Outside that range, the situation reverses; the mirror becomes increasingly "transparent." The other elements P_{i3} and P_{3i} are zero.

A.2.3 Transducer

Transducers have the added complication of transduction, so port 3 actually gets involved. We describe a simple case, the symmetric, lossless, non-reflective transducer, as in Ref. [66] chapter 5. In this case, $P_{11} = P_{22} = 0$ and $P_{21} = P_{12} = \exp[-i\omega N\lambda_0/v]$, with N transducer periods and wavelength λ_0. Note that, although $P_{11} = P_{22} = 0$ for this "non-reflective" transducer model, in the presence of an electrical load on transducer's

electrical port, it may still reflect acoustic waves (I gets a contribution from $P_{31}A_{1,\text{in}}$, and $A_{1,\text{out}}$ gets a contribution from $P_{13}V$, where V may be nonzero). The calculations for transduction are also beyond the scope of this thesis, but expressions for the other elements P_{i3} and P_{3i} can be calculated.

As mentioned above, we actually use a more complicated model that allows for internal reflections within the transducer, the coupling-of-modes model.

A.2.4 Loss

We incorporate loss in a simple way by adding an imaginary component to the wavevector k, which equals ω/v in the lossless case. In chapters 2 and 5, we refer to losses η in Np/m. For example, for lossy space, we use

$$P_{21} = \exp[-i(\omega/v - i\eta)L] = \exp[-\eta L]\exp[-i\omega L/v]\,, \tag{A.6}$$

whereby the *amplitude* is multiplied by a factor $\exp[-\eta L]$.

A.3 Composite devices

With 2-port microwave networks, it's easy to cascade networks one after the other using matrix multiplication of their $ABCD$ matrices [75]. We can combine P-matrices in a similar way, although it isn't quite so simple.

A.3.1 1-port admittance

For a device with one transducer (and hence one electrical port), such as a one-port resonator, often all you need to know is its admittance. As discussed above, that is simply P_{33}.

A.3.2 Cascading

We can cascade two P-matrices into one composite P matrix. In this case, we have two devices, a and b, with a's port 2 placed at b's port 1, and their electrical ports tied in parallel. This is shown in Fig. A.1b.

We combine them into a composite device with a P-matrix described by

$$P_{11} = P^a_{11} + P^b_{11}(P^a_{12})^2/D \tag{A.7}$$

$$P_{22} = P^b_{22} + P^a_{22}(P^b_{12})^2/D \tag{A.8}$$

$$P_{12} = P^b_{12}P^a_{12}/D \tag{A.9}$$

$$P_{13} = P^a_{13} + P^a_{12}(P^b_{11}P^a_{23} + P^b_{13})/D \tag{A.10}$$

$$P_{23} = P^b_{23} + P^b_{12}(P^a_{22}P^b_{13} + P^a_{23})/D \tag{A.11}$$

$$P_{33} = P^a_{33} + P^b_{33} - 2P^a_{23}(P^b_{11}P^a_{23} + P^b_{13})/D - 2P^b_{13}(P^a_{22}P^b_{13} + P^a_{23})/D \tag{A.12}$$

$$(D = 1 - P^a_{22}P^b_{11}). \tag{A.13}$$

This is associative but not commutative. We implement these equations in straightforward Python code centered around a class for P-matrices. It is convenient to overload an

operator, such as `__pow__`, to cascade two P-matrix objects, returning a new composite object. In typical use, we make a resonator using separate objects for the mirrors, spaces, and transducer, making a final object as shown below.

```
resonator = mirror ** space ** transducer ** space ** mirror
admittance = resonator.P33
```

A.3.3 2-port devices

Instead of cascading two P-matrices into a composite P-matrix (tying their electrical ports in parallel), we may instead keep the electrical ports separate and calculate the effective 2-port microwave network of the two electrical ports. This is useful for delay lines and filters. It is easiest to calculate the admittance matrix, which can then be converted to other forms, such as an S matrix or $ABCD$ matrix [75].

Consider two devices, a and b, with a's port 1 placed at b's port 1 (different from the cascade case). This is pictured in Fig. A.1c. Now we convert this to an admittance matrix, effectively assuming there are no external incoming acoustic waves. The admittance matrix is defined by

$$\begin{bmatrix} I_a \\ I_b \end{bmatrix} = \begin{bmatrix} Y_{11} & Y_{12} \\ Y_{21} & Y_{22} \end{bmatrix} \begin{bmatrix} V_a \\ V_b \end{bmatrix}. \tag{A.14}$$

We calculate the admittance matrix using

$$Y_{11} = P^a_{33} - 2P^b_{11}(P^a_{13})^2/(1 - P^a_{11}P^b_{11}) \tag{A.15}$$

$$Y_{22} = P^b_{33} - 2P^a_{11}(P^b_{13})^2/(1 - P^a_{11}P^b_{11}) \tag{A.16}$$

$$Y_{12} = Y_{21} = -2P^a_{13}P^b_{13}/(1 - P^a_{11}P^b_{11}). \tag{A.17}$$

For example, to make a symmetric delay line (two transducers separated by some space), we could use code like this, where `cascade_to_Y` implements the above equations. In this example, `half_delay_line` has the space by port 1 and the transducer by port 2.

```
1 half_delay_line = space ** transducer
2 admittance_matrix = half_delay_line.cascade_to_Y(half_delay_line)
```

Devices like this will also have unwanted capacitive coupling between the transducers; this can be manually inserted into the model admittance matrix (consider the equivalent π network) [75]. With careful design, this electrical crosstalk can be minimized. Additionally, since the acoustic waves are much slower than electromagnetic waves, the electrical crosstalk happens on a much faster timescale. This makes it possible to filter it out, either directly in a time domain experiment, or using Fourier analysis in a frequency domain experiment.

Appendix B

Numerical quantum simulation

To understand and analyze the qubit/resonator experiments in Chapter 5, we use a simple numerical model of an open quantum system subject to the Jaynes-Cummings Hamiltonian. This is easy to simulate with the Python library QuTiP [47].

B.1 Physics

B.1.1 Hamiltonian

We capture the essential features of the experiments with a relatively simple model, a 2-level qubit coupled to a 10-level harmonic oscillator in the Jaynes-Cummings model with the rotating wave approximation [40]. In the reference frame rotating at the resonator frequency ω_r, we have the following Hamiltonian [43],

$$H = \hbar\Delta\sigma_+\sigma_- + \hbar g(\sigma_+ a + \sigma_- a^\dagger), \tag{B.1}$$

with detuning $\Delta = \omega_{ge} - \omega_r$, coupling g, qubit lowering operator σ_-, and harmonic oscillator lowering operator a. Using this rotating frame makes the forthcoming numerical integration much faster. Note that the second excited state of the transmon is often important because of the transmon's relatively weak anharmonicity, but here we can ignore it. In this experiment, we can choose Δ and g rather freely.

B.1.2 Master equation

We are modeling an open quantum system [40, 76]; the loss in the resonator is a particularly important effect. For a pure state $|\psi\rangle$ evolving subject to a Hamiltonian H, we integrate the Schrödinger equation,

$$\frac{d}{dt}|\psi\rangle = -\frac{i}{\hbar}H|\psi\rangle. \tag{B.2}$$

To instead calculate the evolution of a (possibly) mixed state ρ, we integrate the Liouville-von Neumann equation,

$$\frac{d}{dt}\rho = -\frac{i}{\hbar}\left[H, \rho\right], \tag{B.3}$$

which is equivalent to the Schrödinger equation for a pure state $\rho = |\psi\rangle\langle\psi|$. Finally, generalizing to an open quantum system, we integrate the Lindblad master equation,

$$\frac{d}{dt}\rho = -\frac{i}{\hbar}\left[H, \rho\right] + \sum_n \left(c_n \rho c_n^\dagger - \frac{1}{2}\left\{c_n^\dagger c_n, \rho\right\}\right), \tag{B.4}$$

where c_n, known as "collapse operators" [47], "Lindblad operators," or "quantum jump operators" [76], allow us to simulate effects like loss and dephasing. In this case, we use $\sigma_-/\sqrt{T_1}$, $\sigma_z/\sqrt{2T_\phi}$, and $a/\sqrt{T_{1r}}$ for qubit decay, qubit dephasing, and resonator decay,

respectively.

B.2 Python implementation

We implement this in Python 2.7.13, NumPy 1.11.3, and QuTiP 4.1.0. Below we list some simple code including the actual values used in Chapter 5. First, we define some parameters and basic operators.

```
t1_q = 20.67e3 # ns
tphi_q = 2.09e3 # ns
thermal_q = 0.017 # thermal population
visibility = 0.97 # readout: Pe_exp = Pe_ideal * visibility

n_levels = 10 # harmonic oscillator levels
t1_r = 148 # ns
thermal_r = 0.005 # thermal population
g = 2*np.pi*0.00732 # 2*pi*GHz

sigma_minus = qutip.tensor(qutip.sigmam(), qutip.identity(n_levels))
sigma_plus = qutip.tensor(qutip.sigmap(), qutip.identity(n_levels))
sigma_x = qutip.tensor(qutip.sigmax(), qutip.identity(n_levels))
sigma_y = qutip.tensor(qutip.sigmay(), qutip.identity(n_levels))
sigma_z = qutip.tensor(qutip.sigmaz(), qutip.identity(n_levels))
a = qutip.tensor(qutip.identity(2), qutip.destroy(n_levels))
```

Here is a simple function that generates a Hamiltonian $H/\hbar$ for a given coupling and detuning, both in units of $2\pi \times$ GHz.

```
def hamiltonian(g, delta):
    H0 = delta*sigma_plus*sigma_minus
    return H0 + g*(sigma_plus*a + sigma_minus*a.dag())
```

Here are some collapse operators for master equation evolution.

```
t1_collapse_q = sigma_minus / numpy.sqrt(t1_q)
tphi_collapse_q = sigma_z / numpy.sqrt(2*tphi_q)
t1_collapse_r = a / numpy.sqrt(t1_r)
collapse = [t1_collapse_q, tphi_collapse_q, t1_collapse_r]
```

Here are initial states, approximate thermal states very close to the ground states.

```
rho_r = qutip.Qobj(numpy.diag([1-thermal_r, thermal_r] +
                              [0]*(n_levels-2)))
rho_q = qutip.Qobj(numpy.diag([thermal_q, 1-thermal_q]))
rho_composite = qutip.tensor(rho_q, rho_r)
```

From here, we perform various operations on the quantum state `rho_composite`. Discrete operations `A` such as π pulses (`sigma_x`) and displacement pulses (built from `qutip.displace`) are executed by transforming `rho` to `A*rho*A.dag()`. These are interleved with master equation evolution (with the coupling and detuning set appropriately). Here is an example using `qutip.mesolve`, evolving `rho` subject to some Hamiltonian `H` and a list of collapse operators `collapse`. This returns a data structure that contains the calculated density matrix at each point in `times`, though it can also return expectation values of operators (listed in the last argument) instead.

```
times = numpy.linspace(0, 1000, 1001) # ns
result = qutip.mesolve(H, rho, times, collapse, [])
```

Appendix C

Wigner tomography

Here we describe some details of the Wigner tomography data analysis discussed in chapter 5. For details about the master equation numerical model, see appendix B.

C.1 Probability distribution fits

In the experiment, we measure the qubit-resonator interaction for different displacements α of the resonator state in resonator phase space, where α is complex valued. For each α value and each resonator state, we record the qubit state after different interaction times with the displaced resonator state. We then use the master equation model to deduce the diagonal elements of the displaced resonator state's density matrix, $\rho'_{nn}(\alpha)$, which constitute a probability distribution $P_n(\alpha)$ (here, $n = 0, 1, \ldots, 9$).

We measure the qubit state prior to the evolution to establish an initial mixed state in the qubit (typical $P_e \approx 0.03$). We use a cost function which takes a candidate distribution

of resonator populations P_n, generates the evolution of P_e predicted by the model, and returns the summed squared error between P_e as predicted by the model and P_e as measured in the experiment. We numerically minimize this function to arrive at a fitted $P_n(\alpha)$. We assess the uncertainty in P_n by numerically calculating the second derivative of the error with respect to each probability in a distribution. The statistical uncertainty in each probability P_n is approximately 0.004.

C.2 Convert Wigner functions to density matrices

We use all of the $P_n(\alpha)$ values to determine the density matrix ρ of each state. We fit to 4×4 density matrices using 15 real parameters (expanding in generalized Gell-Mann matrices [11]). We convert the 4×4 matrices into 10×10 to accommodate the displacement operations. We minimize a cost function which takes 15 real values, converts them into a candidate density matrix ρ, displaces ρ by each experimental α value, and compares the diagonal elements of the displaced ρ to the experimental $P_n(\alpha)$ values. In this case, we directly obtain variance-covariance matrices which establish the uncertainties in each parameter (typically ≈ 0.008, which translates to a similar error in each element of ρ). The fitted density matrices typically have small negative eigenvalues due to noise (≈ -0.02); we truncate these to zero and renormalize the density matrices. Finally, we compute the fidelities by comparing to the ideal pure states $|\psi\rangle$, $F = \sqrt{\langle\psi|\rho|\psi\rangle}$. We estimate the error in the fidelity using Monte Carlo error propagation; the dominant source is from fitting ρ, not $P_n(\alpha)$.

Appendix D

Experimental setup

In this appendix, we document some details of the experimental setup, primarily for the qubit experiments in chapters 3 and 5. This setup is based on Refs. [85, 52], built using custom electronics designed by John Martinis at UCSB.

The cryogenic experiments in chapters 2 and 4 use similar wiring, including magnetic shields, heavy attentuation on the input lines, a cryogenic HEMT amplifier, and (in the case of chapter 4) IR filtering. They use a vector network analyzer with suitable room temperature attenuation and amplification.

Below, we describe each type of signal line. We display a schematic showing each element and filter in Fig. D.1.

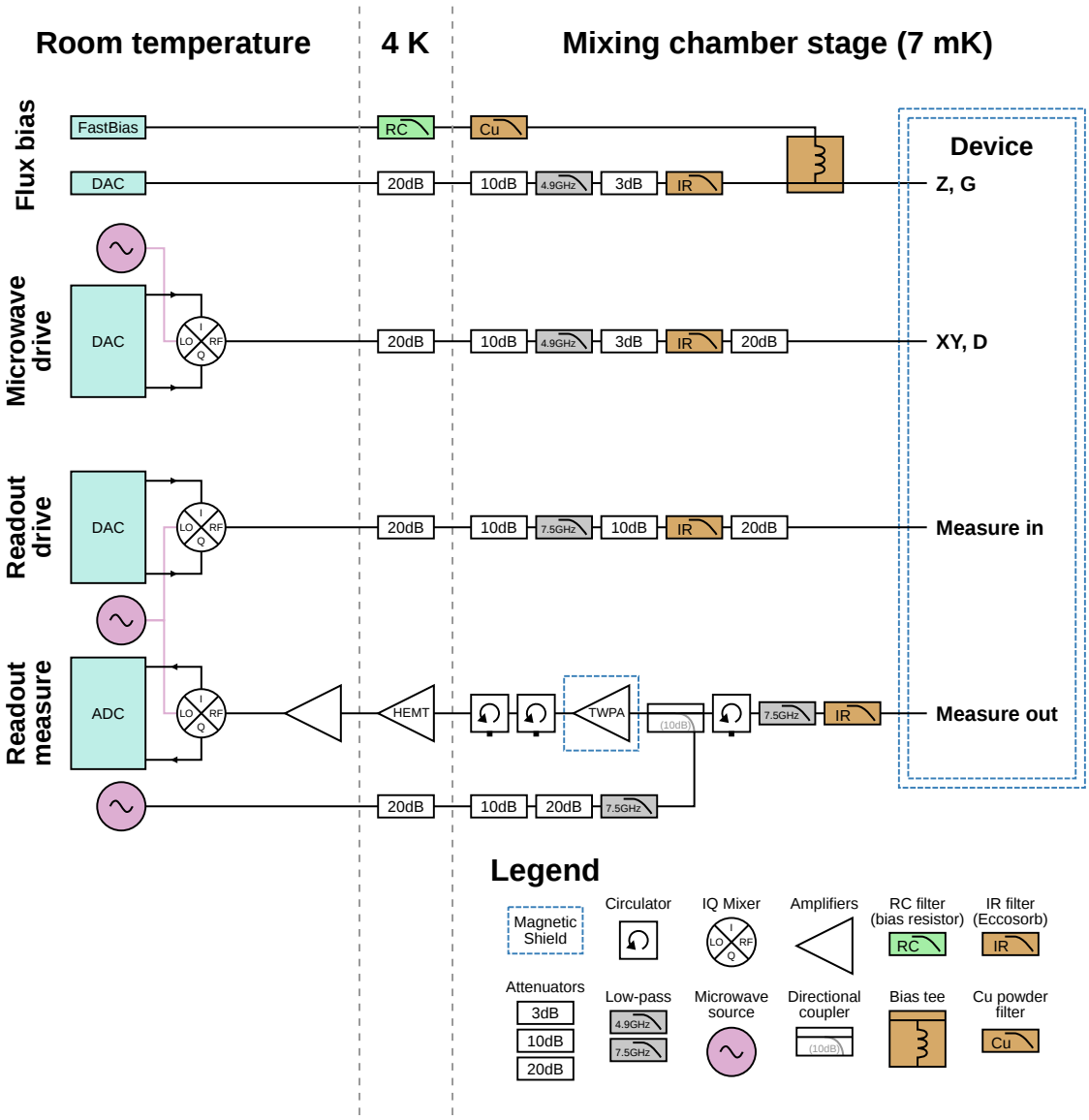

Figure D.1: **Schematic of experimental setup.** Each type of signal line is displayed with the corresponding filters. The temperatures correspond to stages of the dilution refrigerator. These lines have 0 dB attenuators at 50 K and at several stages between 4 K and the mixing chamber stage.

D.1 Flux bias (Z, G)

We separately generate DC signals and pulses; the DC signals are heavily filtered, and the pulses pass through attenuators and filters. They are combined with custom bias tees at the mixing chamber stage.

We generate the qubit Z and coupler G flux pulses using a custom digital to analog converter (DAC) board with 1 Gs/s sampling rate followed by 110 MHz Gaussian filters.

The DC biases for the flux lines are generated by a low-noise voltage source (FastBias card) controlled by a DAC board. The voltage is converted to a current at 4 K with an RC filter acting as a bias resistor, 1.5 kΩ for Z and 0.75 kΩ for G (smaller to compensate for insufficient mutual coupling on our device).

D.2 Microwave pulses (XY, D, readout)

To generate microwave pulses, we use additional custom DAC boards. Each signal line uses two DAC channels, filtered with 240 MHz Gaussian filters, driving the I and Q ports of an IQ mixer to modulate a continuous wave microwave source (local oscillator). They are calibrated to minimize the microwave transmission at the carrier frequency, and typically pulses at slightly different frequencies are generated using sideband modulation. The qubit (XY) and SAW resonator (D) share a microwave source at 3.9 GHz, and the readout microwave source is at 5.3 GHz. The low pass filter at the mixing chamber stage is 4.9 GHz for XY and D and 7.5 GHz for readout.

Not pictured in Fig. D.1, the D line also has a circulator to allow reflection measurements, with the reflected output going through another circulator to a cryogenic HEMT amplifier. We do not employ this functionality in this thesis.

D.3 Output signal chain

The output from the readout network is first amplified by a traveling wave parametric amplifier (TWPA) [60] (MIT Lincoln Laboratory) in a magnetic shield at the mixing chamber stage. It uses a microwave pump at 5.98 GHz, generated by a separate microwave source. This is added to the TWPA input using a -10 dB directional coupler. The TWPA output is amplified by a cryogenic HEMT amplifier (Low Noise Factory).

After one room temperature amplifier (Miteq AFS3), the pump signal is large enough to saturate a second amplifier. We filter out the pump using a custom dissipative notch filter tuned to pass the readout signal at 5.38 GHz and reject the pump signal. This is just some carefully-assembled SMA adapters and attenuators. We then amplify the signal again (Miteq AFS3). This signal is demodulated using the same local oscillator used to generate the readout pulses. The demodulated signals I and Q are read by a custom analog to digital converter (ADC) board with 1 Gs/s sampling rate. These signals are integrated over time (a few hundred ns) to generate the readout amplitude $I + iQ$.

Appendix E

Fabrication

In this appendix, we describe the fabrication techniques used to make the devices in chapters 2, 4, and 5. All of this fabrication took place at the Pritzker Nanofabrication Facility at the University of Chicago. Remember to think clean thoughts.

E.1 Surface acoustic wave devices

Completed devices are shown in Fig. E.1.

E.1.1 Substrate

All of the surface acoustic wave devices discussed in this thesis are fabricated on lithium niobate substrates. We use crystal cut 128°Y-X and chemically reduced ("black") wafers [89]. The chemically reduced wafers have bad optical properties, but they work well for SAW devices and make fabrication much easier:

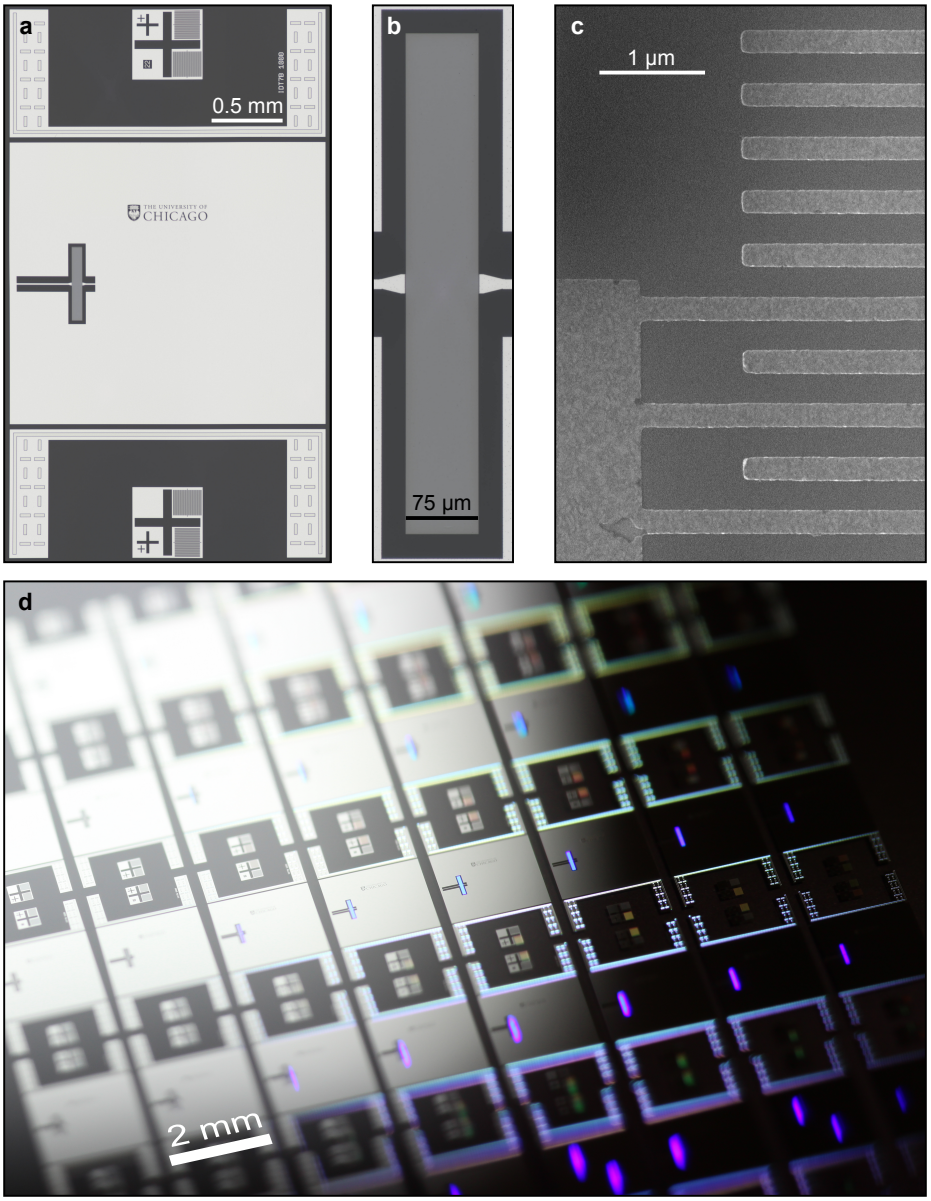

Figure E.1: **Completed surface acoustic wave resonators. a,** Optical micrograph of a completed chip of the same design as the one used in chapter 5. The upper and lower regions contain the alignment marks, SU-8 pattern, and space for glue. **b,** Optical micrograph of the chip in **a**, zoomed in on the surface acoustic wave resonator. The transducer, center, has short coplanar waveguides connected to each side. **c,** Scanning electron micrograph showing the transducer and mirror (the exact device used in chapter 5). **d,** Photograph of the array of resonators designed for flip-chip coupling, prior to dicing. The SU-8 is visible as white highlights, especially in the right half of the image.

- They do not stick to hot plates due to thermally-induced polarization.
- They do not exhibit violent electrostatic discharge between patterned electrodes when heated.
- They are easier to image in an SEM.

Lithium niobate is much more brittle than silicon or sapphire, so care must be taken to avoid shattering the sample. Avoid accidentally chipping the edges. When placing a sample on a hot plate above 115 °C, first place it on a 115 °C hot plate for 30 s to avoid thermal shock.

E.1.2 Metal pattern

For 4 GHz devices, the wavelength λ is 1 µm, necessitating 250 nm wide metal lines and spaces. We create those patterns with electron-beam lithography. We use a liftoff process to avoid roughening the substrate surface with an etch process.[1] In this case, we use a poly(methyl methacrylate) (PMMA) bilayer to attempt to achieve an undercut, but a single PMMA layer should also work. We define the entire metal pattern in one layer, including ground planes and coupling circuitry.

PMMA application

1. Sonicate in acetone and isopropyl alcohol (IPA) and rinse with deionized (DI) water.

[1] We also made 700 MHz devices using photolithography and inductively coupled plasma etching (see qubit process below). The devices worked very well, but we observed the etch roughened the underlying lithium niobate surface. We measured (with atomic force microscopy) root-mean-square roughness 0.2 nm before processing and 0.5 nm after the etch.

2. Heat on 115 °C hot plate for 10 minutes.
3. Spin on PMMA 495K A4 (5000 rpm, 45 s) (150 nm).
4. Heat on 180 °C hot plate for 5 minutes.
5. Spin on PMMA 950K A2 (1500 rpm, 45 s) (100 nm).
6. Heat on 180 °C hot plate for 5 minutes.
7. Thermally evaporate gold conduction layer (10 nm, 0.05 nm/s).

Exposure

We expose using a Raith EBPG5000 Plus at 100 kV. We write fine features at 5 nA to 15 nA and coarse features (such as inductors, ground planes, and alignment marks) at 100 nA to 150 nA. A typical dose is 400 $\mu C/cm^2$, where writing a $(2\,mm)^2$ ground plane takes around 2 minutes. It is critical to use proximity effect correction; we use GenISys BEAMER and TRACER.

Development

1. Remove gold with Gold Etchant TFA (Transene) (10 s) and rinse with DI water.
2. Develop in mixture of 1 part IPA, 1 part methyl isobutyl ketone (MIBK), 60 s.
3. Rinse in IPA, 60 s.

Metalization

The transducers, mirrors, and circuitry are all defined by patterned aluminum, a familiar and friendly superconductor. We use electron-beam evaporation to deposit the aluminum,

typically at 1×10^{-7} mbar and 0.2 nm/s. Immediately before loading in the evaporator, we perform a downstream oxygen clean which etches ≈10 nm PMMA to remove resist residue. Deposit at normal incidence without sample rotation.

Liftoff

We use an overnight (12 hours) liftoff in acetone, although heated N-methyl-2-pyrrolidone (NMP) should also work. It proved helpful to do liftoff with the sample suspended face-down, and (with the sample in a clean acetone solution and with all of the visible extraneous aluminum gone) to use sonication. We then rinse with IPA and DI water. To remove PMMA residue from the metal lines, we perform another downstream oxygen clean.

E.1.3 Flip-chip spacers

For flip-chip devices, we pattern the SU-8 spacers on the lithium niobate devices following the metal pattern (see below), prior to dicing.

E.2 Qubits and coplanar waveguide resonators

We fabricate the qubit and coplanar waveguide resonator devices on double side polished c-axis sapphire. We first coat the substrate in a blanket aluminum film and then etch a pattern into the aluminum with photolithography and inductively coupled plasma (ICP) etching. The qubit devices have several additional liftoff steps to define crossovers,

alignment marks, Josephson junctions, and bandages. These processes are adapted from refs. [28, 52]. The qubit process is illustrated in Fig. E.2.

E.2.1 Base metal pattern

1. Sonicate in acetone and IPA and rinse with DI water.
2. Heat on 200 °C hot plate for 10 minutes.
3. Deposit 100 nm aluminum (1×10^{-7} mbar, 0.2 nm/s).
4. Photolithography (AZ MiR 703).
5. ICP etch the aluminum ($Cl_2/BCl_3/Ar$).
6. Soak in DI water for 10 minutes to passivate residual Cl.
7. Downstream oxygen clean, etching ≈0.1 µm photoresist.
8. Sonicate in 80 °C NMP and rinse with IPA and DI water.

Aluminum etch

We etch the aluminum in an Advanced Vacuum / PlasmaTherm Apex ICP etcher with the following parameters. The larger exposed areas (easily visible to the naked eye) visibly clear in about 12 s.

ICP Power	400 W
Bias Power	33 W
Pressure	5 mTorr
Cl_2 Flow	30 sccm
BCl_3 Flow	30 sccm
Ar Flow	10 sccm
Time	24 s

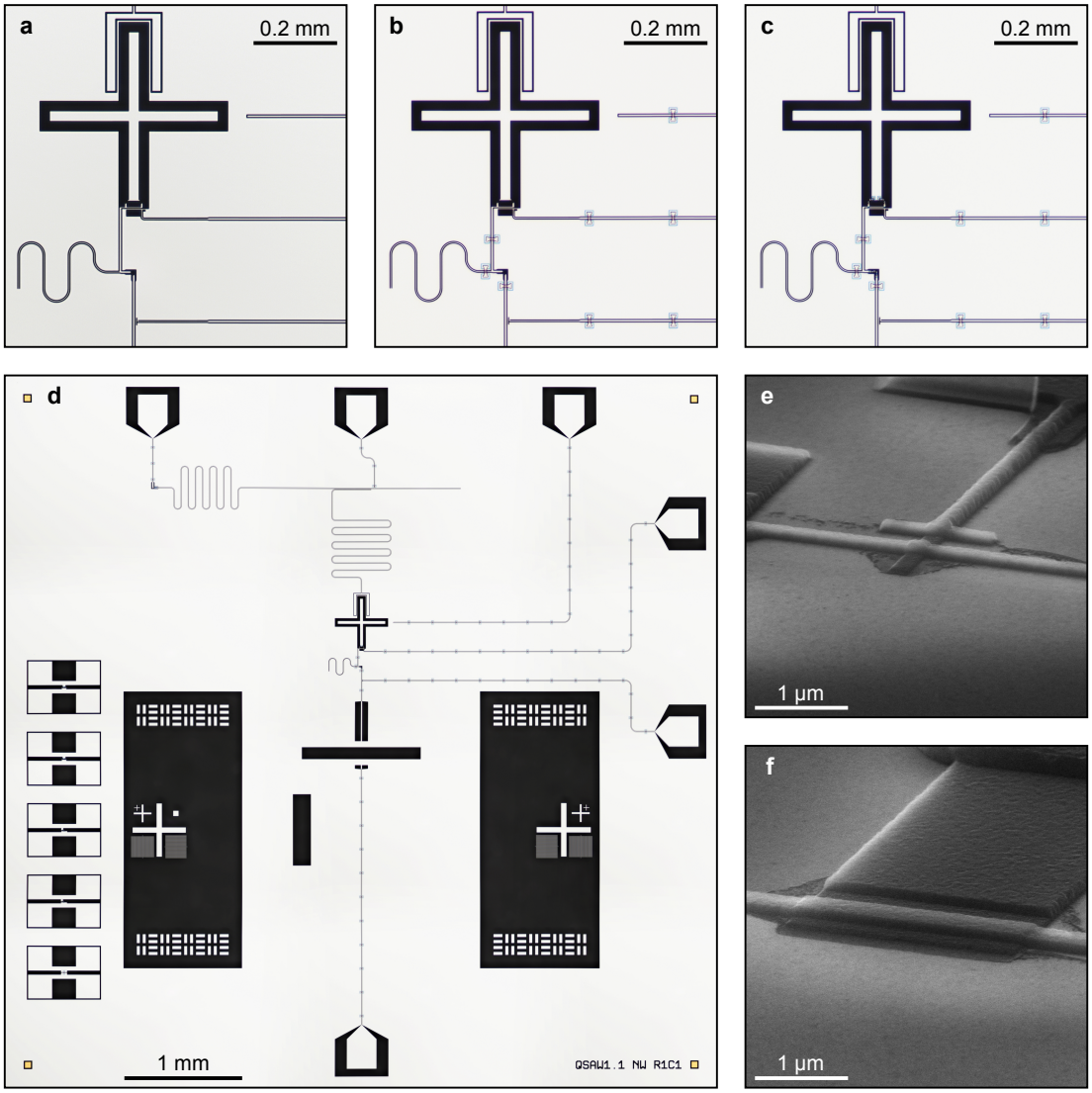

Figure E.2: **Qubit fabrication. a-c,** Optical micrographs summarizing the qubit fabrication process. **a,** The base aluminum is patterned. **b,** The SiO_2/aluminum crossovers are complete. **c,** The junctions and bandages are complete. **d,** Composite optical micrograph of a full complete die. **e-f,** Scanning electron micrographs (perspective view) of fabricated Josephson junctions. **e,** Typical qubit junction. **f,** Typical coupler junction.

E.2.2 Crossovers and alignment marks

For the qubit devices, we follow the base metal pattern with several liftoff layers. Each photolithography layer uses AZ MiR 703 resist for simple "tear"-style liftoff. Each deposition uses electron beam evaporation at about 1×10^{-7} mbar. Each liftoff step (including the Josephson junctions) uses the same NMP process (see below).

1. SiO_2 for crossover dielectric (200 nm, 0.3 nm/s).
2. Al for crossover metal (230 nm, 1 nm/s), preceded by in situ Ar ion mill.
3. Ti+Au for alignment marks (10 nm at 0.1 nm/s and 150 nm at 0.2 nm/s).
4. Josephson junctions (see below), not preceded by in situ Ar ion mill.
5. Al for bandages (200 nm, 1 nm/s), establishing galvanic connections between the base metal and the junction metal, preceded by in situ Ar ion mill.

E.2.3 Josephson junctions

This process is adapted quite directly from ref. [52]; see more details there. In this process, we create a freestanding bridge [27] of PMMA using a bilayer of PMMA on methacrylic acid (MAA) copolymer. In our case, we observed a more reliable process when we use the "bandage" technique [28] instead of ion milling the Dolan bridge PMMA pattern. We use the same process to make the qubit and coupler junctions simultaneously.

PMMA application

1. Sonicate in acetone and IPA.

2. Heat on 115 °C hot plate for 10 minutes.
3. Spin on MAA EL9 (1500 rpm, 45 s) (500 nm).
4. Heat on 160 °C hot plate for 10 minutes.
5. Spin on PMMA 950K A4 (2000 rpm, 40 s) (300 nm).
6. Heat on 160 °C hot plate for 10 minutes.
7. Thermally evaporate gold conduction layer (10 nm, 0.05 nm/s).

Exposure

We expose using a Raith EBPG5000 Plus at 100 kV and 1 nA. We use a dose of 2000 µC/cm^2 for contact pads, 1850 µC/cm^2 for removing PMMA and MAA, and 350 µC/cm^2 for removing MAA only (for undercuts). We do not use proximity effect correction.

Development

1. Remove gold with Gold Etchant TFA (Transene) (10 s) and rinse with DI water.
2. Develop in mixture of 3 part IPA, 1 part MIBK, 40 s.
3. Rinse in IPA, 10 s.

Metalization

1. Downstream oxygen clean (etching ≈10 nm PMMA).
2. Pump in evaporator load lock for 12 hours.
3. Deposit 65 nm aluminum (1×10^{-7} mbar, 1 nm/s, 60° tilt).
4. Oxidize at 30 mbar (15% O_2 in Ar) for 50 minutes.

5. Deposit 100 nm aluminum (1×10^{-7} mbar, 1 nm/s, normal incidence).

E.2.4 Repeated processes

We list these procedures with optional DI water rinses. Skip those rinses if the sample has both gold and aluminum exposed to avoid electrochemical reactions.

Photoresist pattern

We use this standard process to pattern AZ MiR 703 positive i-line photoresist for both the etch and "tear" liftoff processes used above. We use a Heidelberg MLA150 maskless aligner at 375 nm with a typical exposure of 100 mJ/cm^2 to 200 mJ/cm^2 depending on the underlying materials.

1. Sonicate in acetone and IPA and rinse with DI water.
2. Heat on 115 °C hot plate for 10 minutes.
3. Spin AZ MiR 703 (4500 rpm, 30 s) (900 nm).
4. Heat on 90 °C hot plate for 1 minute.
5. Expose pattern.
6. Heat on 115 °C hot plate for 1 minute.
7. Develop in AZ 300 MIF, 1 minute.
8. Rinse in DI water.

If the pattern is for liftoff, we perform a downstream oxygen clean, etching ≈100 nm photoresist, immediately prior to deposition.

Liftoff

This is for both the photoresist "tear" liftoff and the PMMA junction liftoff. Preheat the NMP solutions and use a heated water bath rather than a hot plate. We suspend the sample face-down and do not use sonication.

1. Soak in 80 °C NMP, 3 hours.
2. Spray with NMP to remove most of the film/resist (≈30 s).
3. Soak in new 80 °C NMP, 1 hour.
4. Rinse in IPA, then DI water.

Flip-chip spacers (SU-8)

This process creates robust, solvent-resistant epoxy spacers using negative SU-8 photoresist. Once cured, it is very difficult to remove. Our spacers are 6.5 µm thick.

1. Sonicate in acetone and IPA and rinse with DI water.
2. Heat on 115 °C hot plate for 10 minutes.
3. Spin SU-8 3005 (300 rpm, 10 s, then immediately 4000 rpm, 45 s).
4. Heat on hot plate: 65 °C for 30 s, then immediately 95 °C for 2 minutes.
5. Expose pattern (375 nm, 500 mJ/cm^2).
6. Heat on hot plate: 65 °C for 30 s, then immediately 95 °C for 2 minutes.
7. Develop in SU-8 developer, 90 s.
8. Rinse in new SU-8 developer, 30 s, then IPA, 30 s.
9. Downstream oxygen clean (etching ≈100 nm photoresist).

10. Heat on 160 °C hot plate for 5 minutes to cure.

Bibliography

[1] O. Arcizet, V. Jacques, A. Siria, P. Poncharal, P. Vincent, and S. Seidelin. A single nitrogen-vacancy defect coupled to a nanomechanical oscillator. *Nature Physics*, 7(11):879–883, 2011.

[2] T. Aref, M. Ekström, M. Gustafsson, A. Kockum, A. Ask, G. Johansson, and P. Delsing. Observation of lamb shift in an artificial atom caused by coupling to the phonon vacuum. In *APS Meeting Abstracts*, 2017.

[3] Thomas Aref, Per Delsing, Maria K. Ekstrm, Anton Frisk Kockum, Martin V. Gustafsson, Gran Johansson, Peter J. Leek, Einar Magnusson, and Riccardo Manenti. Quantum acoustics with surface acoustic waves. In *Quantum Science and Technology*, pages 217–244. Springer International Publishing, 2016.

[4] Markus Aspelmeyer, Tobias J. Kippenberg, and Florian Marquardt. Cavity optomechanics. *Reviews of Modern Physics*, 86(4):1391–1452, 2014.

[5] K. Banaszek, C. Radzewicz, K. Wódkiewicz, and J. S. Krasiński. Direct measurement of the Wigner function by photon counting. *Physical Review A*, 60(1):674–677, 1999.

[6] J. Bardeen, L. N. Cooper, and J. R. Schrieffer. Theory of superconductivity. *Physical Review*, 108(5):1175–1204, 1957.

[7] R. Barends, J. Kelly, A. Megrant, D. Sank, E. Jeffrey, Y. Chen, Y. Yin, B. Chiaro, J. Mutus, C. Neill, P. O'Malley, P. Roushan, J. Wenner, T. C. White, A. N. Cleland, and John M. Martinis. Coherent Josephson qubit suitable for scalable quantum integrated circuits. *Physical Review Letters*, 111(8), 2013.

[8] R. Barends, J. Kelly, A. Megrant, A. Veitia, D. Sank, E. Jeffrey, T. C. White, J. Mutus, A. G. Fowler, B. Campbell, Y. Chen, Z. Chen, B. Chiaro, A. Dunsworth, C. Neill, P. O'Malley, P. Roushan, A. Vainsencher, J. Wenner, A. N. Korotkov, A. N. Cleland, and John M. Martinis. Superconducting quantum circuits at the surface code threshold for fault tolerance. *Nature*, 508(7497):500–503, 2014.

[9] R. Barends, J. Wenner, M. Lenander, Y. Chen, R. C. Bialczak, J. Kelly, E. Lucero, P. O'Malley, M. Mariantoni, D. Sank, H. Wang, T. C. White, Y. Yin, J. Zhao, A. N. Cleland, John M. Martinis, and J. J. A. Baselmans. Minimizing quasiparticle generation from stray infrared light in superconducting quantum circuits. *Applied Physics Letters*, 99(11):113507, 2011.

[10] P. Bertet, A. Auffeves, P. Maioli, S. Osnaghi, T. Meunier, M. Brune, J. M. Raimond, and S. Haroche. Direct measurement of the Wigner function of a one-photon fock state in a cavity. *Physical Review Letters*, 89(20), 2002.

[11] Reinhold A. Bertlmann and Philipp Krammer. Bloch vectors for qudits. *Journal of Physics A: Mathematical and Theoretical*, 41(23):235303, 2008.

[12] Joerg Bochmann, Amit Vainsencher, David D. Awschalom, and Andrew N. Cleland. Nanomechanical coupling between microwave and optical photons. *Nature Physics*, 9(11):712–716, 2013.

[13] Niels Bohr. Über die serienspektra der elemente. *Zeitschrift für Physik*, 2(5):423–469, 1920.

[14] G. Bu, D. Ciplys, M. Shur, L. J. Schowalter, S. Schujman, and R. Gaska. Electromechanical coupling coefficient for surface acoustic waves in single-crystal bulk aluminum nitride. *Applied Physics Letters*, 84(23):4611–4613, 2004.

[15] S. Butterworth. On electrically-maintained vibrations. *Proceedings of the Physical Society of London*, 27:410–424, 1915.

[16] Jasper Chan, T. P. Mayer Alegre, Amir H. Safavi-Naeini, Jeff T. Hill, Alex Krause, Simon Grblacher, Markus Aspelmeyer, and Oskar Painter. Laser cooling of a nanomechanical oscillator into its quantum ground state. *Nature*, 478(7367):89–92, 2011.

[17] Yu Chen, C. Neill, P. Roushan, N. Leung, M. Fang, R. Barends, J. Kelly, B. Campbell, Z. Chen, B. Chiaro, A. Dunsworth, E. Jeffrey, A. Megrant, J. Y. Mutus, P. J. J. O'Malley, C. M. Quintana, D. Sank, A. Vainsencher, J. Wenner, T. C. White, Michael R. Geller, A. N. Cleland, and John M. Martinis. Qubit architecture with high coherence and fast tunable coupling. *Physical Review Letters*, 113(22), 2014.

[18] Zijun Chen. *Metrology of Quantum Control and Measurement in Superconducting Qubits*. PhD thesis, University of California Santa Barbara, 2017.

[19] Zijun Chen, Julian Kelly, Chris Quintana, R. Barends, B. Campbell, Yu Chen, B. Chiaro, A. Dunsworth, A. G. Fowler, E. Lucero, E. Jeffrey, A. Megrant, J. Mutus, M. Neeley, C. Neill, P. J. J. O'Malley, P. Roushan, D. Sank, A. Vainsencher, J. Wenner, T. C. White, A. N. Korotkov, and John M. Martinis. Measuring and suppressing quantum state leakage in a superconducting qubit. *Physical Review Letters*, 116(2), 2016.

[20] Yiwen Chu, Prashanta Kharel, William H. Renninger, Luke D. Burkhart, Luigi Frunzio, Peter T. Rakich, and Robert J. Schoelkopf. Quantum acoustics with superconducting qubits. *Science*, 358(6360):199–202, 2017.

[21] Yiwen Chu, Prashanta Kharel, Taekwan Yoon, Luigi Frunzio, Peter Rakich, and Robert Schoelkopf. Climbing the phonon Fock state ladder. *Submitted*, 2018.

[22] A. N. Cleland and M. R. Geller. Superconducting qubit storage and entanglement with nanomechanical resonators. *Physical Review Letters*, 93(7), 2004.

[23] Andrew N. Cleland. *Foundations of Nanomechanics*. Springer, 2003.

[24] Jacques Curie and Pierre Curie. Développement par compression de l'électricité polaire dans les cristaux hémièdres à faces inclinées. *Bulletin de la Société minérologique de France*, 3:90–93, 1880.

[25] P. Debye. Zur theorie der spezifischen wärmen. *Annalen der Physik*, 344(14):789–839, 1912.

[26] Michel H. Devoret and John M. Martinis. Implementing qubits with superconducting integrated circuits. In *Experimental aspects of quantum computing*, pages 163–203. Springer, 2005.

[27] G. J. Dolan. Offset masks for lift-off photoprocessing. *Applied Physics Letters*, 31(5):337–339, 1977.

[28] A. Dunsworth, A. Megrant, C. Quintana, Zijun Chen, R. Barends, B. Burkett, B. Foxen, Yu Chen, B. Chiaro, A. Fowler, R. Graff, E. Jeffrey, J. Kelly, E. Lucero, J. Y. Mutus, M. Neeley, C. Neill, P. Roushan, D. Sank, A. Vainsencher, J. Wenner, T. C. White, and John M. Martinis. Characterization and reduction of capacitive loss induced by sub-micron Josephson junction fabrication in superconducting qubits. *Applied Physics Letters*, 111(2):022601, 2017.

[29] K. S. Van Dyke. The electric network equivalent of a piezoelectric resonator. *Physical Review*, 25(6):895, 1925.

[30] Y. Ebata. Suppression of bulk-scattering loss in SAW resonator with quasi-constant acoustic reflection periodicity. In *IEEE Ultrasonics Symposium Proceedings*. IEEE, 1988.

[31] A. Einstein. Die plancksche theorie der strahlung und die theorie der spezifischen wärme. *Annalen der Physik*, 327(1):180–190, 1907.

[32] V. V. Felmetsger, P. N. Laptev, and S. M. Tanner. Innovative technique for tailoring intrinsic stress in reactively sputtered piezoelectric aluminum nitride films. *Journal of Vacuum Science & Technology A: Vacuum, Surfaces, and Films*, 27(3):417–422, 2009.

[33] B. Foxen, J. Y. Mutus, E. Lucero, R. Graff, A. Megrant, Yu Chen, C. Quintana, B. Burkett, J. Kelly, E. Jeffrey, Yan Yang, Anthony Yu, K. Arya, R. Barends, Zijun Chen, B. Chiaro, A. Dunsworth, A. Fowler, C. Gidney, M. Giustina, T. Huang, P. Klimov, M. Neeley, C. Neill, P. Roushan, D. Sank, A. Vainsencher, J. Wenner, T. C. White, and John M. Martinis. Qubit compatible superconducting interconnects. *Quantum Science and Technology*, 3(1):014005, 2017.

[34] K. Geerlings, Z. Leghtas, I. M. Pop, S. Shankar, L. Frunzio, R. J. Schoelkopf, M. Mirrahimi, and M. H. Devoret. Demonstrating a driven reset protocol for a superconducting qubit. *Physical Review Letters*, 110(12), 2013.

[35] Michael R. Geller, Emmanuel Donate, Yu Chen, Michael T. Fang, Nelson Leung, Charles Neill, Pedram Roushan, and John M. Martinis. Tunable coupler for superconducting Xmon qubits: Perturbative nonlinear model. *Physical Review A*, 92(1), 2015.

[36] Herbert Goldstein, Charles P. Poole Jr., and John L. Safko. *Classical Mechanics*. Pearson, 2001.

[37] Maxim Goryachev, Daniel L. Creedon, Eugene N. Ivanov, Serge Galliou, Roger Bourquin, and Michael E. Tobar. Extremely low-loss acoustic phonons in a quartz bulk acoustic wave resonator at millikelvin temperature. *Applied Physics Letters*, 100(24):243504, 2012.

[38] M. V. Gustafsson, T. Aref, A. F. Kockum, M. K. Ekstrom, G. Johansson, and P. Delsing. Propagating phonons coupled to an artificial atom. *Science*, 346(6206):207–211, 2014.

[39] M. V. Gustafsson, P. V. Santos, G. Johansson, and P. Delsing. Local probing of propagating acoustic waves in a gigahertz echo chamber. *Nature Physics*, 8(4):338–343, 2012.

[40] Serge Haroche and Jean-Michel Raimond. *Exploring the quantum: Atoms, cavities, and photons*. Oxford University Press, 2006.

[41] K. Hashimoto, T. Omori, and M. Yamaguchi. Design considerations on surface acoustic wave resonators with significant internal reflection in interdigital transducers. *IEEE Transactions on Ultrasonics, Ferroelectrics and Frequency Control*, 51(11):1394–1403, 2004.

[42] Ken-ya Hashimoto. *Surface Acoustic Wave Devices in Telecommunications*. Springer, 2000.

[43] Max Hofheinz, H. Wang, M. Ansmann, Radoslaw C. Bialczak, Erik Lucero, M. Neeley, A. D. O'Connell, D. Sank, J. Wenner, John M. Martinis, and A. N. Cleland. Synthesizing arbitrary quantum states in a superconducting resonator. *Nature*, 459(7246):546–549, 2009.

[44] E. T. Jaynes and F. W. Cummings. Comparison of quantum and semiclassical radiation theories with application to the beam maser. *Proceedings of the IEEE*, 51(1):89–109, 1963.

[45] Evan Jeffrey, Daniel Sank, J. Y. Mutus, T. C. White, J. Kelly, R. Barends, Y. Chen, Z. Chen, B. Chiaro, A. Dunsworth, A. Megrant, P. J. J. O'Malley, C. Neill, P. Roushan, A. Vainsencher, J. Wenner, A. N. Cleland, and John M. Martinis. Fast accurate state measurement with superconducting qubits. *Physical Review Letters*, 112(19), 2014.

[46] X. Y. Jin, A. Kamal, A. P. Sears, T. Gudmundsen, D. Hover, J. Miloshi, R. Slattery, F. Yan, J. Yoder, T. P. Orlando, S. Gustavsson, and W. D. Oliver. Thermal and residual excited-state population in a 3d transmon qubit. *Phys. Rev. Lett.*, 114:240501, 2015.

[47] J. R. Johansson, P. D. Nation, and Franco Nori. QuTiP: An open-source python framework for the dynamics of open quantum systems. *Computer Physics Communications*, 183(8):1760–1772, 2012.

[48] B. D. Josephson. Possible new effects in superconductive tunnelling. *Physics Letters*, 1(7):251–253, 1962.

[49] B. D. Josephson. The discovery of tunnelling supercurrents. *Reviews of Modern Physics*, 46(2):251–254, 1974.

[50] Dvir Kafri, Chris Quintana, Yu Chen, Alireza Shabani, John M. Martinis, and Hartmut Neven. Tunable inductive coupling of superconducting qubits in the strongly nonlinear regime. *Physical Review A*, 95(5), 2017.

[51] J. Kelly, R. Barends, A. G. Fowler, A. Megrant, E. Jeffrey, T. C. White, D. Sank, J. Y. Mutus, B. Campbell, Yu Chen, Z. Chen, B. Chiaro, A. Dunsworth, I.-C. Hoi, C. Neill, P. J. J. O'Malley, C. Quintana, P. Roushan, A. Vainsencher, J. Wenner, A. N. Cleland, and John M. Martinis. State preservation by repetitive error detection in a superconducting quantum circuit. *Nature*, 519(7541):66–69, 2015.

[52] Julian S. Kelly. *Fault-tolerant superconducting qubits*. PhD thesis, University of California Santa Barbara, 2015.

[53] Charles Kittel. *Introduction to Solid State Physics*. Wiley, 2004.

[54] Jens Koch, Terri M. Yu, Jay Gambetta, A. A. Houck, D. I. Schuster, J. Majer, Alexandre Blais, M. H. Devoret, S. M. Girvin, and R. J. Schoelkopf. Charge-insensitive qubit design derived from the Cooper pair box. *Physical Review A*, 76(4), 2007.

[55] S. Kolkowitz, A. C. Bleszynski Jayich, Q. P. Unterreithmeier, S. D. Bennett, P. Rabl, J. G. E. Harris, and M. D. Lukin. Coherent sensing of a mechanical resonator with a single-spin qubit. *Science*, 335(6076):1603–1606, 2012.

[56] Gershon Kurizki, Patrice Bertet, Yuimaru Kubo, Klaus Mølmer, David Petrosyan, Peter Rabl, and Jrg Schmiedmayer. Quantum technologies with hybrid systems. *Proceedings of the National Academy of Sciences*, 112(13):3866–3873, 2015.

[57] John H. Lau, editor. *Flip Chip Technologies*. McGraw-Hill, 1996.

[58] C. K. Law and J. H. Eberly. Arbitrary control of a quantum electromagnetic field. *Physical Review Letters*, 76(7):1055–1058, 1996.

[59] Kenneth W. Lee, Donghun Lee, Preeti Ovartchaiyapong, Joaquin Minguzzi, Jero R. Maze, and Ania C. Bleszynski Jayich. Strain coupling of a mechanical resonator to a single quantum emitter in diamond. *Physical Review Applied*, 6(3), 2016.

[60] C. Macklin, K. O'Brien, D. Hover, M. E. Schwartz, V. Bolkhovsky, X. Zhang, W. D. Oliver, and I. Siddiqi. A near-quantum-limited Josephson traveling-wave parametric amplifier. *Science*, 350(6258):307–310, 2015.

[61] R. Manenti, M. J. Peterer, A. Nersisyan, E. B. Magnusson, A. Patterson, and P. J. Leek. Surface acoustic wave resonators in the quantum regime. *Physical Review B*, 93(4), 2016.

[62] Riccardo Manenti, Anton F. Kockum, Andrew Patterson, Tanja Behrle, Joseph Rahamim, Giovanna Tancredi, Franco Nori, and Peter J. Leek. Circuit quantum acoustodynamics with surface acoustic waves. *Nature Communications*, 8(1), 2017.

[63] Benjamin A. Mazin. *Microwave Kinetic Inductance Detectors*. PhD thesis, California Institute of Technology, 2004.

[64] A. Megrant, C. Neill, R. Barends, B. Chiaro, Yu Chen, L. Feigl, J. Kelly, Erik Lucero, Matteo Mariantoni, P. J. J. O'Malley, D. Sank, A. Vainsencher, J. Wenner, T. C. White, Y. Yin, J. Zhao, C. J. Palmstrøm, John M. Martinis, and A. N. Cleland. Planar superconducting resonators with internal quality factors above one million. *Applied Physics Letters*, 100(11):113510, 2012.

[65] Bradley A. Moores, Lucas R. Sletten, Jeremie J. Viennot, and K. W. Lehnert. Cavity quantum acoustic device in the multimode strong coupling regime. *Physical Review Letters*, 120(22), 2018.

[66] David Morgan. *Surface Acoustic Wave Filters*. Elsevier, 2007.

[67] C. Neill, P. Roushan, M. Fang, Y. Chen, M. Kolodrubetz, Z. Chen, A. Megrant, R. Barends, B. Campbell, B. Chiaro, A. Dunsworth, E. Jeffrey, J. Kelly, J. Mutus,

P. J. J. O'Malley, C. Quintana, D. Sank, A. Vainsencher, J. Wenner, T. C. White, A. Polkovnikov, and J. M. Martinis. Ergodic dynamics and thermalization in an isolated quantum system. *Nature Physics*, 12(11):1037–1041, 2016.

[68] Charles J. Neill. *A path towards quantum supremacy with superconducting qubits*. PhD thesis, University of California Santa Barbara, 2017.

[69] A. D. O'Connell, M. Ansmann, R. C. Bialczak, M. Hofheinz, N. Katz, Erik Lucero, C. McKenney, M. Neeley, H. Wang, E. M. Weig, A. N. Cleland, and John M. Martinis. Microwave dielectric loss at single photon energies and millikelvin temperatures. *Applied Physics Letters*, 92(11):112903, 2008.

[70] A. D. O'Connell, M. Hofheinz, M. Ansmann, Radoslaw C. Bialczak, M. Lenander, Erik Lucero, M. Neeley, D. Sank, H. Wang, M. Weides, J. Wenner, John M. Martinis, and A. N. Cleland. Quantum ground state and single-phonon control of a mechanical resonator. *Nature*, 464(7289):697–703, 2010.

[71] Aaron D. O'Connell. *A Macroscopic Mechanical Resonator Operated in the Quantum Limit*. PhD thesis, University of California Santa Barbara, 2010.

[72] R. K. Pathria and Paul D. Beale. *Statistical Mechanics*. Academic Press, 2011.

[73] R. W. Peterson, T. P. Purdy, N. S. Kampel, R. W. Andrews, P.-L. Yu, K. W. Lehnert, and C. A. Regal. Laser cooling of a micromechanical membrane to the quantum backaction limit. *Physical Review Letters*, 116(6), 2016.

[74] M. Pltner, G. Sadowski, S. Rzepka, and G. Blasek. Aspects of indium solder bumping and indium bump bonding useful for assembling cooled mosaic sensors. *Microelectronics International*, 8(2):27–30, 1991.

[75] David M. Pozar. *Microwave Engineering*. Wiley, 2012.

[76] John Preskill. *Lecture Notes for Ph219/CS219: Quantum Information*. California Institute of Technology, http://www.theory.caltech.edu/people/preskill/ph229/, 2015.

[77] C. M. Quintana, A. Megrant, Z. Chen, A. Dunsworth, B. Chiaro, R. Barends, B. Campbell, Yu Chen, I.-C. Hoi, E. Jeffrey, J. Kelly, J. Y. Mutus, P. J. J. O'Malley, C. Neill, P. Roushan, D. Sank, A. Vainsencher, J. Wenner, T. C. White, A. N. Cleland, and John M. Martinis. Characterization and reduction of microfabrication-induced decoherence in superconducting quantum circuits. *Applied Physics Letters*, 105(6):062601, 2014.

[78] Christopher M. Quintana. *Superconducting flux qubits for high-connectivity quantum annealing without lossy dielectrics*. PhD thesis, University of California Santa Barbara, 2017.

[79] Lord Rayleigh. On waves propagated along the plane surface of an elastic solid. *Proceedings of the London Mathematical Society*, s1-17(1):4–11, 1885.

[80] W. H. Renninger, P. Kharel, R. O. Behunin, and P. T. Rakich. Bulk crystalline optomechanics. *Nature Physics*, 2018.

[81] D. Rosenberg, D. Kim, R. Das, D. Yost, S. Gustavsson, D. Hover, P. Krantz, A. Melville, L. Racz, G. O. Samach, S. J. Weber, F. Yan, J. L. Yoder, A. J. Kerman, and W. D. Oliver. 3d integrated superconducting qubits. *npj Quantum Information*, 3(1), 2017.

[82] P. Roushan, C. Neill, A. Megrant, Y. Chen, R. Babbush, R. Barends, B. Campbell, Z. Chen, B. Chiaro, A. Dunsworth, A. Fowler, E. Jeffrey, J. Kelly, E. Lucero, J. Mutus, P. J. J. O'Malley, M. Neeley, C. Quintana, D. Sank, A. Vainsencher, J. Wenner, T. White, E. Kapit, H. Neven, and J. Martinis. Chiral ground-state currents of interacting photons in a synthetic magnetic field. *Nature Physics*, 13(2):146–151, 2016.

[83] J. J. Sakurai and Jim Napolitano. *Modern Quantum Mechanics*. Pearson, 2010.

[84] Daniel Sank, Zijun Chen, Mostafa Khezri, J. Kelly, R. Barends, B. Campbell, Y. Chen, B. Chiaro, A. Dunsworth, A. Fowler, E. Jeffrey, E. Lucero, A. Megrant, J. Mutus, M. Neeley, C. Neill, P. J. J. O'Malley, C. Quintana, P. Roushan, A. Vainsencher, T. White, J. Wenner, Alexander N. Korotkov, and John M. Martinis. Measurement-induced state transitions in a superconducting qubit: Beyond the rotating wave approximation. *Phys. Rev. Lett.*, 117:190503, 2016.

[85] Daniel T. Sank. *Fast, Accurate State Measurement in Superconducting Qubits*. PhD thesis, University of California Santa Barbara, 2014.

[86] E. Schrödinger. Die gegenwärtige situation in der quantenmechanik. *Naturwissenschaften*, 23:807–812; 823–828; 844–849, 1935.

[87] M. J. A. Schuetz, E. M. Kessler, G. Giedke, L. M. K. Vandersypen, M. D. Lukin, and J. I. Cirac. Universal quantum transducers based on surface acoustic waves. *Physical Review X*, 5(3), 2015.

[88] David I. Schuster. *Circuit Quantum Electrodynamics*. PhD thesis, Yale University, 2007.

[89] E. M. Standifer, D. H. Jundt, R. G. Norwood, and P. F. Bordui. Chemically reduced lithium niobate single crystals: Processing, properties and improvements in SAW device fabrication and performance. In *Proceedings of the IEEE International Frequency Control Symposium (Cat. No.98CH36165)*. IEEE, 1998.

[90] K. Stannigel, P. Rabl, A. S. Sørensen, P. Zoller, and M. D. Lukin. Optomechanical transducers for long-distance quantum communication. *Physical Review Letters*, 105(22), 2010.

[91] J. D. Teufel, T. Donner, Dale Li, J. W. Harlow, M. S. Allman, K. Cicak, A. J. Sirois, J. D. Whittaker, K. W. Lehnert, and R. W. Simmonds. Sideband cooling of micromechanical motion to the quantum ground state. *Nature*, 475(7356):359–363, 2011.

[92] Osamu Tokuda and Kazuhiro Hirota. Two-dimensional coupling-of-modes analysis in surface acoustic wave device performed by COMSOL multiphysics. *Japanese Journal of Applied Physics*, 50(7):07HD15, 2011.

[93] Q. A. Turchette, C. S. Wood, B. E. King, C. J. Myatt, D. Leibfried, W. M. Itano, C. Monroe, and D. J. Wineland. Deterministic entanglement of two trapped ions. *Physical Review Letters*, 81(17):3631–3634, 1998.

[94] Amit Vainsencher, K. J. Satzinger, G. A. Peairs, and A. N. Cleland. Bi-directional conversion between microwave and optical frequencies in a piezoelectric optomechanical device. *Applied Physics Letters*, 109(3):033107, 2016.

[95] R. D. Vispute, J. Narayan, Hong Wu, and K. Jagannadham. Epitaxial growth of AlN thin films on silicon (111) substrates by pulsed laser deposition. *Journal of Applied Physics*, 77(9):4724–4728, 1995.

[96] B. Vlastakis, G. Kirchmair, Z. Leghtas, S. E. Nigg, L. Frunzio, S. M. Girvin, M. Mirrahimi, M. H. Devoret, and R. J. Schoelkopf. Deterministically encoding quantum information using 100-photon Schrödinger cat states. *Science*, 342(6158):607–610, 2013.

[97] C. Wang, C. Axline, Y. Y. Gao, T. Brecht, Y. Chu, L. Frunzio, M. H. Devoret, and R. J. Schoelkopf. Surface participation and dielectric loss in superconducting qubits. *Applied Physics Letters*, 107(16):162601, 2015.

[98] H. Wang, M. Hofheinz, J. Wenner, M. Ansmann, R. C. Bialczak, M. Lenander, Erik Lucero, M. Neeley, A. D. O'Connell, D. Sank, M. Weides, A. N. Cleland, and John M. Martinis. Improving the coherence time of superconducting coplanar resonators. *Applied Physics Letters*, 95(23):233508, 2009.

[99] Samuel J. Whiteley, Gary Wolfowicz, Christopher P. Anderson, Alexandre Bourassa, He Ma, Meng Ye, Gerwin Koolstra, Kevin J. Satzinger, F. Joseph Heremans, Andrew N. Cleland, David I. Schuster, Giulia Galli, and David D. Awschalom. Coherent control of spins with Gaussian acoustics. *Submitted*, 2018.

[100] E. Wigner. On the quantum correction for thermodynamic equilibrium. *Physical Review*, 40(5):749–759, 1932.

[101] K. K. Wong, editor. *Properties of Lithium Niobate*. INSPEC, 2002.

[102] E. L. Wooten, K. M. Kissa, A. Yi-Yan, E. J. Murphy, D. A. Lafaw, P. F. Hallemeier, D. Maack, D. V. Attanasio, D. J. Fritz, G. J. McBrien, and D. E. Bossi. A review of lithium niobate modulators for fiber-optic communications systems. *IEEE Journal of Selected Topics in Quantum Electronics*, 6(1):69–82, 2000.

[103] I. Yeo, P-L. de Assis, A. Gloppe, E. Dupont-Ferrier, P. Verlot, N. S. Malik, E. Dupuy, J. Claudon, J-M. Gérard, A. Auffèves, G. Nogues, S. Seidelin, J-Ph. Poizat, O. Arcizet, and M. Richard. Strain-mediated coupling in a quantum dot–mechanical oscillator hybrid system. *Nature Nanotechnology*, 9(2):106–110, 2013.